



HAL
open science

Structure and dynamics of rod-like colloids with patchy interaction

Andrii Repula

► **To cite this version:**

Andrii Repula. Structure and dynamics of rod-like colloids with patchy interaction. Automatic Control Engineering. Université de Bordeaux, 2019. English. NNT : 2019BORD0097 . tel-03276297

HAL Id: tel-03276297

<https://theses.hal.science/tel-03276297>

Submitted on 2 Jul 2021

HAL is a multi-disciplinary open access archive for the deposit and dissemination of scientific research documents, whether they are published or not. The documents may come from teaching and research institutions in France or abroad, or from public or private research centers.

L'archive ouverte pluridisciplinaire **HAL**, est destinée au dépôt et à la diffusion de documents scientifiques de niveau recherche, publiés ou non, émanant des établissements d'enseignement et de recherche français ou étrangers, des laboratoires publics ou privés.

THÈSE PRÉSENTÉE POUR OBTENIR LE GRADE DE
DOCTEUR DE L'UNIVERSITÉ DE BORDEAUX

ÉCOLE DOCTORALE DES SCIENCES PHYSIQUES ET DE L'INGÉNIEUR
SPÉCIALITÉ : LASERS, MATIÈRE ET NANOSCIENCES

par Andrii REPULA

**Structure and dynamics of rod-like colloids
with patchy interaction**

Sous la direction de : Eric GRELET

Soutenue le 27 Juin 2019

Membres du jury :

Président du jury : M. Philippe POULIN

M. Dirk AARTS

Mme Laurence RAMOS

M. Thomas BICKEL

M. Philippe POULIN

Professeur à l'Université d'Oxford

Directrice de Recherche, CNRS

Maître de Conférences à l'Université de Bordeaux

Directeur de Recherche, CNRS

Rapporteur

Rapporteur

Examineur

Examineur

Centre de Recherche Paul Pascal (CRPP)

UMR5031, CNRS & Université de Bordeaux

115 Avenue du Dr Albert Schweitzer, 33600, PESSAC, France

Acknowledgement

Almost five years ago I arrived to France to begin a new stage of my scientific education. After one year of Master in Strasbourg, I moved to Bordeaux in order to do my PhD, which is, perhaps, the most challenging and complicated, but at the same time, undoubtedly, the most useful and significant period of my life so far. I have met a lot of smart and ambitious people over the last five years, who helped and inspired me to move forward in science. So, I want to thank all these amazing and outstanding persons.

I would like to start with my supervisor Eric Grelet, who has opened for me an extremely exciting world of experiment physics. I am so grateful for all the time you spent with me helping to manage experiments, discuss their results, and prepare all the papers, abstracts, reports, presentations and so on, and so on. I owe so much to you because my PhD project would not have been possible without your contribution. I am going to pursue a scientific career further, and all the lessons, which I have learnt from you, will be priceless on my path.

I thank my thesis committee Dirk Aarts, Laurence Ramos, Thomas Bickel and Philippe Poulin for your comments and discussions. It was a pleasure and an honor to share my research with all of you.

Of course, I really want to thank all members of DiStruc network who are truly outstanding and special people. My PhD was really a unique one due to the participation in all DiStruc events. Special thanks to the coordinator Dirk Aarts (again) for an enormous amount of the administration work, to Paul van der Schoot and Mariana Oshima Menegon for the collaboration in publishing our PRL paper as well as to Pavlik Lettinga who helped us to write and rewrite the codes for particle detection which are, indeed, a crucial things in my thesis. It is my pleasure to say thanks to Irini, Pavlina and Mercedes for organizing very cool DiStruc meeting.

I also thank to all people from CRPP including the director Cécile Zakri; administration - Béatrice Dupin, Corinne Amengual, Elisabeth Hortolland, Caroline Legrand, Nathalie Touzé. IT team - Jean-Luc Laborde, Philippe Hortolland, Sandrine Maillet and Desenfant Julien. Special thanks to Julien, who managed to fix my laptop when it was nearly crashed during the hot time of thesis writing. And all permanents staff who helped me with experiments, chemical

compounds ordering and other things: Bernard Pouligny, Jean-Christophe Loudet, Frédéric Louerat, Frederic Nallet, Ahmed Bentaleb (thank you for all my SAXS experiments), Sébastien Gounel, Eric Laurichesse, Lionel Buisson, Sabrina Bichon, and Pascal Merzeau (I hope I did not forget anyone). Bernard, you have opened for me the optical tweezer technique and gave an opportunity to be a teacher during “Fete de la Science”. It was an amazing experience!

A lot of thanks to my team-mates: Hanna, Arantza, Lachlan, Baeckkyoung, Weichao and Marie. Special thanks to Cheng, who helped with all the chemistry in my project, to Laura for the single particle detection lectures, and to Alexis who stood at the initial stage of my PhD project. I really enjoyed working with you, share thoughts and opinions. From the bottom of my heart, I wish all of you to make your dreams come true.

Thanks to all my friends whom I made during my Bordeaux period of life: Julia Voitek, Sergios, Illia, Vlad, Tania, Lili. You helped me to relax after hard scientific challenges at work. All these small and beautiful French cities such as Angouleme, Avignon, Bayonne *etc.* I have discovered with you. I will never forget this!

А цими рядками я хочу виразити вдячність своїм батькам Миколі Савовичу і Людмилі Василівні, а також своїй сестрі Каті, які своїм вихованням та настановами давали мені можливість розвиватися та пізнавати світ. Дякую, за усі книги, які ви купували, за усі мої інтереси, які ви заохочували та усі передачки щосуботи до Києва. Не можу не згадати своїх шкільних вчителів Бевза І. І. та Воробія М.П. Ви відкрили для мене світ математики та фізики. Дякую Вам на Ваш нескінченний ентузіазм та невичерпне натхнення, з яким Ви вели свої уроки. Ви показали, що тільки жорстка дисципліна та дитяча пристрасть водночас є ключовими моментами у вивченні точних наук.

La lastaj frazoj de mia agnosko mi ŝatus literumi en *Esperanto* - la tutmonda lingvo de paco kaj unuigo. Mi kredas, ke la celo de scienco estas alporti la ĝojon kaj feliĉon al la homoj. Mi esperas, ke mi plu kontribuos al la evoluo de homa civilizo kaj detruos la limojn inter homoj uzantaj mian sciencan esploron.

"To boldly go where no man has gone before"

- *from "Star Trek" series*

Résumé

Les dispersions de virus filamenteux présentent une succession d'états cristallins liquides comprenant les phases nématique, smectique (ou lamellaire) et colonnaire. L'auto-organisation de ces particules colloïdales en forme de bâtonnet s'est révélée être essentiellement pilotée par l'entropie dont résulte un potentiel d'interaction entre particules purement répulsif. Dans cette thèse, les propriétés structurales et dynamiques de bâtonnets présentant une interaction attractive directionnelle fortement localisée (interaction dite à « patch ») à l'une des extrémités des particules ont été étudiées. L'interaction attractive locale a été obtenue en fonctionnalisant les extrémités des virus filamenteux par greffage régiosélectif de colorants fluorescents hydrophobes qui jouent le rôle de « patch » enthalpique. La force d'attraction peut être modulée en faisant varier le nombre de molécules de colorant liées. Nous avons montré que cette interaction à « patch » stabilise la phase smectique au détriment de la phase nématique, laissant les autres phases cristallines liquides essentiellement inchangées. En outre, la présence de molécules de colorant fluorescent sur les extrémités des virus permet l'observation de structures lamellaires cristal-liquides avec un contraste et une résolution exacerbés. La visualisation *in situ* de défauts topologiques en phase smectique, tels que des dislocations de type coin et vis, a été réalisée à l'échelle de la périodicité du réseau. Le champ de déplacement autour d'une dislocation coin a été établi expérimentalement et comparé au profil prédit par les théories élastiques. Des dislocations de type vis ont également été mises en évidence, pour lesquelles la taille du cœur et l'hélicite ont été déterminés.

La dynamique des virus « patchy » et de ceux non fonctionnalisés a été étudiée par suivi temporel du déplacement des particules individuelles en microscopie de fluorescence. Dans toutes les phases cristallines liquides, la diffusion de particules « patchy » s'est avérée être entravée. En particulier dans la phase smectique, les bâtonnets « patchy » ont tendance à résider dans les couches diffusant principalement dans la direction perpendiculaire à l'axe principal du virus, tandis que les bâtonnets non fonctionnalisés présentent une diffusion entre couches beaucoup plus prononcée. Ce comportement peut s'expliquer par la plus grande valeur du potentiel smectique associé et mesuré expérimentalement dans les deux types de dispersion.

Nous avons combiné des effets de « patch » entropique et enthalpique en ajoutant des polymères non-absorbants à la dispersion virale fonctionnalisée. Dans ce cas, les bâtonnets s'auto-assemblent latéralement par déplétion en des clusters de morphologie définie. La diffusion de rayons X et la

microscopie optique ont été utilisées pour comparer les propriétés structurales et dynamiques des dispersions virales fonctionnalisées - ou pas - mélangées à des polymères non absorbants, et pour établir les diagrammes de phases correspondants.

En résumé, nous avons démontré un nouveau moyen efficace de contrôler la structure de fluides complexes par la modifications régio-sélective des particules constituantes.

Mots-clés: Matière molle, cristaux liquides colloïdaux, virus filamenteux, auto-assemblage, interaction « patchy », diffusion.

Summary

Dispersions of filamentous viruses exhibit a plethora of liquid crystalline states including nematic, smectic (or lamellar), and columnar phases. Self-organization of these rod-shaped colloidal particles has been shown to map the hard-core behavior for which the interaction potential is purely repulsive. In this thesis, the structural and dynamical properties of rods with highly localized directional attractive interaction (or “patchiness”) between one of the ends of the particles have been studied. Local attraction has been achieved by functionalizing the filamentous virus tips via regioselective grafting hydrophobic fluorescent dyes which act as enthalpic patch. The single tip attraction strength can be tuned by varying the number of bound dye molecules. We have shown that increasing attraction interaction stabilizes the smectic phase at the cost of the nematic phase leaving all other liquid crystalline transitions unchanged. Furthermore, the fluorescent dye molecules on the viral tips enable the observation of liquid crystalline lamellar structures with improved contrast and resolution. *In situ* visualization of topological defects in the smectic phase such as edge and screw dislocations has been thus performed at the lattice periodicity level. The displacement field around an edge dislocation has been experimentally established and compared to the profile predicted by elastic theory. Screw dislocations have been also evidenced, for which the core size and handedness have been determined.

Dynamics of patchy and pristine viruses has been investigated by tracking individual rod displacements. In all liquid crystalline phases, the self-diffusion of patchy rods has been found to be hindered compared to the self-diffusion of pristine rods. Particularly in the smectic phase, patchy rods tend to reside within the layers mainly diffusing in the direction perpendicular to the main virus axis, contrary to pristine rods whose self-diffusion between layers is far more pronounced. This behavior is explained by the higher unidimensional smectic ordering potential experimentally measured in the dispersions of patchy rods compared to that obtained for pristine rods.

We have combined both entropic and enthalpic patchinesses by adding non-adsorbing polymers into tip-functionalized viral dispersions. In this case, rod sides act as entropic patches due to attractive depletion interaction between them. Small angle X-ray scattering and optical microscopy techniques have been used to compare the structural and dynamical properties of pristine and tip-functionalized viral dispersions mixed with hydrophilic polymers acting as depletants agent. We

have determined and compared the phase diagrams obtained for the two types of virus-polymer systems.

In summary, we have demonstrated a new and efficient way to control the structure of complex fluids by implementing site-specific modifications of building blocks.

Key words: Soft matter, colloidal liquid crystals, filamentous viruses, self-assembly, patchy interaction, self-diffusion.

Contents

0. General introduction	13
0.1 Colloids and a concept of « big atoms »	14
0.2 Colloidal interactions.....	15
0.2.1 Hard-core interaction	16
0.2.2 Depletion interaction (attraction through repulsion).....	17
0.2.3 Patchy interaction	19
0.3 Colloidal rods	21
0.3.1 Phase diagram of rod-like colloids with hard core interaction	21
0.3.2 Rod-like colloids under depletion or entropic patchiness	24
0.3.3 Rod-like colloids with enthalpic patchiness	28
0.4 Fd-virus as a model system of colloidal rods	31
0.4.1 Self-assembled structures in fd suspensions	32
0.4.2 Dynamics in fd suspension	34
0.4.3 Chemical functionalization of fd	39
0.5 Linear topological defects in lamellar liquid crystalline ordering.....	40
0.5.1 Elastic properties of nematic and smectic A liquid crystals	40
0.5.2 Screw and edge dislocation in molecular liquid crystals	43
0.6 Outline of the thesis	45
0.7 References.....	46
1. Directing liquid crystalline self-organization of rod-like particles through tunable attractive single tips.....	55
1.1 Directing liquid crystalline self-organization of rod-like particles through tunable attractive single tips	56
1.2. Supplemental Material	69

2. Elementary edge and screw dislocations visualized at the lattice periodicity level in smectic phase of colloidal rods	73
2.1 Elementary edge and screw dislocations visualized at the lattice periodicity level in smectic phase of colloidal rods	74
2.2. Supplemental Material	85
3. Effect of patchy interaction on dynamics of rod-like colloids	89
3.1 Introduction	90
3.2 Results and Discussion	91
3.2.1 Mean square displacements in different phases	91
3.2.1.1 Columnar and Smectic B phases	92
3.2.1.2 Smectic A phase	94
3.2.1.3 Nematic phase	99
3.2.1.4 Isotropic liquid phase	103
3.2.2 Self-diffusion coefficients of patchy and pristine rods	106
3.2.3 Orientational order parameter in patchy and pristine suspensions	108
3.3 Conclusions	109
3.4 References	110
Appendix	113
4. Self-organization of rod-like particles with combination of both entropic and enthalpic patchiness	121
4.1 Introduction	122
4.2 Material and Methods	123
4.2.1 Enthalpic patchiness: virus tip-labeling with fluorescent dyes	123
4.2.2 Entropic patchiness: choice of depleting agent	124

4.3 Results and discussions..... 126

 4.3.1 Effect of PEG 20k on tip-labeled suspension 126

 4.3.1.1 Phase diagram of fd Y21M+PEG20k 126

 4.3.1.2 SAXS experiment on fd Y21M suspension with combined patch..... 128

 4.3.1.3 Single rod dynamics within the assemblies 131

 4.3.2 Effect of PEG 8k on tip-labeled viral suspension..... 132

4.4 Conclusions..... 134

4.5 References..... 135

 Appendix.....137

Conclusions and Perspectives.....143

Chapter 0

General introduction

Contents

0.1 Colloids and a concept of « big atoms »	14
0.2 Colloidal interactions.....	15
0.2.1 Hard-core interaction	16
0.2.2 Depletion interaction (attraction through repulsion).....	17
0.2.3 Patchy interaction	19
0.3 Colloidal rods	21
0.3.1 Phase diagram of rod-like colloids with hard core interaction	21
0.3.2 Rod-like colloids under depletion or entropic patchiness	24
0.3.3 Rod-like colloids with enthalpic patchiness	28
0.4 Fd-virus as a model system of colloidal rods	31
0.4.1 Self-assembled structures in fd suspensions	32
0.4.2 Dynamics in fd suspension	34
0.4.3 Chemical functionalization of fd	39
0.5 Linear topological defects in lamellar liquid crystalline ordering.....	40
0.5.1 Elastic properties of nematic and smectic A liquid crystals	40
0.5.2 Screw and edge dislocation in molecular liquid crystals	43
0.6 Outline of the thesis	45
0.7 References.....	46

0.1 Colloids and a concept of « big atoms »

Colloids are insoluble particles dispersed in continuous media (liquid or gas) whose size is in the range of $\sim 10\text{nm}$ to $\sim 1\mu\text{m}$. They are sensitive to the observable random motion, or so-called Brownian motion, arising from the thermal energy of order of magnitude $k_B T$ for each particle, where k_B is the Boltzmann constant and T is the absolute temperature. Thanks to their microscopic size, colloids can be easily observed with optical microscopy techniques.

Historically the basic understanding of colloidal science began in the early 20th century, when the reality of atoms and molecules has been proven [2]. Albert Einstein provided the theoretical explanation of Brownian motion by assuming that colloids dispersed in liquid experience random collisions by the much smaller solvent molecules. This resulted in the derivation of an expression for the mean square displacement of colloidal particles dispersed in liquid, and of exponential expression for the number density of particles in dispersion that has reached sedimentation equilibrium [1]. Jean Perrin proved these two theoretical predictions experimentally by observation of resin spherical colloids with optical microscopy. He tracked the trajectories of single diffusing particles, and counted the number of particles as a function of height in colloidal suspension in sedimentation equilibrium. For both cases he calculated Avogadro's number, and the convergence of those two independent values undoubtedly manifested the existence of atoms [2].

Einstein's and Perrin's pioneering discoveries have shown that relatively large particles such as colloids can behave in the same way as their atomic and molecular counterparts whose are roughly three orders of magnitude smaller. In other words, the structural and dynamical properties of colloidal suspensions are governed by the same thermodynamics that determines the behavior of atomic and molecular systems. For this reason colloids are often considered as "big atoms". Therefore, thanks to their ability of being observed by optical microscopy at the level of single particle, colloids give insight into fundamental questions of condensed matter. For example, spherical colloidal particles have been used to study such phenomena as growth and nucleation in crystals [4], crystal melting [5], and phase transitions in fluids [6].

Colloidal particles can also serve as tools or building blocks for engineering the assembly of various targeted structures [7], [8]. Conceptually, the simplest building blocks for self-assembly are colloidal spheres with hard-core interaction [3]-[5]. "Hard-core" means that such particles don't interact if they don't interpenetrate, and repulsion between them is infinitely high

if they do. Hard colloidal spheres lack any directionality in their shape and interaction; therefore, they can assemble only into crystalline structures with the simple symmetry, such as face-centered cubic (FCC), hexagonal close-packed (HCP) and body-centered cubic (BCC). Contrary to the isotropic particles, colloids with anisotropic shape and interaction extend the number of possible ways of their assembly, and can potentially lead to as complex structures as can be seen at atomic and molecular scale. For example, colloids with shape anisotropy, such as hard rods, exhibit nematic, smectic and columnar phases, which are also found in molecular liquid crystals [9], [10]. Interaction anisotropy can be induced by deposition of some attractive or “patchy” sites on the surface of otherwise hard particles. An example of colloids with directional attractive interaction or “patchiness” is the triblock Janus colloidal spheres (hydrophilic body and two hydrophilic poles) dispersed in water, which self-organize into a colloidal kagome lattice (centres of mass of spheres are organized into equilateral triangles and regular hexagons, arranged so that each hexagon is surrounded by triangles and vice versa), due to electrostatic repulsion of the bodies and attraction of the poles [11].

In this thesis, we will study the self-organization of anisotropic rod-like colloids with different types of directional interactions. Firstly, we will explain the concept the simplest interaction – hard-core repulsion, and then we will show how to go beyond and to induce attraction interaction between colloids.

0.2 Colloidal interactions

In the middle of the 20th century the theory of colloidal interaction has been proposed by Derjaguin, Landau [12], Verwey and Overbeek [13]. In their theory, known as DLVO, for a dispersion of charged spherical particles it is claimed that there are two opposite contributions which define the overall interaction potential (Fig.0.1). There are the short range (0-10 nm) Van der Waals attraction and the repulsion originating from the electric double layer which encloses charged colloid and is characterized by the Debye screening length [14]. However, the other types of interactions such as hard-core repulsion [3], depletion [16] and directional attractive interaction or patchiness [20] have gained experimental as well as theoretical interest later on.

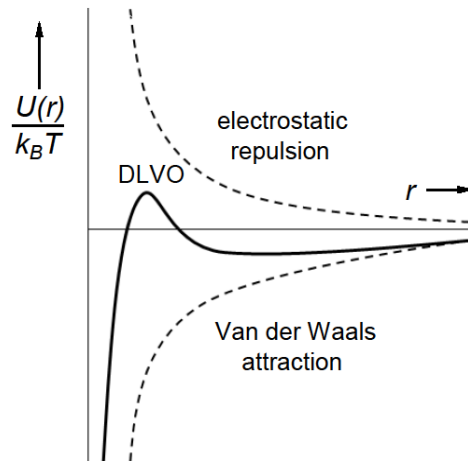


Fig.0.1. Schematic plot of the DLVO interaction potential $U(r)/k_B T$ between charged colloidal spheres which is the sum of double layer repulsion (top) and Van der Waals attraction (bottom), where r is the center-to-center distance between the particles.

0.2.1 Hard-core interaction

The simplest model interaction between two colloids is the so-called hard-core interaction based on excluded volume. In this case, as we already mentioned, there is no interaction when the particles do not overlap and an infinite repulsion when they do overlap. Experimentally it can be nearly achieved by adding a polymer brush on the particle surfaces [3]-[5]. The thickness of this stabilized polymer layer d_{brush} must be much smaller than the radius of colloidal particle R ($d_{brush} \ll R$). This leads to the absence of short-range attraction and only to repulsion between the particles. The pairwise interaction between two hard spheres can be then written as (Fig.0.2):

$$U(r) = \begin{cases} \infty & r \leq 2R \\ 0 & r > 2R \end{cases} \quad (0.1)$$

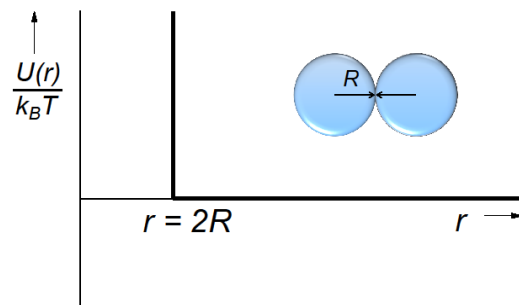


Fig.0.2. Hard-core interaction potential between two spherical particles; r is the center-to-center distance between the particles.

The phase behavior of the system which consists of hard particles is dictated only by entropy. In entropy-driven systems, the phases that can be observed depend only on particle shape and density, and do not depend on temperature. In the case of spherical colloidal suspensions, it results in the athermal phase diagram reported in the experimental study of Pusey and van Megen [3]. By increasing the concentration of hard spheres the fluid, crystal, and glass phases have been achieved (Fig.0.3).

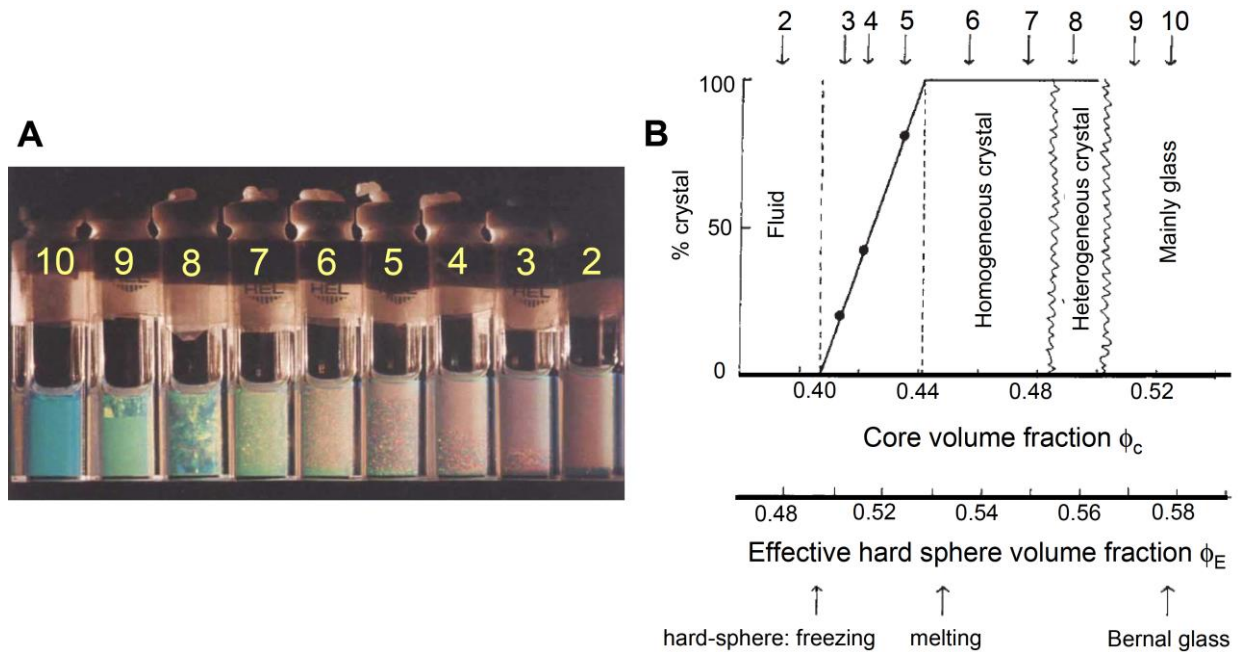


Fig.0.3. (A) Hard sphere suspensions illuminated from behind by the white light. The samples are contained in cells and are numbered 2-10 from the right in order of increasing volume fraction. (B) Phase diagram is established according to the visual inspection of the samples. The two horizontal axes indicate the experimentally measured sphere volume fraction ϕ_c and the effective hard sphere volume fraction ϕ_E defined as $\phi_E = (0.494/0.407)\phi_c$ [3], where 0.407 is the core volume fraction ϕ_c at which freezing start, and 0.494 is an effective volume ϕ_E of hard spheres freezing predicted by computer simulations [105].

0.2.2 Depletion interaction (attraction through repulsion)

Let us consider the mixture of colloidal hard spheres and non-adsorbing polymers. “Non-adsorbing” means that the polymer chains have neither adhesive nor repulsive interaction with the colloidal surface. In the 1950s Asakura and Oosawa [15] developed a theory for the effective interaction between colloidal particles dispersed in a solution of ideal polymers. It has been

shown that there is an indirect effective attraction, called depletion interaction, between colloids driven by entropy associated with the centers of mass of the polymers (or depletants). In such mixture of spheres and polymers, each colloidal particle is enclosed by the depletion (or excluded) layer with the thickness δ given by the radius of a depletant. The center of mass of the polymer cannot penetrate this layer, thus the local polymer concentration near the colloids surface is lower than the one in the bulk. When two colloids approach closer than 2δ , their depletion layers overlap, and the overall volume from which the polymers are excluded is decreasing by the amount of overlapping volume $\Delta V_{overlap}$ (Fig.0.4). One can also claim that the depletants gain more translation entropy when the depletion layers surrounding colloids are overlaid. Therefore the depletion attraction is a purely entropic effect driven by excluded volume interaction [16]. The size of the depletant agents implies the range of attraction, while their concentration determines the strength of attraction. The expression for the depletion interaction between two spheres with radii R under the osmotic pressure $\Pi = n_b k_B T$, where n_b is bulk number density of depletant, is [14]:

$$U(r) = \begin{cases} \infty & r < 2R \\ -\Pi V_{overlap}(r) & 2R \leq r \leq 2R + 2\delta \\ 0 & r > 2R + 2\delta \end{cases} \quad (0.2)$$

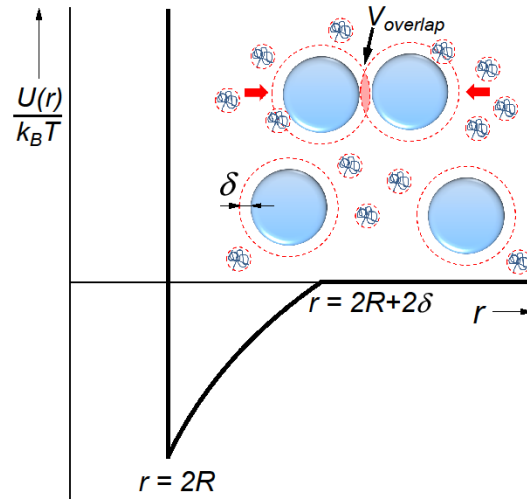


Fig.0.4. Sketch of depletion interaction potential with the schematic picture of colloidal spheres with radii R in a mixture with non-adsorbing polymers with radii δ ; r is the center-to-center distance between spheres and $V_{overlap}$ is the overlap volume between depletion layers.

0.2.3 Patchy interaction

In section 0.1, we mentioned that colloids with isotropic shape and interaction can mimic atomic structures with the simplest crystal structures such as FCC or HCP. Today's research demands to go beyond these simple symmetrical structures and to mimic more complex assembly such as, for example, the diamond crystal, to be employed in photonic application [17], or some protein aggregation [18]. To fabricate these new generations of materials, the local directional attraction interaction, or so-called patchy interaction, has to be induced between colloids. The term "patchy sites" is usually associated with chemical or physical surface patterning. There is a trend to discriminate entropic patchiness (particle shape modification) and enthalpic patchiness (modification of particle surface by chemical functions) in the literature [19]. We will focus on these two mechanisms in section 0.3.

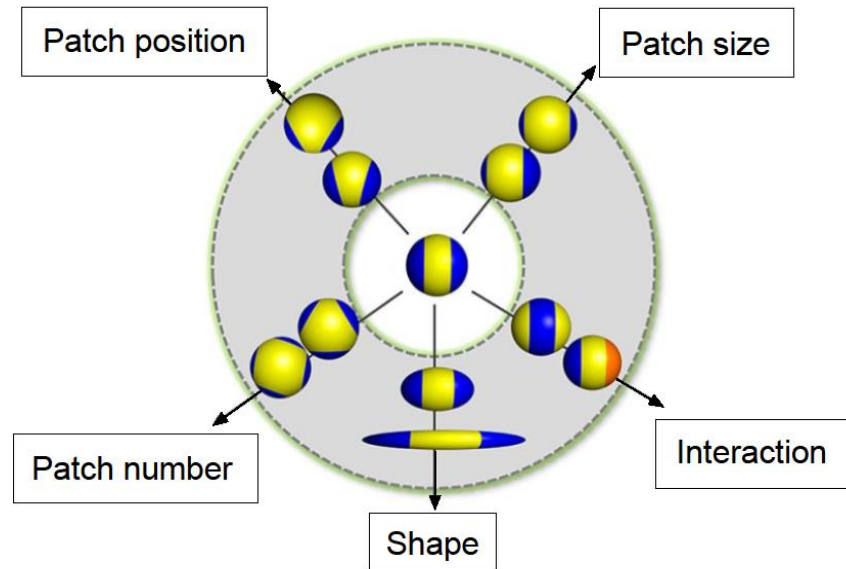


Fig.0.5. Different parameters to introduce and vary the patchiness (blue and orange colours) on the surface of colloid: size, position, number, shape of the patches and interpatch interaction which depends on chemical functions deposited onto surface. Illustration here is for the triblock Janus sphere [11] as a reference system in the center of a circle, but it can be also generalized for other shapes such as rods, cubes etc [57].

In principle, there is an enormous amount of ways to modify the particle surface. One can tune the size of the patches, their position, number, shape and interaction selectivity (Fig.0.5) [7], [57]. In order to understand the concept of patchy interaction, let us consider the paradigmatic example suggested by Kern and Frenkel [20], where a hard sphere of radius R possesses an

attractive patch on its surface. The position of this patch is given by a unit vector \mathbf{n}_i , and its size is given by a conical segment of half-opening angle α (Fig.0.6). The patches on the surface of the different particles interact via a square-well potential with attraction range Δ . Such model can serve as a reference system for the more detailed study of the effect of patch number, size, position etc. The expression for the interaction potential between particles i and j can be read as:

$$U(\mathbf{r}_{ji}) = U^{SW}(r) \cdot f(\Omega_{ij}) \quad (0.3)$$

$U^{SW}(r_{ij})$ is an isotropic square-well interaction term of depth ε and range Δ [Fig.0.6]:

$$U^{SW}(r_{ij}) = \begin{cases} \infty & r \leq 2R \\ -\varepsilon & 2R \leq r \leq 2R + \Delta \\ 0 & r > 2R + \Delta \end{cases} \quad (0.4)$$

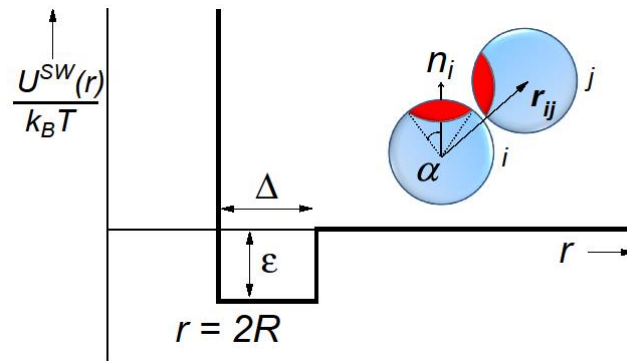


Fig.0.6. Square-well interaction potential and the sketch of two patchy particles; r is the center-to-center distance between spheres. Attraction between hard particles is restricted to the configuration at which two patchy segments (red areas) face each other.

The angular function $f(\Omega_{ij})$ is defined as (\mathbf{r}_{ij} is a particle separation vector):

$$f(\Omega_{ij}) = \begin{cases} 1 & \text{if } \begin{cases} \mathbf{r}_{ij} \cdot \mathbf{n}_i > \cos\alpha, \\ \text{and} \\ \mathbf{r}_{ji} \cdot \mathbf{n}_j > \cos\alpha \end{cases} \\ 0 & \text{otherwise} \end{cases} \quad (0.5)$$

Experimentally this model system has been realized by Granick *et al.* [21], [22]. In these studies 50% of the particle surface has been covered by the patchy functions (Fig.0.7). In these so-called Janus spheres attractive interaction appears due to hydrophobicity of chemically modified hemispheres. Janus spheres are found to self-assemble into colloidal clusters of changing coordination number or wormlike chains (Fig.0.7B,C). Experimental conditions of the dispersion such as pH and ionic strength determine the morphology of formed colloidal clusters.

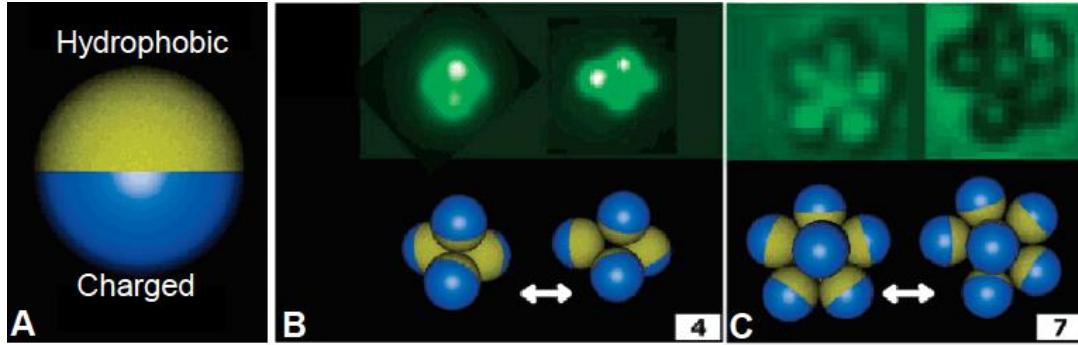


Fig.0.7. (A) Illustration of Janus colloidal spheres in water dispersion with hydrophobic hemispheres. Comparison of epifluorescence images and Monte Carlo simulations of clusters configurations with (B) four particles and (C) seven particles [21].

0.3 Colloidal rods

In the previous sections, some elements of spherical colloid phase behavior and different types of colloidal interaction have been reviewed. Although sphere ability to form closed-packed colloidal crystals has shed light into some fundamental soft matter problems [3]-[6], the more complex symmetries of atomic systems have to be reproduced at the colloidal scale to resolve new challenging questions of condensed matter and materials science. Recognition that anisotropic particles possess richer phase behavior than their isotropic counterparts has motivated new directions of colloidal research which investigate the chemical synthesis and physical properties of the building blocks with novel shapes and interactions. In the following section, we will overview one class of anisotropic particles – colloidal rods, and will give insight into their phase behavior as well as discuss the key experiments which have been performed involving different types of interactions between these particles.

0.3.1 Phase diagram of rod-like colloids with hard core interaction

Suspensions of hard rod-like particles exhibit a plethora of phases compared to hard spheres. Additionally to the liquid and crystal states, rods can form liquid crystalline phases due to their anisotropic shape. Those additional phases possess positional as well as orientational orders in at least one direction of space. Liquid crystalline phase behavior has been studied by using systems of organic rods such as tobacco mosaic viruses [23], or fd-viruses [9], [24]-[26] as

well as inorganic rods such as boehmite [28], vanadium pentoxide [29], β -ferric oxyhydroxine [30] and silica rods [10], [27]. Probably, the most extensive study has been done on the suspensions of fd-viruses, whose phase diagram is depicted in Fig.0.8. By increasing the volume fraction of rods, they can form liquid crystalline nematic, smectic and columnar phases [9], [25].

Onsager was the first to theoretically describe the isotropic-nematic phase transition in suspension of infinitely long hard rods [31]. He wanted to explain this phase transition in the suspension of tobacco mosaic viruses [58]. Onsager theory describes the transition from orientationally disordered isotropic liquid phase to orientationally ordered nematic phase (Fig.0.9). His results show that such phase transition for infinitely long hard rods is associated with an increase of entropy.

Onsager theory is based on the expression of the free energy of hard cylinders dispersed in a fluid. The total free energy is the sum of three terms. The first one is the free energy of an ideal solution; the second term describes the contribution of the orientation entropy to the free energy; and the third term accounts for the interaction between particles.

$$F = F_{id} + F_{or} + F_{int} \quad (0.6)$$

The system is assumed to be spatially uniform and thus the expression for particle density can be read as $\rho(r, \Omega) = (N/V)f(\Omega)$, where r and Ω is a vector and a solid angle describing the position and the orientation of rod respectively, N is the number of the rods, and V is the volume of the system. The function $f(\Omega)$ indicates the probability that a rod is pointing at a solid angle Ω , it is normalized as $\int f(\Omega)d\Omega = 1$. Using this input, it is possible to rewrite the equation (0.6) into Onsager free energy for a solution of rod-like particles at the level of second virial approximation:

$$F/k_bT = \log \frac{N}{V} + \int f(\Omega) \log(4\pi f(\Omega)) d\Omega - \frac{1}{2} \frac{N}{V} \iint \beta(\Omega, \Omega') f(\Omega) f(\Omega') d\Omega d\Omega' \quad (0.7)$$

Function $\beta(\Omega, \Omega')$ is called Mayer overlap function, and for hard cylinders it is equal to the excluded volume to one particle with orientation Ω due to the presence of another particle with orientation Ω' (one can introduce the angle γ as a relative angle between two cylinders):

$$\beta(\Omega, \Omega') = -v_{excl}(\Omega, \Omega') \simeq -2L^2 D \sin(\gamma) \quad (0.8)$$

The volume excluded to a given cylinder due to the presence of another cylinder is sketched in Fig.0.9 and is dependent on the angle γ .

The second term in the equation (0.7) is related to the *orientational entropy*, whereas the third term is related to the *packing entropy*. The isotropic-nematic phase transition arises from a

competition between these two types of entropy. At low rod concentration the orientational entropy dominates and all cylinders are pointed in different directions giving rise to isotropic phase, whereas at high concentration the packing entropy becomes more important which favors the nematic phase. By performing a stability analysis of the Onsager equation (0.7), it has been concluded that at certain volume fraction of hard rods $\varphi \approx 4 \frac{D}{L}$, where D and L are rod diameter and length respectively, isotropic phase becomes unstable towards nematic fluctuations, and isotropic-nematic phase transition occurs [59].

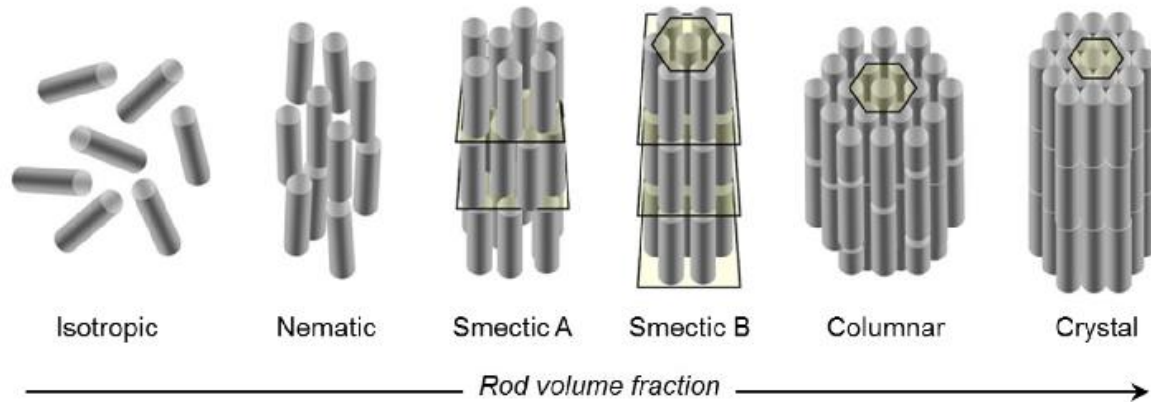


Fig.0.8. Schematic representation of colloidal rod-like fd-virus self-organization. Different phases can be formed by increasing the particle concentration. The isotropic liquid and crystal phases appear at very low and at very high volume fraction respectively, while the liquid crystalline nematic, smectic and columnar phases are arising between them due to anisotropic particle shape .

The isotropic-nematic transition for long hard rods is an example of a very general class of phase transitions which are purely entropy driven and does not depend on temperature. Another example of the counterintuitive role of entropy, such as depletion interaction, has been discussed in the section 0.2.2. As we already mentioned, in nematic phase all particles are aligned in average along the same direction called director. There is long range orientational order and no long range positional order in this phase. Upon increasing the particle density, the smectic phase becomes stable, and rods self-organize into the stacks of liquid-like layers. Additionally to the orientational order, there is a 1D positional order along the director (Fig.0.8). It has been shown by Frenkel *et al.* [32] that there is no need to induce attractive interaction between rods, and purely repulsive hard-core interaction is enough to stabilize the smectic ordering, meaning that nematic-smectic is also entropy driven transition as the isotropic-nematic one.

The nematic-smectic phase transition is predicted to be independent on the rod size above the aspect ratio $L/D > 10$ [33], and it occurs at rod volume fraction $\varphi_{Nem-sm} \sim 0.5$ as shown by the computer simulations [32], [33], theory [34], and experiment [9].

Columnar phase possesses a 2D positional order meaning that the particles form liquid-like columns that are arranged in a 2D lattice. Although it has been detected in fd-virus suspension [26], the computer simulations and theory cannot evidence the columnar phase stabilization for rods by entropy alone [35], [36]. We will not describe the details of these results, because it goes out the scope of this thesis.

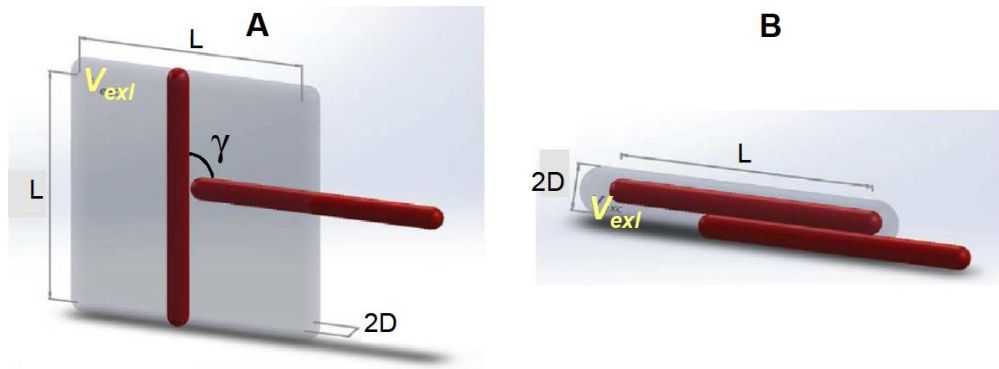


Fig.0.9. A rod with the length L and diameter D excludes the center of mass of the second identical rod from occupying a certain volume (greyish shadow enclosing the rod). These excluded volumes scales as L^2D for (A) perpendicular particle orientation, and LD^2 for (B) aligned or parallel particle orientation.

0.3.2 Rod-like colloids under depletion or entropic patchiness

We have shown in section 0.2.2 that interaction between hard colloidal particles can be tuned from repulsive to effective attractive by adding non-adsorbing polymers. Unlike spherical particles, the depletion attraction between rods is highly dependent on both their mutual orientation and their center of mass separation along the axial and radial directions. The overall entropy of rod-polymer mixture increases if rods coalesce via side-to-side association. In this case the maximized overlap volume between two excluded layers of thickness δ which surrounds rods with length L and diameter D is scaled as $V_{overlap} \sim LD^{1/2}\delta^{3/2}$ (Fig.0.10) [19].

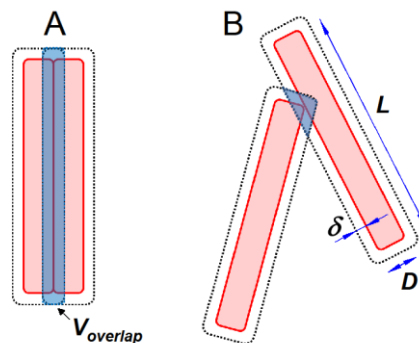


Fig.0.10. Illustration of the excluded volume between rods, where L and D are rod length and diameter respectively, mediated by depletants that induce a fixed depletion thickness δ (indicated by the dashed lines). The overlap volume V_{overlap} between depletion layers is maximized (blue shadow) for (A) the laterally associated rods rather than for rods with (B) some random mutual orientation. The rod sides could be regarded as patchy sites on the particle surfaces.

For depletion interaction, attraction range and strength can be tuned by varying the polymer size and concentration respectively. The most extensive experimental studies on rods under depletion interaction have been performed employing filamentous viruses fd (see details in section 0.4) as a model system of rod-like colloids [37], [45]. Two different viral assemblies have been observed in fd suspensions mixed with (i) Dextran 500k (radius of gyration R_g is about 16 nm [60]) or with (ii) PEG 8k (radius of gyration R_g is about 4 nm [61]) polymers, which can be regarded as relatively big and relatively similar in size depletants, respectively, compared to virus diameter of 3.5 nm [62]. (i) In case of mixture with relatively large polymers Dextran 500k, highly anisotropic interaction between particles leads to the formation of circular colloidal membranes consisting of a single monolayer of aligned rods (Fig.0.11A) [37] In fact, membrane has hemi-toroidal curved edge because such shape decreases the area of rod-polymer interface, therefore reducing line tension, at the cost of increasing the elastic energy due to twist distortion [53]. Dynamical study of such structures performed at the single particle level by fluorescence microscopy revealed the liquid-like internal structure of the membranes. (ii) When relatively small polymers PEG 8k are used, it results in the growth of the platelets which are monolayer with crystalline structures made of hexagonally assembled aligned rods (Fig.0.11B) [38]. These platelets possess crystalline internal order which has been proved by small X-ray scattering experiment (SAXS) and by the lack of significant particle motion within the structure.

For some specific cases which depend on kinetics of platelets growth, a linear topological defect such as a screw dislocation can be observed in the center of this assembly. Linear topological defects in molecular and colloidal liquid crystals will be discussed in section 0.5 in more details.

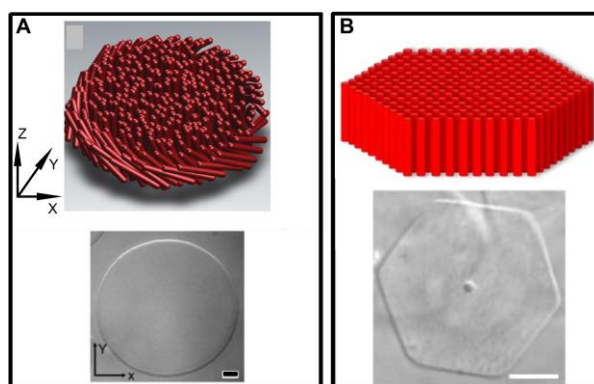


Fig.0.11. Schemes and DIC (differential contrast microscopy) images of self-assembled structures made of rod-like viral particles with length of about $1\ \mu\text{m}$ and diameter of $7\ \text{nm}$ [62] driven by depletion interaction. (A) Liquid-like colloidal membrane in the mixture with large polymers Dextran 500k [37] (radius of gyration R_g is $16\ \text{nm}$ [60]) as a depletant agent. Scale bar: $2\ \mu\text{m}$. (B) Hexagonal platelet induced by short range depletion attraction coming from the polymers PEG 8k [38] (radius of gyration R_g is about $4\ \text{nm}$ [61]), whose size is similar to virus diameter. Scale bar: $5\ \mu\text{m}$.

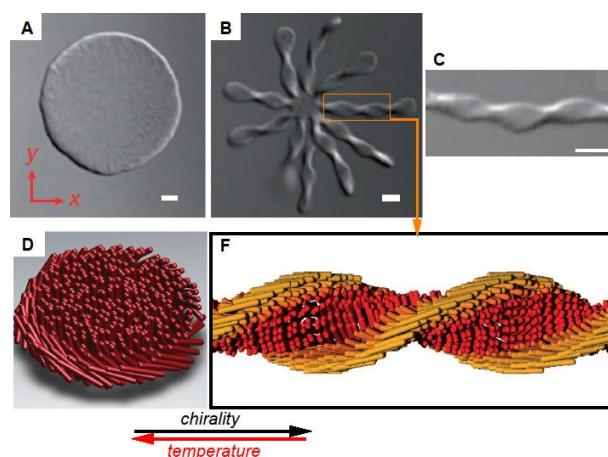


Fig.0.12. DIC images of (A) liquid-like colloidal membrane at high temperature, and (B) starfish shaped membrane made of twisted ribbons which grew from the circular membrane upon decreasing temperature. (C) DIC image of isolated twisted ribbon. Scale bar: $2\ \mu\text{m}$. Schematic illustration of (D) circular membrane showing how its edge assumes interfacial minimization curved profile, and (F) twisted ribbon structure [52].

It is worth stressing, that under effective depletion attraction, colloidal rods tend to approach each other strictly by their sides because any other mutual orientations decrease overall entropy of the system. Therefore this anisotropic attraction between rods induced by the excluded volume interactions can be regarded as patchiness with entropic origin, with the rod side considered as a patch on the particle surface.

It has been shown that internal chirality of fd-virus [52] or DNA-origami filaments [63] strongly affects the morphology of the structures formed under depletion. When two chiral rods are in the close proximity of each other, the interaction energy between them is minimized if they are twisted with respect to each other, meaning that particle main axes are not parallel to each other [47], [52]. In the case of a circular liquid-like membrane (Fig.0.12A), where 2D layered geometry cannot support twist, chirality is expelled to its edges. Hence, chirality of the constituent rods controls the strength of line tension γ_{eff} which is the parameter governing the shape of the edge of circular liquid-like membrane. There are two contributions to the effective line tension: γ_{bare} (line tension which appears due to the reduction of rod-polymer interfacial tension) and γ_{chiral} (chiral contribution to the line tension):

$$\gamma_{eff} = \gamma_{bare} - \gamma_{chiral} \quad (0.9)$$

At high enough temperatures (of around 60°C) fd-wt virus loses its chiral properties and become achiral [53], thus at high temperatures $\gamma_{eff} = \gamma_{bare}$. Decreasing the temperature enhances the magnitude of chiral interactions, resulting in smaller γ_{eff} value. At sufficiently low temperatures the chiral contribution to the line tension dominates the bare line tension, decreasing the energetic penalty of creating edges resulting in their spontaneous formation. In Fig.0.12A a membrane at high temperature is shown. With decreasing temperature, the chiral fluctuations of membrane edge become more significant, indicating that γ_{eff} is decreasing. Eventually the edge becomes unstable, giving rise to a polymorphic transition in which twisted ribbon-like structures grow from the edges of membranes (Fig.0.12B).

1D twisted ribbons (Fig.0.12C) are stable at low polymer concentration and low temperatures (small γ_{bare} and large γ_{chiral}), whereas the 2D membranes are stable for large γ_{bare} and small γ_{chiral} [52], [63]. Fluorescence optical microscopy reveals liquid-like dynamics within the twisted ribbon-like structures [52].

The suspension of colloidal rods is an example of a more general class of particles with irregular shapes where directional entropic attractive forces are induced by adding non-

adsorption polymers. Other illustrations of shape anisotropic colloids with entropic patchiness promoted by depletion interaction are, for instance, lock and key particles [39] and colloidal superballs [40] (Fig.0.13).

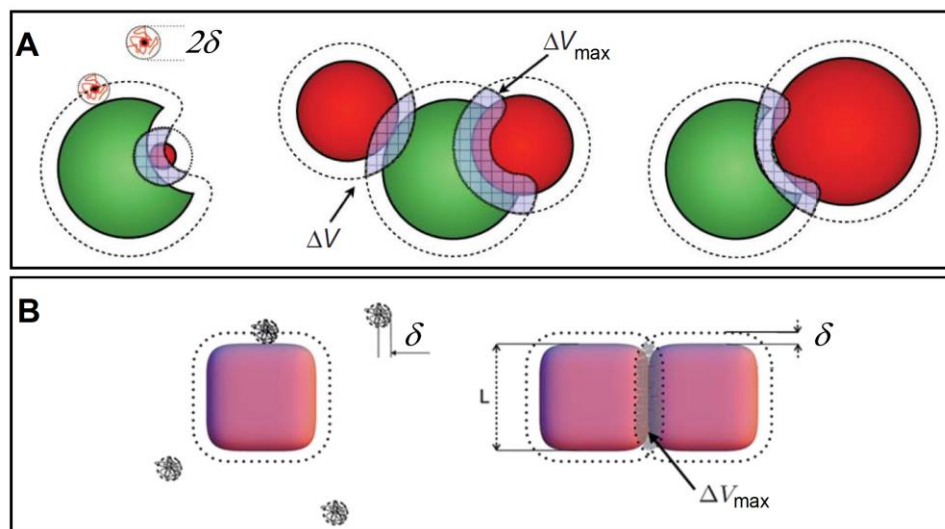


Fig.0.13. (A) Illustration of the depletion interaction between a lock (green particle with a spherical cavity) and a key (simple red spherical particle) induced by a depletant agent of radius δ . The maximum overlapping excluded volume, ΔV_{max} , is achieved when the key particles precisely fits into the spherical cavity of the lock particle. (B) Depletion effect between superballs (cubic particles with rounded edges) [19].

0.3.3 Rod-like colloids with enthalpic patchiness

Colloids with chemically inhomogeneous surfaces are another type of patchy particles which are referred to colloids with enthalpic patch. In section 0.2.3, we mentioned the Janus spheres with hydrophobic and hydrophilic parts, and the types of superstructures they can generate [21], [22]. Preparation of Janus rods has extended the variety of complex architectures which can be obtained via enthalpic patchiness. The simplest example of colloidal rods with chemically modified surface is so-called Janus colloidal matchsticks which are monodisperse silica rods coated with gold on one tip which acts as a enthalpic patch (Fig.0.14) [41]. The size of these patchy inclusions is characterized by the patch angle α (Fig.0.14A), which is found to be equal to 116° . According to the matchstick dimensions of $L = 2.3 \mu\text{m}$ and $D = 1.1 \mu\text{m}$, these colloidal rods thanks to their chemical heterogeneity can be regarded as mesoscopic amphiphiles.

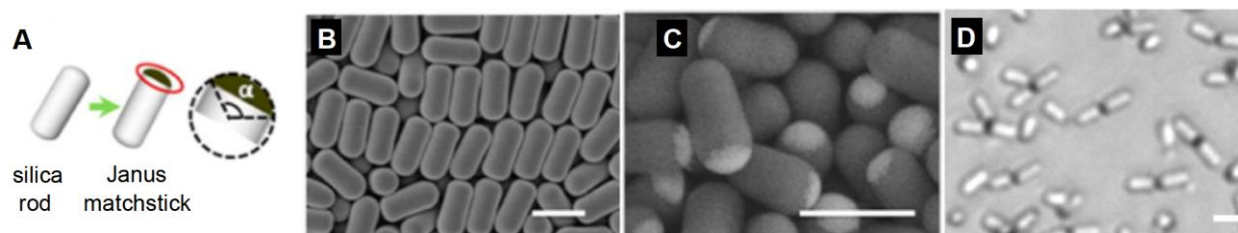


Fig.0.14. Schematic (A) and scanning electron microscopy images (SEM) of (B) pristine and (C) tip-functionalized silica rods with gold. These metal inclusions drive particles to self-assemble into various clusters such as bipods and tripods (D) [41]. Scale bars: 2 μ m.

When exposed to water, the gold tips of Janus matchsticks are brought together due to their hydrophobicity forming multipod structures of different coordination number such as bipods and tripods (Fig.0.14D). The resulted structures were observed by scanning electron microscopy (SEM) and are the interplay of sedimentation (which gives rise to a planar geometry), entropy (which drives rods to possess the highest orientation freedom within each multipod), and enthalpy (which promotes the attraction between the matchstick cluster).

Nevertheless, the fixed patch size restricts the complexity of output self-assembled structures using Janus matchsticks as the building blocks. Therefore to deeply explore the potential morphologies of rod-like colloids with enthalpic patchiness, mesoscopic amphiphiles with varied size of the chemical functions on the tip have been prepared by Mirkin group [42]. They synthesized rod-like particles consisting of gold (Au) hydrophilic domain and polymer called oxidized polypyrrole (Ppy) hydrophobic domain (Fig.0.15A). The driving force to raise the assembly in this rod system is the hydrophobic attraction between polymer ends (Fig.0.15A). Three different types of particles have been produced as a function of Au-to-Ppy surface areas ratio, and the rod length has been fixed at value of 4.5 μ m. Rods with a 1:4 gold-to-polymer ratio assembled into \sim 60 μ m diameter tubes whose walls made of the single layer of particles (Fig.0.15B). Rods with a 3:2 gold-to-polymer ratio give raise to \sim 29 μ m tubular structures (Fig.0.15C). And when rods with 4:1 are utilized the opened tubular structures are obtained (Fig.0.15D). These assembled ways of gold/polymer patchy rods can be partially explained by using theoretical models for cylindrical micelles made of amphiphilic molecules [43]. The geometrical packing factor $R = V/a_h l_c$, where V is a volume of individual rod, a_h is the average rod head area, and l_c is the rod length, can be used to understand the yielding structures based on these patchy particles. It is worth stressing that factor R increases as gold-to-polymer ratio become higher. Each patchy rod can be imaged as a truncated cone, because of strong attractive

interaction between polymer ends and the diameter difference between gold and polymer particle domains (Fig.0.15A). The average diameter of gold block is 400 nm and the polymer block diameter is 360 nm. The rod head area a_h can be estimated from a first order approximation of the average area occupied by the gold end of each rod in the microtubular structure, which is defined by the perimeter area of the tube divided by the total number of rods that make up the assembly. For the fixed rod length, the contraction of gold domain contribution leads to decrease of a_h , and therefore results in decreasing of the overall superstructure curvature. This general trend was observed for three tubular structures shown in Fig.0.15.

To summarize, it worth to emphasize that there are very few experimental results on colloidal rods with enthalpic patchiness. Moreover, there are some drawbacks in the works reviewed in this section. For examples, the colloidal matchsticks made of silica rods are not Brownian particles, therefore their self-assembly is strongly affected by sedimentation (Fig.0.14D). The yield of superstructures with completely closed walls made of Au-Ppy patchy rods (Fig.0.15B-D) is low ($\sim 10\%$). Probably, the drawback of Au-Ppy rods self-assembly is that SEM sample preparation for structures characterization involves a drying process which can easily alter the equilibrium configurations of yielding assemblies.

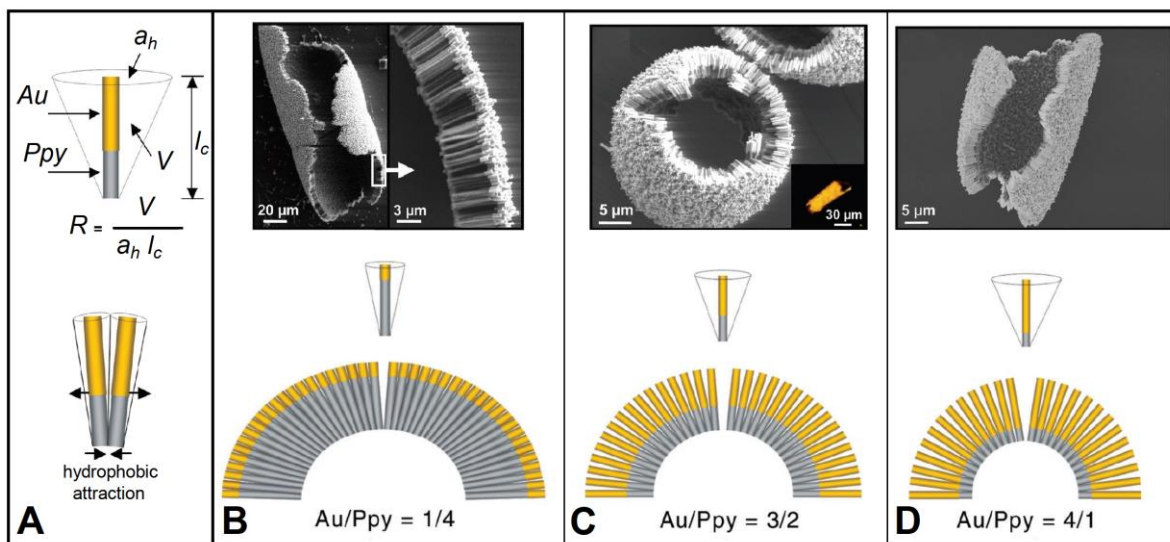


Fig.0.15. (A) Sketch of the Au-Ppy patchy rod and its geometrical packing factor R . SEM images of tubular superstructures formed by Au-Ppy patchy rods and their schematic representation for (B) 1:4, (C) 3:2, and (D) 4:1 gold-to-polymer ratio [42].

As a perspective, one can be also interested in how patchy rods behave as a function of particle concentration. If aspect ratio of patchy rod is sufficiently high, what would the effect of enthalpic patch on their predominantly entropy-driven liquid crystalline self-assembly? The dynamical properties of patchy rod-like colloids have not been investigated yet in the experimental studies either [41], [42]. Therefore the central goal of this thesis is to synthesize suitable patchy colloidal system and to investigate its structural and dynamical properties in a wide range of particle concentrations. Besides, following the idea of Hubert *et al.* [64], the combination of entropic and enthalpic patchiness can be realized on colloidal rods adding depletion agents into dispersions of particles with enthalpic patches.

0.4 Fd-virus as a model system of colloidal rods

In this section, we will review the experimental achievements which have been done so far on the structural and dynamical properties of colloidal dispersions made of fd-viruses which are the main experimental system in this study.

Fd-virus is a semiflexible rod-like polyelectrolyte formed by a cylindrical shell composed of around 3000 copies of the major coat protein (p8) which wrap in a helical way a circular single stranded DNA [44]. Thus fd is a chiral object displaying a helical charge distribution. There are five copies each of four minor proteins capping the two ends of the virion: p7 and p9 on one end and p3 and p6 on another end as depicted in Fig.0.16.

The conventional representative of fd strain is fd-wt (wild type) with a contour length of 880 nm and a diameter of 7 nm [62]. The persistent length of fd-wt is three times higher than its contour length $P_{fdwt} \sim 3L_{fdwt}$. Thanks to the ability to genetically modify the structure of filamentous viruses, the stiffer fd-Y21M mutant has been derived with single point mutation in the amino-acid sequence of each p8 protein [45]. The 21st amino acid of the major coat protein is changed from tyrosine to methionine. This mutation results in the increasing of the fd-Y21M length $L_{fdY21M} = 920 \text{ nm}$ [46] and, more importantly, of its persistent length $P_{fdY21M} \sim 10L_{fdY21M}$ [45]. Therefore fd-Y21M mutant has stiffness which is about three times higher than stiffness of fd-wt virus.

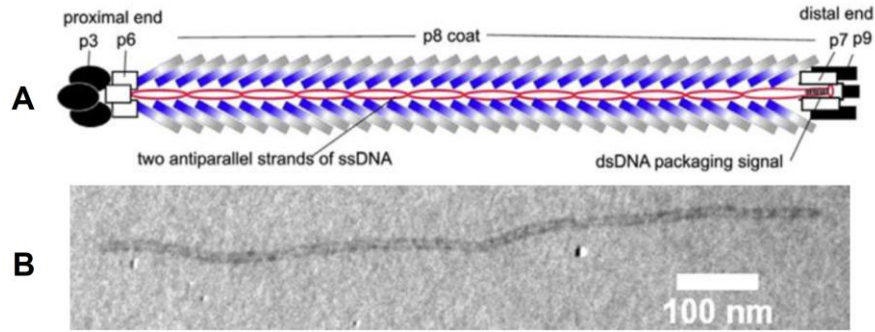


Fig.0.16. (A) Schematic representation of fd-virus (its length is of about $1 \mu\text{m}$ and its diameter is of 7 nm). It consists of around 3000 copies of major p8 protein enclosing a single strand DNA. There are also five copies of each minor coat proteins p7/p9 on one end, and proteins p3/p6 on another end. (B) Transmission electron microscopy (TEM) image of fd-virus. The two p7/p9 and p3/p6 ends cannot be discriminated in this TEM image.

There is a strain called M13 which is closely related to fd. M13 virus shares the same length, diameter and flexibility as fd, but it differs by one amino acids per major coat protein. There is negatively charged aspartate in 12th position in fd, and in M13 there is neutral asparagine. Thus the linear charge density is different for the two viruses: it is $10 e^-/\text{nm}$ for fd and $7 e^-/\text{nm}$ for M13 [65]. In this thesis we will use two longer mutants of M13 called M13KE and M13C7C which have the same diameter, stiffness and charge as M13, but they differ by their length which is of 1000 nm . M13KE and M13C7C themselves only differ by the number of cysteines groups in minor p3 tip proteins. The details will be provided in Chapter 1.

The filamentous viruses fd and M13 have been used as model systems of rod-like particles because of three important features. (i) They can be easily observed at the single particle level by optical microscopy [9]. (ii) Regardless of fd/M13 charge, they can be approximated as hard rods if the concept of effective diameter is introduced [9], [24]. (iii) The filamentous phages are essentially identical to each other, meaning that they are highly monodisperse in shape and size.

In this section, we will discuss the main structural and dynamical properties of fd-virus liquid crystalline suspensions, and will focus on the methods used for fd functionalization with fluorescent dye molecules.

0.4.1 Self-assembled structures in fd suspensions

The monodisperse chiral fd-viruses in water dispersion self-organize into chiral nematic (N^*), smectic (Sm) and columnar (Col) liquid-crystalline phases (Fig.0.17). In chiral nematic or

cholesteric phase, the director follows the helical path, as viruses prefer to twist with respect to each other. The cholesteric pitch P_0 is defined as the periodicity along the screw axis in which the local director has rotated by 2π (Fig.0.17A). Since the typical fd cholesteric pitch (from $20\mu\text{m}$ to $200\mu\text{m}$ [47]) is around three orders of magnitude larger than the interrod distance in cholesteric phase [9], locally chiral and usual nematic have the same structure. There is no difference in Onsager theory between isotropic-nematic and isotropic-cholesteric phase transition, as the free energy difference between the nematic and cholesteric phase is negligible compared to the one between the isotropic and nematic phase [69].

The location and coexistence concentrations of fd-wt isotropic-(chiral)nematic phase transition have been found experimentally [24] in a good agreement with numerical calculation of persistent polymers [66], [67], where Onsager theory [31] is generalized including rod flexibility. There is a necessity to involve the effect of the virus charge to find matching with Onsager theory, meaning that the bare fd diameter D must be rescaled by a charge-dependent effective hard-rod diameter D_{eff} ($D_{eff} > D$) which is proportional to the Debye screening length of the virus [65], [68].

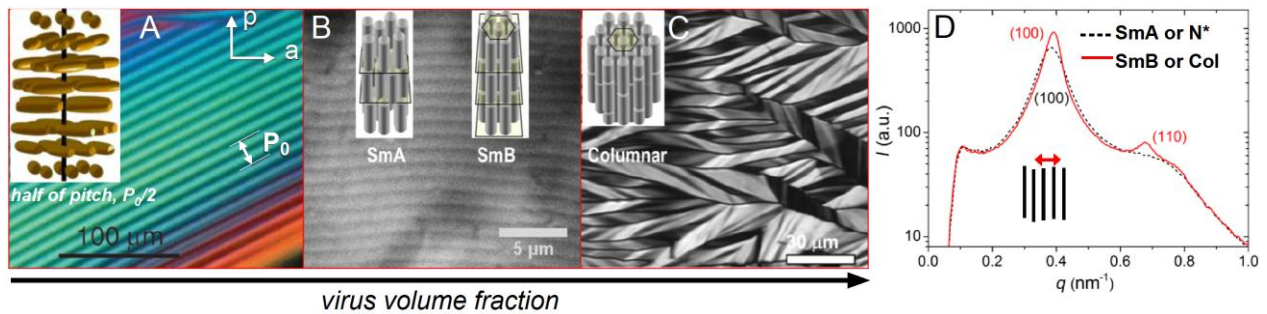


Fig.0.17. (A) Polarizing microscopy image of the chiral nematic or cholesteric phase formed by fd-viruses, where P_0 is cholesteric pitch; insert represent the twist of the director [47]. (B) Differential interference contrast microscopy (DIC) of the smectic phase formed by rod-like viruses; inserts illustrate liquid-like and positional order within smectic A and smectic B phases, respectively. (C) Optical texture of the columnar phase observed by polarizing microscopy. (D) Typical scattered intensity obtained by SAXS measuring the average interrod side-to-side distance. The dotted black line indicates the typical signature of liquid-like (smectic A and chiral nematic) and the solid red line indicates hexagonal positional order (smectic B and columnar). Bragg reflections (100) and (110) have been indexed according to the typical ratios of the

scattering vector $q:1:\sqrt{3}:\sqrt{4}:\sqrt{7}:\dots$ of a 2D hexagonal lattice corresponding, respectively, to the Miller indices (hkl) with the h , k , and l defined as the directions along the viruses [26].

The smectic phase includes the smectic A and the smectic B phases. In both cases viruses are arranged into layers stacked on top of each other, but the order within layers are different for two phases (Fig.0.17B insets). SAXS experiments reveal that smectic A possesses liquid-like order within the layer, whereas smectic B has long range hexagonal positional order [9]. To find a quantitative agreement between experimental [9], [25], computer simulations [32], [33] and theoretical [34] results on the values of the nematic-smectic A phase transition the virus charge also must be taken into account replacing a bare diameter D by an effective hard-rod diameter D'_{eff} [9]. D'_{eff} is determined via the Manning model of charge condensation which becomes significant in concentrated dispersions and usually neglected for dilute cases [70], [71], [106].

Columnar-smectic B phase transition is failed to be described by purely excluded volume interactions [36]. The existence of columnar phase in rod-like fd-virus suspension [26] may be explained by rod flexibility [72]. The structural analysis by means of SAXS experiments reveals that the short range positional ordering occurs suggesting a hexatic order. Such organization could be originating from a geometrical frustration induced by the competition between long range 2D translational order and helical twist due to the virus chirality [73]. This frustration is resolved by the introduction of topological defects which exist to accommodate two competitive orders as helical twist and positional order.

0.4.2 Dynamics in fd suspension

One of the fundamental dynamical characteristics of any colloidal suspension is the rate at which constituent particles diffuse. In colloidal liquid crystals, the self-diffusion depends on the degree of ordering of the system. For rod-like dispersions, in principle, three parameters of interest can be measured to describe the dynamical properties of the system. They are the translational diffusion coefficients D_{\parallel} and D_{\perp} for motion parallel and perpendicular to the rod long axis respectively, and the rotational diffusion D_r with respect to the rod long axis.

At the *infinite dilution* of rods in solvent, the particle diffusion is caused by the Brownian force and torque exerted on it by the thermal energy $k_B T$ coming from the surrounding solvent molecules. When a particle moves through a solvent of viscosity η_0 , it experiences a friction resulting in a hydrodynamic force for the translation and hydrodynamic torque for the rotation.

For long and thin rods of length L and diameter D these frictions coefficients for parallel and perpendicular motion are [77]:

$$\gamma_{\parallel} = 2 \frac{\pi\eta_0 L}{\ln(L/D)} \quad (0.10)$$

$$\gamma_{\perp} = 4 \frac{\pi\eta_0 L}{\ln(L/D)} \quad (0.11)$$

The friction coefficient for rotation is:

$$\gamma_r = \frac{\pi\eta_0 L^3}{3\ln(L/D)} \quad (0.12)$$

Hence, it is possible to express three corresponding diffusion coefficients:

$$D_{\parallel} = \frac{k_B T}{\gamma_{\parallel}}, D_{\perp} = \frac{k_B T}{\gamma_{\perp}}, \text{ and } D_r = \frac{k_B T}{\gamma_r} \quad (0.13)$$

We see that $\gamma_{\parallel} = 2\gamma_{\perp}$, meaning that the diffusion coefficient D_{\parallel} in the direction parallel to the rod axis is about twice larger than the one for the perpendicular diffusion D_{\perp} at the infinite rod dilution.

However, in the concentrated regimes, especially if there is positional and orientational order in the colloidal rod-like systems, the theoretical description of particle diffusion becomes complex due to spatial interaction between rods which has to be taken into account. Nevertheless, there are theoretical studies on the diffusion of rods in dense isotropic phase made by Doi [74], and in nematic phase made by Tang and Evans [75].

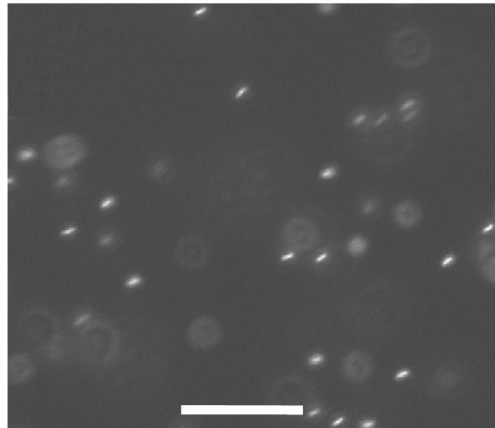


Fig.0.18. Image of fluorescently labeled rods dispersed in nematic matrix of unlabeled rods ($1:10^5$) [48]. Due to limited spatial resolution of optical microscope, labeled fd appears as a slightly anisotropic rod, even though its actual aspect ratio is of around 100. Scale bar: $5\mu\text{m}$.

Experimental studies on fd-virus *translational* diffusion in different liquid crystalline phases have been fruitful in the recent years. Although several techniques can be applied, such as

dynamic light scattering [76] or fast recovery after photobleaching [107], the most efficient and convenient method is the imaging and tracking of individual viruses with video microscopy. The motion of individual rods can be directly observed by fluorescence optical microscopy if they received labeling with fluorescent dye molecules (Fig.0.18). The details of labeling will be discussed in section 0.4.3. In order to characterize the dynamics of fd suspension, the mean square displacements (MSD) are measured relying on the individual trajectories r_i (i is id-number of a given particle) of the labeled viruses traced down by video microscopy. If there are N trajectories the expression for MSD in parallel and perpendicular directions in terms of the distance from the initial position $r_i(0)$ of each particle reads as follow:

$$MSD_{\parallel}(t) = \frac{1}{N} \sum_{i=1}^N \left(r_{i\parallel}(t) - r_{i\parallel}(0) \right)^2 \quad (0.14)$$

$$MSD_{\perp}(t) = \frac{1}{N} \sum_{i=1}^N \left(r_{i\perp}(t) - r_{i\perp}(0) \right)^2 \quad (0.15)$$

The parallel and perpendicular self-diffusion coefficients can be extracted from the following expression [49]:

$$MSD_{\parallel,\perp} = 2D_{\parallel,\perp} t^{\gamma} \quad (0.16)$$

The time evolution of MSD given by (0.14) and (0.15) provides also the value of diffusion exponent γ [49]: (i) case with $\gamma = 1$ represent unbiased random Brownian motion corresponding to the standart self-diffusion coefficients $D_{\parallel,\perp}$, (ii) $\gamma < 1$ is a signature of a subdiffusive behavior which appears in crowded systems [108], and finally (iii) $\gamma > 1$ is a characteristic of superdiffusion which can be observed for self-propelled or active particles [109]. It is worth stressing that if $\gamma \neq 1$, the parameters $D_{\parallel,\perp}$ should be regarded as the diffusion rates as they correspond to the unusual or non-Brownian motion.

The typical collection of fd-wd traces in concentrated isotropic and nematic phases near isotropic-nematic transition (nematic traces have been extracted from the movie represented in Fig.0.18A) and correspondent MSD are shown in Fig.0.19C, while the trajectory of a single particle in smectic A phase is depicted in Fig.0.20B. All traces in isotropic phase are spherically symmetric, meaning there is no preferred direction of motion, whereas those in nematic phase display a significant anisotropy. All nematic traces are aligned along nematic director showing much lower displacement perpendicular to it. In smectic A phase rods prefer to diffuse faster along the director as well. Furthermore, in nematic phase the parallel virus displacement is

continuous whereas in smectic A it exhibits discontinuous hopping-like diffusion through smectic layers [46], [49].

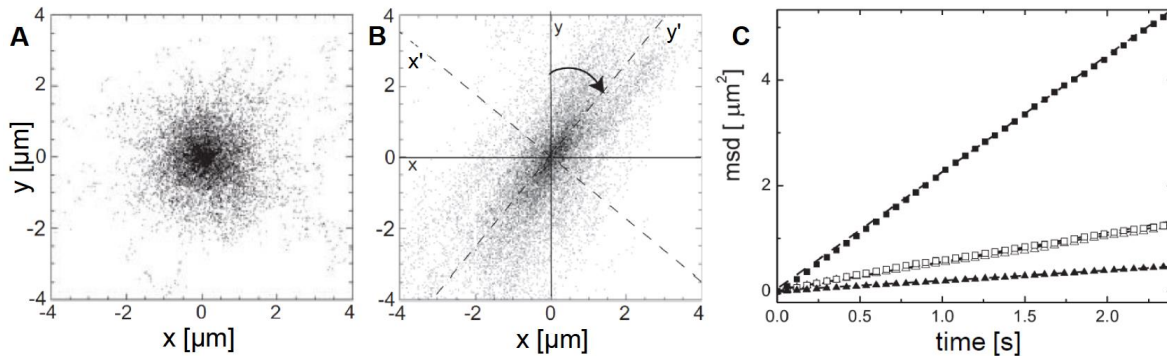


Fig.0.19. Collection of traces of fluorescently labeled viral particles in (A) isotropic phase, and (B) anisotropic traces in nematic phase; x' and y' indicate a new lab-frame in which the director is aligned along the y' -axis. (C) The mean square displacements of rods parallel to the director (full squares) and perpendicular to the director (full triangles) obtained for nematic phase. The isotropic mean square displacements are given by the open squares and triangles. The diffusion along the director in nematic phase is significantly enhanced when compared to the diffusion of isotropic phase, whereas the perpendicular diffusion is significantly suppressed [48].

The diffusion of fd-viruses along the director in nematic and smectic phase is strongly enhanced compared to isotropic phase, while the diffusion perpendicular to the director is reduced. The anisotropy in diffusion increases from $D_{\parallel}/D_{\perp} \approx 1$ to ≈ 10 after the isotropic-nematic phase transition and growing up to $D_{\parallel}/D_{\perp} \approx 20$ in smectic A phase. Moreover the total diffusion $D_{tot} = 1/3 (D_{\parallel} + 2D_{\perp})$ increases abruptly, directly proving the increase of translation entropy after isotropic-nematic phase transition predicted by Onsager [31].

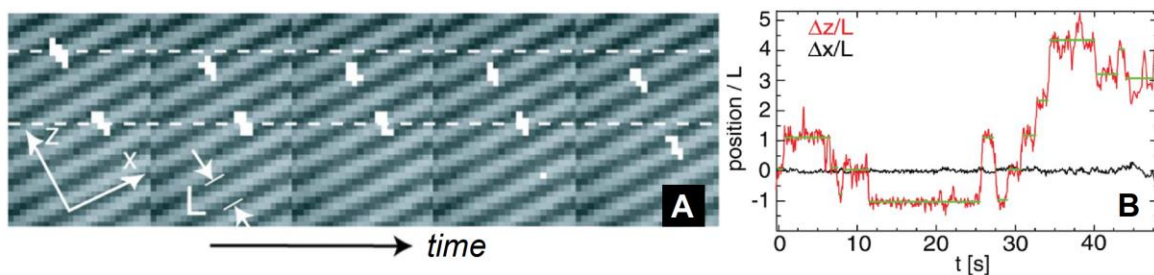


Fig.0.20. (A) Overlays of DIC and fluorescence optical microscopy images showing the time consecutive frames of jumping labeled virus (elongated whitish signal) through the smectic

A layers. (B) The displacement of chosen particle in the direction parallel (red) and perpendicular (black) to the director [49].

In the fd liquid crystalline phases with positional translational order (smectic B and columnar) no significant self-diffusion has been detected [50], [51], except rare (around one event per 12 hours for one particle) half- and full-rod-length jumps were observed in columnar phase (Fig.0.21).

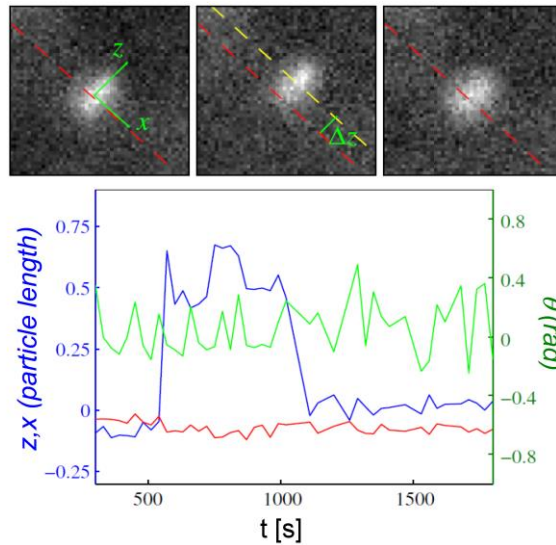


Fig.0.21. Half-jump motion of fd-virus in the columnar phase. Fluorescence images show the raw data where the dashed red line is drawn perpendicular to the long axis of the labeled particle and indicated its position at the initial time. The corresponding trajectory presents the dimensionless displacement along (z , blue line) and perpendicular (x , red line) to the long axis (director). Displacements are normalized by the particle length L . The green line indicate the relative orientation change of the particles in radians (right vertical axes) [50].

Although, the general features of the diffusional behavior of fd suspensions in isotropic, nematic, and smectic A phases, where self-assembly is driven by entropy, are studied, there is no study on the dynamics in suspensions where enthalpy contributes to the self-assembly. Thus, one of the goals of this thesis is to investigate the self-diffusion of patchy rods and to perform quantitative comparison with self-diffusion of pristine (purely repulsive) rods in all phases of fd dispersions.

0.4.3 Chemical functionalization of fd

Fd-viruses have proven their importance as a model system for investigation of colloidal liquid crystals [9], [24] and as a building block for assembly of the various targeted structures [37], [38], [53]. Another striking feature of fd-virus is the opportunity to perform chemical modifications on its surface. In the framework of this thesis, we will perform the fd-virus conjugation or labeling with fluorescent dye molecules. Here we distinguish two types of labeling, which are the *full body labeling* and the *tip labeling*. These two ways are used to fulfill distinct and independent purposes in our exploration by the fluorescence optical microscopy of structural and dynamical properties of the fd liquid crystalline suspension.

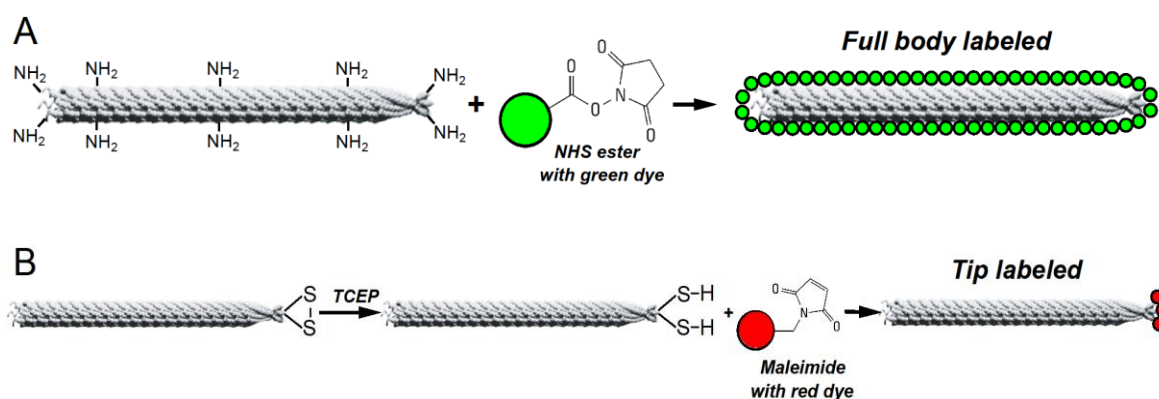


Fig.0.22. Schemes of labeling reaction on virus full body and tip. (A) The full body conjugation can be done by reaction between NH_2 group and NHS (N-hydroxysuccinimide) ester activated green dye molecules. (B) Tip conjugation can be performed only on p3 minor protein, where cysteine groups (S-S) reduced by TCEP (tris(2-carboxyethyl)phosphine) react with Maleimide activated red dyes.

Full body labeling has been done thanks to the NH_2 amine group (N-terminus) at the exposed to the solvent ends of each coat protein (p8, p3, p6, p7, p9) [54]. During the chemical reaction of labeling, NH_2 group links with N-hydroxysuccinimide (NHS) ester whose in turn can be bound to the dye molecule. In this thesis we chose green dyes for the virus body labeling (Fig.0.22A). Full body labeling is employed in this thesis to study dynamical properties of colloidal suspension via single particle tracking. We have been working within an assumption that the green dye molecules which cover the surface of whole particle do not affect the virus self-diffusion behavior in colloidal dispersions.

Tip labeling has been performed thanks to the exposed disulfide bridges (S-S groups) formed by cysteines on p3 proteins at one of the tips of fd-virus [54], [55]. Disulfide bridge

reduction to the thiols (*SH* groups) by tris(2-carboxyethyl)phosphine (*TCEP*) compound is required to conduct further reaction with Maleimide activated red fluorescent dye molecules [110] (Fig.0.22B). The same principle of regio-selective chemistry has been already successfully realized for the construction of the virus based colloidal multiarm structured [56], where biotin has been used instead of red dye molecules. In our study, the primary purpose of the virus tip labeling is the creation of enthalpic patchiness. The fluorescent dye molecules are partially hydrophobic [111] due to the presence of aromatic rings. This leads to the localized attractions or “patchiness” between viral ends. The secondary purpose is the visualization by fluorescence microscopy of the local structure of virus colloidal suspensions with improved optical resolution and contrast. Fd-virus tip labeling reaction used in this thesis has been developed and optimized by Cheng WU [110], a former PhD student in our group.

The *combined labeling* of virus surface is also performed to be able to observe the self-diffusion of patchy viral particles. In this case we initially conduct tip labeling with red dyes, and then full body labeling with green dyes.

0.5 Linear topological defects in lamellar liquid crystalline ordering

The large variety of different phases displayed by lyotropic (concentration dependent) and thermotropic (temperature dependent) liquid crystals has led to investigate at least two major fields of soft matter science: phase transition theory (global symmetry breakings) and defect theory (local symmetry breaking) [82]. Topological defects are crucial to understand ordered and disordered systems, frustrated media, and phase transitions [80-82].

In this section, we will specifically introduce the linear defects in liquid crystalline structures with lamellar organization, and review the main experimental results on their observation and structural analysis in smectic phase of molecular liquid crystals.

0.5.1 Elastic properties of nematic and smectic A liquid crystals

Because of quasi-liquid nature of nematic liquid crystals, they can be treated as media that have continuum or elastic properties [84], [85]. For example, nematic phase, which is a one-dimensional ordered fluid where the particles are orientationally ordered and are aligned in average along common direction \mathbf{n} , called director, but have no long range positional order, can

be treated as an elastic fluid. There are three possible elastic deformations of its structure: splay, twist, and bend deformations as shown schematically in Fig.0.23A-C. These deformations have the following Frank elastic constants associated with them, respectively, K_1, K_2, K_3 . The free energy per unit volume f can be written as follow ($q_0 = 2\pi/p$ is related to the pitch p in the chiral nematic case if any) [80], [90]:

$$f = \frac{1}{2}K_1(\nabla \cdot \mathbf{n})^2 + \frac{1}{2}K_2(\mathbf{n} \cdot \nabla \times \mathbf{n} + q_0)^2 + \frac{1}{2}K_3[\mathbf{n} \times (\nabla \times \mathbf{n})]^2 \quad (0.17)$$

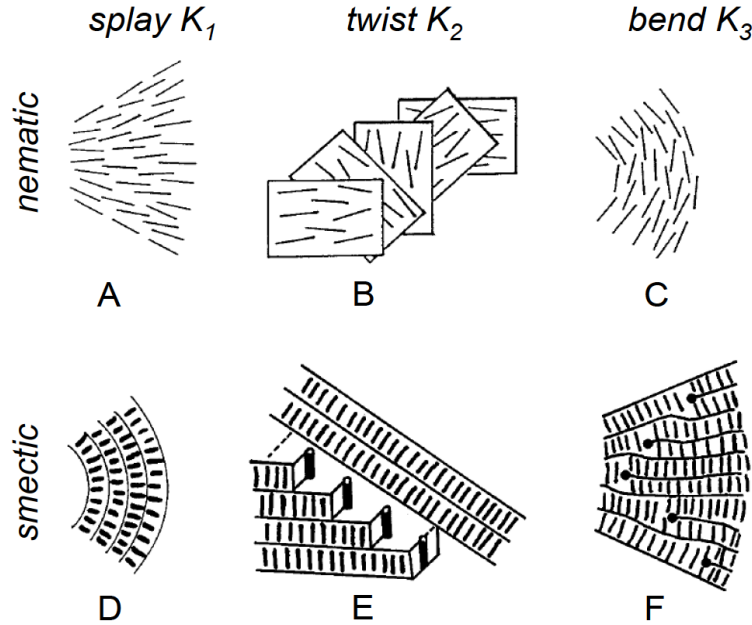


Fig.0.23. (A)-(C) Basic deformation modes of a nematic director field: (A) splay deformation ($\nabla \cdot \mathbf{n} \neq 0$); (B) twist deformation ($\mathbf{n} \cdot \nabla \times \mathbf{n} \neq 0$); and (C) bend deformation ($\mathbf{n} \times (\nabla \times \mathbf{n}) \neq 0$). (D)-(F) The same deformations of the director field in a smectic phase. Only splay deformation of the director field (D) is compatible with the constant layer spacing. A twist deformation (E) [bend deformation (F)] is only possible if screw dislocations [edge dislocations] are introduced [83].

In contrast to the (chiral) nematic phase, the smectic A phase shows a layered structure which is incompatible with a director field $\mathbf{n}(\mathbf{r})$ which is twisted or bent. This consideration means that terms containing $\nabla \times \mathbf{n}$ cannot occur in smectic liquid crystals [86], [87]. Indeed, experiments on thermotropic liquid crystals have shown that the pitch p and the elastic coefficients K_2 and K_3 of the chiral nematic phase increase strongly in the vicinity of smectic A

phase and diverge at the nematic-smectic A transition [88], [89]. The only way to twist or to bend the director field of a lamellar structure is to insert so-called screw- or edge-dislocations, respectively (Fig.0.23 E, F).

Dislocations are linear defect with broken translation symmetry. The screw dislocations impose a change of orientation of the smectic layer through the axial direction of the sample, and the rotation in the lateral packing of the rods becomes localized at defect core. The edge dislocations are characterized by the breaking of continuity of a smectic layer, where a new layer appears (Fig.0.24). The vector that represents the magnitude and direction of the lattice distortion, called Burger vector \mathbf{b} , is parallel to the dislocation line in the case of a screw dislocation, whereas it is perpendicular to the dislocation line for an edge dislocation.

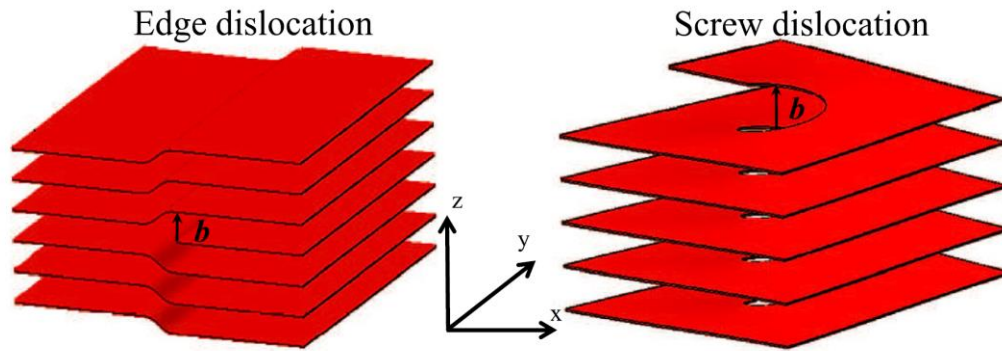


Fig.0.24. Schemes of a screw and an edge dislocations. The Burger vector \mathbf{b} is parallel to the dislocation line along the z -axis for a screw dislocation and it is perpendicular to the dislocation line along the y -axis for an edge dislocation.

In smectic phase density of elastic free energy (0.17) has to be supplemented by a term which accounts for layer compressibility [80]:

$$f_{elastic} = \frac{1}{2}B \left(\frac{\partial u}{\partial n} \right)^2 \quad (0.18)$$

In this expression, u is the displacement field, and B is the compressibility modulus. Taking into account $\nabla \times \mathbf{n} = \mathbf{0}$, and introducing the elastic length $\lambda = \sqrt{K_1/B}$ (typical length scale over which an exerted distortion relaxes in lamellar systems), we can rewrite the free energy density for smectic as [80], [92]:

$$f_{smectic} = \frac{1}{2}B \left[\left(\frac{\partial u}{\partial n} \right)^2 + \lambda^2 (\nabla \cdot \mathbf{n})^2 \right] \quad (0.19)$$

By accounting only linear derivatives in the displacement field u , the solution of (0.19) for screw dislocation with Burger vector \mathbf{b} and defect core axis along z -axis (Fig.0.24) can be exactly minimized as [82], [91], [93]:

$$u_{screw} = \frac{b}{2\pi} \tan^{-1} \left(\frac{y}{x} \right) \quad (0.20)$$

In the case of a single edge dislocation with Burger vector \mathbf{b} along y -axis (Fig.0.24), the solution of equation (0.19) is also known [82], [91]:

$$u_{edge} = \frac{b}{4} \left[1 + \operatorname{erf} \left(\frac{x}{\sqrt{4\lambda z}} \right) \right] \quad (0.21)$$

where $\operatorname{erf}(\dots)$ is the error function.

The expression (0.21) is valid only for the edge dislocations where Burger scalar b is much lower than the elastic length ($b \ll \lambda$). To describe the general case when $b \sim \lambda$ or $b \gg \lambda$ the higher-order derivatives terms must be added to the displacement field u in the expression for the free energy density (0.19) which yields the nonlinear exact solution for u :

$$u_{edge}^{nonlinear} = 2\lambda \ln \left[1 + \frac{e^{b/4\lambda} - 1}{2} \left\{ 1 + \operatorname{erf} \left(\frac{x}{\sqrt{4\lambda z}} \right) \right\} \right] \quad (0.22)$$

0.5.2 Screw and edge dislocation in molecular liquid crystals

Although dislocations play an important role in liquid crystals determining many static and dynamic properties of these materials [94]-[98], quantitative experimental analysis of displacement field around dislocations and detailed structure of their cores remains scarce to the date [99]. Recently observations of screw and edge dislocations have been reported in liquid crystal material made of bent-shape molecules *E9* [100] (Fig.0.25) by employing cryogenic transmission electron microscopy (Cryo-TEM), and in ordered films of PS/PBMA diblock copolymers by using atomic force microscopy (AFM) [112].

For a screw dislocation the width of defect core (blank region between red and green layer on the bottom sketch for Fig.0.25A) is found to be less than 5nm, which is nearly equal to the smectic interlayer spacing, and is in agreement with the “melted” (nematic or isotropic) model of the core proposed for thermotropic smectic A phase by Pleiner [101], [102]. Using equation (0.21) the elastic length λ of *E9* liquid crystalline material has been estimated from the edge

dislocation profile shown in Fig.0.25B. The experimental findings provided an approximate value for λ which has the same order of magnitude as the value of smectic interlayer spacing.

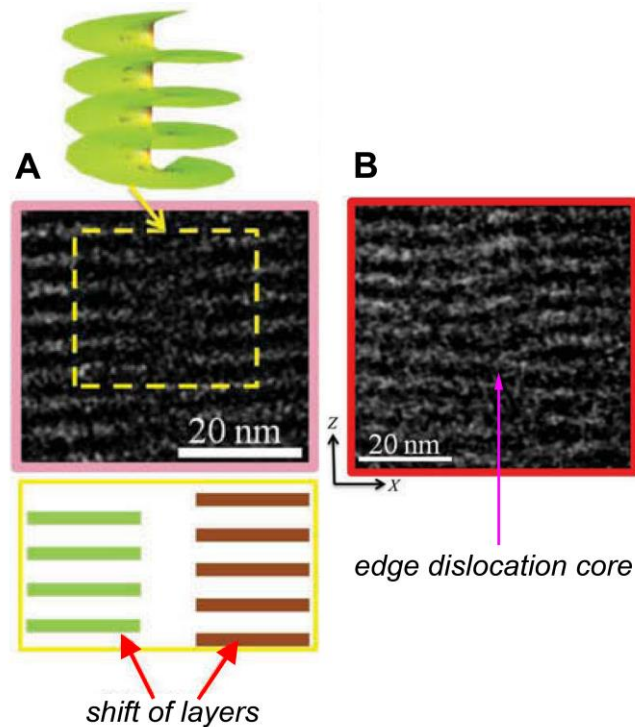


Fig.0.25. TEM-images of (A) a screw dislocation with 3D model of its core on the top and cross section of the smectic layers on the bottom, and (B) an edge dislocation in bent-shape liquid crystal material E9 [100].

From this demonstration, we can conclude that investigation of dislocations depends on the quality of their visualization at length scale corresponding to smectic layer periodicity, which is typically of several nanometers for molecular systems. This results in poorly resolved images as we can see in Fig.0.25. Therefore it could be very useful to take advantage of the micrometer range smectic periodicity of, for instance, lyotropic fd-virus liquid crystalline dispersion, and perform observation of dislocation in this system gaining highly resolved optical images. Specifically, one might expect to probe the detailed structure in dislocation core via, for example, observation of particle self-diffusion within it. The local order within the dislocation core is expected to be “melted” into a higher-symmetry phase; (nematic or isotropic), but it does not receive yet an experimental confirmation [103], [104].

0.6 Outline of the thesis

The recognition that entropic and enthalpic patchinesses can lead to diverse morphologies assembled at the microscale has inspired the development of numerous chemical methods for creating novel types of colloidal particles with selective and directional interactions [7], [8]. In our group we exploit the fact that the functionalization by patchy inclusions can be locally performed at one of the single tips of filamentous viruses [56], producing a new sort of shape-anisotropic particles with enthalpic patchiness. As the experimental studies of phase behavior and dynamics of patchy rods are scarce to the date [41], [42], it has motivated us to investigate the effect of highly localized attractive interaction on the structural and dynamical properties of fd-virus liquid crystalline colloidal dispersions. Therefore, the aim of this thesis is to study the phase diagram and the dynamical features of fd-virus dispersions with tunable directional attraction and to compare the obtained results to that of pristine i.e. purely repulsive particles.

In Chapter 1, the structural properties of viral particles with highly localized directional attractive interaction are studied. Firstly, we employ the regiospecific surface functionalization to achieve the local attraction between rod tips. Then we show that the strength of the resulting attractive interaction can be tuned by using different fd-virus mutants and by varying the dye molar excess during the chemical reaction. Computer simulations performed by the group from Eindhoven University of Technology is used to get deeper insight into the effect of directional attraction on self-assembly of rod-like colloids. Experimental phase diagram of patchy viruses as a function of their volume fraction and the interaction strength is thus constructed and compared to the simulation phase behavior of modeled patchy rods. As the liquid crystalline behavior of tip-functionalized rods is highly sensitive to the mutual positions between patchy inclusions in different phases, particular attention of our analysis is devoted to the smectic ordering due to the high correlation of sticky particle ends in this organization.

In Chapter 2, we show how the dye molecules on the rod tips are used to observe the liquid crystalline lamellar structure by fluorescence microscopy with improved resolution and contrast. Thanks to this, the visualization of linear topological defects in the smectic phase, called edge and screw dislocations, is performed at the lattice periodicity level. The detailed structure of defect cores is evidenced, as well as displacement field around an edge dislocation is calculated and compared to the theoretical predictions [78], [79]. “Melted” ordering within the screw

dislocations is revealed thanks to the self-diffusion experiments performed at the individual particle level.

In Chapter 3, we focus our attention on the dynamical features of tip-functionalized viral suspensions. Dynamics in all liquid crystalline states of both patchy and pristine rods is investigated by tracking individual particle displacements by fluorescence microscopy. To characterize the differences between the two types of viruses, their mean square displacements, and thus self-diffusion coefficients, are experimentally measured and compared. Local diffusion of patchy rods assembled into layered reminiscent of smectic ordering in the nematic and isotropic phases are also presented.

Finally in Chapter 4, we combine the effects of entropic and enthalpic patchiness. Non-absorbing polymers are added into pristine as well as tip-functionalized viral dispersions inducing effective attraction between rod sides. Structural and dynamical properties of non-functionalized and tip-grafted particles under depletion interaction are studied by optical microscopy and small angle X-ray scattering techniques with the determination of the experimental phase diagrams.

In the general conclusion, we summarize all the results obtained for dispersions of filamentous viruses with highly localized directional attractive interaction. Some perspectives of this work are also discussed including further ideas for combination of entropic and enthalpic patchiness, as well as varying the position of localized attraction on rod surface to achieve new types of virus based superstructures.

0.7 References

- [1] A. Einstein. Investigation on the theory of the Brownian movement. *Dover, New York*, 1926.
- [2] J. Perrin. Les atomes. *Constable, London*, 1923.
- [3] P. N. Pusey and W. van Megen. Phase behaviour of concentrated suspensions of nearly hard colloidal spheres. *Nature*, 1986, 320: 340–342.
- [4] U. Gasser, E. R. Weeks, A. Schofield, P. N. Pusey, and D. A. Weitz. Real-space imaging of nucleation and growth in colloidal crystallization. *Science*, 2001, 292: 258-262.

-
- [5] Z. Wang, F. Wang, Y. Peng, Z. Zheng, and Y. Han. Imaging the homogeneous nucleation during the melting of superheated colloidal crystals. *Science*, 2012, 338: 87–90.
- [6] D. G. A. L. Aarts, Matthias Schmidt, and H. N. W. Lekkerkerker. Direct visual observation of thermal capillary waves. *Science*, 2004, 304: 847-850.
- [7] S. C. Glotzer and M. J. Solomon. Anisotropy of building blocks and their assembly into complex structures. *Nat. Mater.*, 2007, 6: 557–562.
- [8] N. D. Burrows, A. M. Vartanian, N. S. Abadeer, E. M. Grzincic, L. M. Jacob, W. Lin, J. Li, J. M. Dennison, J. G. Hinman, and C. J. Murphy. Anisotropic nanoparticles and anisotropic surface chemistry. *J. Phys. Chem. Lett.*, 2016, 7: 632-641.
- [9] E. Grelet. Hard-rod behavior in dense mesophases of semiflexible and rigid charged viruses. *Phys. Rev. X*, 2014, 4: 21053.
- [10] A. Kuijk, Dmytro V. Byelov, Andrei V. Petukhov, A. van Blaaderen, and A. Imhof. Phase behavior of colloidal silica rods. *Faraday Discuss.*, 2012, 159: 181-199.
- [11] Q. Chen, S. C. Bae, and S. Granick. Directed self-assembly of a colloidal kagome lattice. *Nature*, 2011, 469: 381–384.
- [12] B.V. Derjaguin and L. Landau. Theory of the stability of strongly charged lyophobic sols and of the adhesion of strongly charged particles in solutions of electrolytes. *Acta Physicochimica USSR*, 1941, 14: 633.
- [13] E.J.W. Verwey and J. Th. Overbeek. Theory of the stability of lyophobic colloids. *Elsevier, Amsterdam*, 1948.
- [14] H. N. W. Lekkerkerker and R. Tuinier. Colloids and the Depletion Interaction. *Springer*, 2011.
- [15] S. Asakura, and F. Oosawa. On interaction between two bodies immersed in a solution of macromolecules. *J. Chem. Phys.*, 1954. 22: 1255-1256
- [16] A. Vrij. Polymers at interfaces and the interactions in colloidal dispersions. *Pure & Appl. Chem.*, 1976, 48: 471-483.
- [17] M. Maldovan, and E. L. Thomas. Diamond-structured photonic crystals. *Nat. Mater.*, 2003, 3: 593-600.
- [18] A. Lomakin, N. Asherie, and G. B. Benedek. Aeolotropic interactions of globular proteins. *PNAS*, 1999, 96: 9465-9468.

- [19] A. V. Petukhov, R. Tuinier, G. J. Vroege. Entropic patchiness: effects of colloid shape and depletion. *Curr. Opin. in Coll. & Int. Sc*, 2017, 30: 54-61.
- [20] N. Kern, and D. Frenkel. Fluid–fluid coexistence in colloidal systems with short-ranged strongly directional attraction. *J. Chem. Phys.*, 2003, 118: 9882-9889.
- [21] L. Hong, A. Cacciuto, E. Luijten, and S. Granick. Clusters of amphiphilic colloidal spheres. *Langmuir*, 2008, 24; 621-625.
- [22] L. Hong, A. Cacciuto, E. Luijten, and S. Granick. Clusters of charged Janus spheres. *Nano Lett.*, 2006, 6: 2510-2514.
- [23] S. Fraden, G. Maret, D. L. D. Caspar, and R. B. Meyer. Isotropic-nematic phase transition and angular correlations in isotropic suspensions of tobacco mosaic virus. *Phys. Rev. Lett.*, 1989, 63: 2068-2071.
- [24] J. Tang and S. Fraden. Isotropic-cholesteric phase transition in colloidal suspensions of filamentous bacteriophage. *Liq. Cryst.*, 1995, 19: 459–467.
- [25] Z. Dogic and S. Fraden. Smectic Phase in a Colloidal Suspension of Semi flexible Virus Particles. *Phys. Rev. Lett.*, 1997, 78: 2417–2420.
- [26] E. Grelet. Hexagonal order in crystalline and columnar phases of hard rods. *Phys. Rev. Lett.*, 2008, 100: 168301.
- [27] A. Kuijk, A. van Blaaderen, and A. Imhof. Synthesis of monodisperse, rodlike silica colloids with tunable aspect ratio. *JACS*, 2011, 133: 2346-2349.
- [28] P. A. Buining, A. P. Philipse, and H. N. W. Lekkerkerker. Phase behavior of aqueous dispersions of colloidal boehmite rods. *Langmuir*, 1994, 10: 2106-2114.
- [29] O. Pelletier, P. Davidson, C. Bourgaux and J. Livage. The effect of attractive interactions on the nematic order of V_2O_5 gels. *Europhys. Lett.*, 1999, 48: 53-59.
- [30] H. Maeda. Atomic force microscopy studies for investigating the smectic structures of colloidal crystals of β -FeOOH. *Langmuir*, 1996, 12: 1446-1452.
- [31] L. Onsager. The effects of shape on the interaction of colloidal particles. *Ann. N. Y. Acad. Sci.*, 1949, 51: 627–659.
- [32] D. Frenkel., H. N. W. Lekkerkerker, and A Stroobants. Thermodynamic stability of a smectic phase in system of hard rods. *Nature*, 1988, 332: 822-823.
- [33] P. Bolhuis, and D. Frenkel. Tracing the phase boundaries of hard spherocylinders. *J. Chem. Phys.*, 1997, 106: 666-687.

-
- [34] B. Mulder. Density-functional approach to smectic order in an aligned hard-rod fluid. *Phys. Rev. A*, 1987, 35: 3095-3101.
- [35] B. de Braaf, M. O. Menegon, S. Paquay, and P. van der Schoot. Self-organisation of semi-flexible rod-like particles. *J. Chem. Phys.*, 2017, 147: 244901.
- [36] S. Dussi, M. Chiappini, and M. Dijkstra. On the stability and finite-size effects of a columnar phase in single-component systems of hard-rod-like particles. *Molecular Physics*, 2018.
- [37] E. Barry and Z. Dogic. Entropy driven self-assembly of nonamphiphilic colloidal membranes. *PNAS*, 2010, 107: 10348–10353.
- [38] B. Sung, A. de la Cotte, and E. Grelet. Chirality-controlled crystallization via screw dislocations. *Nat. Commun.*, 2018, 9: 1405.
- [39] S. Sacanna, W. T. M. Irvine, P. M. Chaikin, and D. J. Pine. Lock and key colloids. *Nature*, 2010, 464: 575–578.
- [40] L. Rossi, S. Sacanna, W. T. M. Irvine, P. M. Chaikin, D. J. Pine, and A. P. Philipse. Cubic crystals from cubic colloids. *Soft Matter*, 2011, 7: 4139–4142.
- [41] K. Chaudhary, Q. Chen, J. J. Juárez, S. Granick, and J. A. Lewis. Janus colloidal matchsticks. *JACS*, 2012, 134: 12901–12903.
- [42] S. Park, J-H. Lim, S.-W. Chung, and C. A. Mirkin. Self-Assembly of Mesoscopic Metal-Polymer Amphiphiles. *Science*, 2004, 303: 348-351.
- [43] J. N. Israelachvili. Intermolecular and Surface Forces. *Third Edition, Elsevier*, 2011.
- [44] D. Marvin. Filamentous phage structure, infection and assembly. *Curr. Opin. Struct. Biol.*, 1998, 8: 150–158.
- [45] E. Barry, D. Beller, and Z. Dogic. A model liquid crystalline system based on rodlike viruses with variable chirality and persistence length. *Soft Matter*, 2009, 5: 2563–2570.
- [46] E. Pouget, E. Grelet, and M. P. Lettinga. Dynamics in the smectic phase of stiff viral rods. *Phys. Rev. E*, 2011, 84: 41704.
- [47] Z. Dogic and S. Fraden. Cholesteric phase in virus suspensions. *Langmuir*, 2000, 16: 7820–7824.
- [48] M. P. Lettinga, E. Barry, and Z. Dogic. Self-diffusion of rod-like viruses in the nematic phase. *Europhys. Lett.*, 2005, 71: 692–698.

- [49] M. P. Lettinga and E. Grelet. Self-diffusion of rodlike viruses through smectic layers. *Phys. Rev. Lett.*, 2007, 99: 197802.
- [50] S. Naderi, E. Pouget, P. Ballesta, P. van der Schoot, M. P. Lettinga, and E. Grelet. Fractional hoppinglike motion in columnar mesophases of semiflexible rodlike particles. *Phys. Rev. Lett.*, 2013, 111: 37801.
- [51] L. Alvarez, M. P. Lettinga, and E. Grelet. Fast Diffusion of Long Guest Rods in a Lamellar Phase of Short Host Particles. *Phys. Rev. Lett.*, 2017, 118: 178002.
- [52] E. Grelet, and S. Fraden. What Is the Origin of Chirality in the Cholesteric Phase of Virus Suspensions? 2003, 90: 198302.
- [53] T. Gibaud *et al.* Reconfigurable self-assembly through chiral control of interfacial tension. *Nature*, 2012, 481: 348–351.
- [54] D. A. Marvin, M. F. Symmons, and S. K. Straus. Structure and assembly of filamentous bacteriophages. *Prog. Biophys. Mol. Biol.*, 2014, 114: 80–122.
- [55] A. Kremser and I. Rasched. The adsorption protein of filamentous phage fd: assignment of its disulfide bridges and identification of the domain incorporated in the coat. *Biochemistry*, 1994, 33: 13954—13958
- [56] A. de la Cotte, C. Wu, M. Trévisan, A. Repula, and E. Grelet. Rod-like virus based multiarm colloidal molecules. *ACS Nano*, 2017, 11: 10616-10622.
- [57] Q. Chen, J. Yan, J. Zhang, S. C. Bae, and S. Granick. Janus and multiblock colloidal particles. *Langmuir*, 2012, 28: 13555–13561.
- [58] F. C. Bawden, and N. W. Pirie. The isolation and some properties of liquid crystalline substances from solanaceous plants infected with three strains of tobacco mosaic virus. *Proc. R. Soc. Lond. B*, 1937, 123: 274-320.
- [59] R. F. Kayser, Jr. and H. J. Raveche. Bifurcation in Onsager's model of the isotropic-nematic transition. *Phys. Rev. A*, 1978, 17: 2067-2072.
- [60] S. Spaltro, K.P. Ananthapadmanabhan, M. Frushour, and M. Aronson. Adsorption of dextrans onto hydroxyapatite: presence of maxima. *Coll. and Surf.*, 1992, 68: 1-8.
- [61] K. Devanand, and J. C. Selser. Asymptotic behavior and long-range interactions in aqueous solutions of poly(ethylene oxide). *Macromolecules*, 1991, 24: 5943-5947.
- [62] J. Sambrook and W. D. Russell. Molecular cloning. A laboratory manual, 4th Ed. *Cold Spring Harbor Laboratory Press: New-York*, 2012.

- [63] M. Siavashpouri *et al.* Molecular engineering of chiral colloidal liquid crystals using DNA origami. *Nat. Mater.*, 2017, 49.
- [64] C. Hubert *et al.* Synthesis of multivalent silica nanoparticles combining both enthalpic and entropic patchiness. *Faraday Discuss.*, 2015, 181: 139–146.
- [65] K. R. Purdy and S. Fraden. Isotropic-cholesteric phase transition of filamentous virus suspensions as a function of rod length and charge. *Phys. Rev. E*, 2004, 70: 61703.
- [66] A. R. Khokhlov and A. N. Semenov. Liquid-crystalline ordering in the solution of partially flexible macromolecules. *Physica*, 1982, 112A: 605-614.
- [67] Z. Y. Chen. Nematic ordering in semiflexible polymer chains. *Macromolecules*, 1993, 26: 3419-3423.
- [68] G. J. Vroege, and H. N. W. Lekkerkerker. Phase transitions in lyotropic colloidal and polymer liquid crystals. *Rep. Prog. Phys.*, 1992, 55: 1241-1309.
- [69] A. Saupe. Recent results in the field of liquid crystals. *Angew. Chem. internat. Edit.* 1, 1968, 7: 97-112.
- [70] G. S. Manning. Counterion condensation on charged spheres, cylinders, and planes. *J. Phys. Chem. B*, 2007, 111: 8554-8559.
- [71] E. Trizac, M. Aubouy, and L. Bocquet. Analytical estimation of effective charges at saturation in Poisson–Boltzmann cell models. *J. Phys.: Condens. Matter*, 2003, 15: 291–296.
- [72] R. Hentschke *et al.*, *Phys. Rev. A*, 1991, 44: 1148.
- [73] R. D. Kamien *et al.*, *Phys. Rev. Lett.*, 1995, 74: 2499.
- [74] M. Doi. Rotational relaxation time of rigid rod-like macromolecule in concentrated solution. *Le Journal De Physique*, 1975, 36: 607-611.
- [75] S. Tang, and G. T. Evans. Self-diffusion in isotropic and nematic phases of highly elongated hard particles. *J. Chem. Phys.*, 1993, 98: 7281.
- [76] J. Newman, and H. L. Swzney. Hydrodynamic Properties and Structure of fd Virus. *J. Mol. Biol.*, 1977, 116: 593-606.
- [77] J. M. Burgers. Second report on viscosity and plasticity. *Amsterdam Academy of Science Nordeman, Amsterdam*, 1938, chap. 3.
- [78] E. A. Brener, and V. I. Marchenko. Nonlinear theory of dislocations in smectic crystals: An exact solution. *Phys. Rev. E*, 1999, 59: R4752.

- [79] T. Ishikawa, and O. D. Lavrentovich. Dislocation profile in cholesteric finger texture. *Phys. Rev. E*, 1999, 60: R5037.
- [80] M. Kleman, and O. D. Lavrentovich. Soft Matter Physics: An Introduction. *Springer-Verlag, New York*, 2002.
- [81] P. M. Chaikin, and T. C. Lubensky. Principles of Condensed Matter Physics. *Cambridge Univ. Press, Cambridge*, 1995.
- [82] M. Kleman. Defects in liquid crystals. *Rep. Prog. Phys.*, 1989, 52: 555-654
- [83] H.-S. Kitzerow. Chirality in Liquid Crystals, Chapter: Twist Grain Boundary Phases. *Springer, New York, NY*, 2001.
- [84] P. Collings, M. Hird. Introduction to Liquid crystals: Chemistry and Physics. *Taylor and Francis, London*, 1997.
- [85] F. Leslie in: G.W. Gray , D. Demus , H.W. Spiess , J.W. Goodby , V. Vill. Handbook of Liquid Crystals, Vol I, *Wiley-VCH, Weinheim*, 1998.
- [86] S. Chandrasekhar. Liquid Crystals, 2nd ed. *Cambridge University Press, Cambridge*, 1992.
- [87] P.G. de Gennes. *Solid State Commun.* 1973, 10: 753.
- [88] L. Cheung, R.B. Meyer, and H. Gruler. *Phys. Rev. Lett.*, 1973, 31: 349.
- [89] R.S. Pindak, C.-C. Huang, and J.T.Ho. *Phys. Rev. Lett.* 1974, 32: 43-46.
- [90] F. C. Frank. I. Liquid crystals. On the theory of liquid crystals. *Disc. of the Far. Soc.*, 1958, 25: 19.
- [91] M. Kleman. Points, Lines and Walls. *Wiley, New York*, 1983.
- [92] C. D. Santangelo. Geometry and the nonlinear elasticity of defects in smectic liquid crystals, *Liq. Crys. T.*, 2006, 15: 11-18.
- [93] P. G. de Gennes, J. Prost. The Physics of Liquid Crystals(2nd edition). *Oxford University Press, New York*, 1993.
- [94] M. Kleman and J. Friedel. Disclinations, dislocations, and continuous defects: A reappraisal. *Rev. Mod. Phys.*, 80, 61 2008.
- [95] R. B. Meyer, B. Stebler, and S. T. Lagerwall. Observation of edge dislocations in smectic liquid crystals. *Phys. Rev. Lett.*, 1978, 41:1393.
- [96] R. D. Kamien and T. C. Lubensky. Chiral lyotropic liquid crystals: TGB phases and helicoidal structures. *J. Phys II France*, 1997, 7: 157.

-
- [97] R. P. Trivedi, I. I. Klevets, B. Senyuk, T. Lee, and I. I. Smalyukh. Reconfigurable interactions and three-dimensional patterning of colloidal particles and defects in lamellar soft media. *PNAS*, 2012, 109: 4744.
- [98] H. Aharoni, T. Machon, and R. D. Kamien. Aspects of Defect Topology in Smectic Liquid Crystals. *Phys. Rev. Lett.*, 2017, 118: 257801.
- [99] P. Oswald and P. Pieranski. Smectic and Columnar Liquid Crystals: Concepts and Physical Properties Illustrated by Experiments. *Taylor and Francis/CRC Press, London*, 2005.
- [100] C. Zhang *et al.* Cryo-TEM studies of two smectic phases of an asymmetric bent-core material. *Liq. Cryst.*, 2013, 12: 1636-1645.
- [101] H. Pleiner. Structure of the core of screw dislocations in smectic-A liquid-crystals. *Liq Cryst.*, 1986, 1:197–201.
- [102] H. Pleiner. Energetics of screw dislocations in smectic-A liquid-crystals. *Liq Cryst.*, 1988, 3:249–258.
- [103] C. D. Muzny, and N. A. Clark. Direct observation of the brownian motion of a liquid-crystal topological defect. *Phys. Rev. Lett.*, 1992, 6:804–807.
- [104] R. L. Blumberg Selinger. Diffusion in a smectic liquid crystal with screw dislocations. *Phys. Rev. E*, 2002, 5: 1–4.
- [105] W. G. Hoover and F. H. Ree. Melting Transition and Communal Entropy for Hard Spheres. *J. Chem. Phys.*, 1968, 49: 3609.
- [106] G. S. Manning. Counterion Condensation on Charged Spheres, Cylinders, and Planes. *J. Phys. Chem. B*, 2007, 111, 8554.
- [107] A. van Blaaderen. Long-time self-diffusion of spherical *colloidal particles measured with fluorescence recovery after photobleaching*. *J. Chem. Phys.*, 1992, 96, 4591.
- [108] E. R. Weeks, D. A. Weitz. Subdiffusion and the cage effect studied near the colloidal glass transition. *Chem. Phys.*, 2002, 284: 361–367.
- [109] W. Wang, W. Duan, S. Ahmed, A. Sen, and T. E. Mallouk. From one to many: Dynamic assembly and collective behavior of self-propelled colloidal motors. *Acc. Chem. Res.*, 2015, 48: 1938–1946.
- [110] C. Wu. Hybrid colloidal molecules from self-assembly of viral rod-like particles. *PhD thesis, University of Bordeaux*, 2018.

- [111] Z. Zhang and E. Grelet. Tuning chirality in the self-assembly of rod-like viruses by chemical surface modifications. *Soft Matter*, 2013, 9, 1015.
- [112] M. Maaloum et al. Edge profile of relief 2D domains at the free surface of smectic copolymer thin films. *Phys. Rev. Lett.*, 1992, 68, 1575.

Chapter 1

Directing liquid crystalline self-organization of rod-like particles through tunable attractive single tips

This part of thesis has been done in collaboration with Mariana Oshima Menegon and Paul van der Schoot from Eindhoven University of Technology (TUE), as well as with Cheng Wu, former PhD student in our group. The team from TUE has performed computer simulations to deeper investigate the effect of local directional interaction on structural properties of rod-like liquid crystalline colloidal dispersions. The results have been published in *Physical Review Letters* in 2019. Thus, we present this published paper as Chapter 1.

Filamentous viruses self-organize into various phases by tuning rod concentration including isotropic liquid, chiral nematic, smectic (or lamellar), and columnar states. This phase behavior has been shown to be nearly mapped by hard-core interaction between colloidal particles [18], [20]. In this Chapter, we go beyond purely repulsive interaction between rods, and study the structural properties of viral particles with highly localized directional attractive interaction (or “patchiness”). Local attraction is achieved by functionalizing the proximal ends of filamentous viruses via regioselective grafting of hydrophobic fluorescent dyes. Interaction strength between viral tips is shown to be tuned by employing different fd mutants and varying dye molar excess during chemical reactions. In computer simulations, filamentous virus is modeled as a chain of overlapping beads connected via springs. One of the end beads of each chain represents the patch on the tip of rod-like colloid and interacts attractively with other end beads, whereas it repels via hard-core interaction the rest of the beads forming chains.

We establish and compare experimental and simulations phase diagrams as a function of rod concentration and attraction strength between their tips. Local ordering of patchy viruses in different liquid crystalline mesophases is visualized by fluorescent optical microscopy and compared to the assemblies of modeled rods with sticky end beads.

Directing liquid crystalline self-organization of rod-like particles through tunable attractive single tips

Andrii Repula,¹ Mariana Oshima Menegon,² Cheng
Wu,¹ Paul van der Schoot,^{2,3} and Eric Grelet^{1,*}

¹*Centre de Recherche Paul-Pascal, CNRS & Université de Bordeaux,
115 Avenue Schweitzer, F-33600 Pessac, France*

²*Department of Applied Physics, Eindhoven University of Technology,
PO Box 513, 5600 MB Eindhoven, The Netherlands*

³*Institute for Theoretical Physics, Utrecht University,
Princetonplein 5, 3584 CC Utrecht, The Netherlands*

(Dated: March 18, 2019)

Abstract

Compelling justification: Hard-core repulsion is the simplest interaction in Nature yet it drives the self-organization of many complex fluids. To investigate how enthalpy impacts upon entropy-dominated liquid crystalline states, we introduce a highly localized and tunable directional attractive interaction (or “patch”) on one of the tips of rod-shaped colloids. Our experiments and computer simulations show that increasing the patch attraction dramatically stabilizes the lamellar phase, a structure desired in materials science due to its outstanding mechanical and optical properties. Our work demonstrates that introducing patches in anisotropic nanoparticles adds to the control of their self-assembly.

Abstract: Dispersions of rod-like colloidal particles exhibit a plethora of liquid crystalline states, including nematic, smectic A, smectic B, and columnar phases. This phase behavior can be explained by presuming the predominance of hard-core volume exclusion between the particles. We show here how the self-organization of rod-like colloids can be controlled by introducing a weak and highly localized directional attractive interaction between one of the ends of the particles. This has been performed by functionalizing the tips of filamentous viruses by means of regioselectively grafting fluorescent dyes onto them, resulting in a hydrophobic patch whose attraction can be tuned by varying the number of bound dye molecules. We show, in agreement with our computer simulations, that increasing the single tip attraction stabilizes the smectic phase at the expense of the nematic phase, leaving all other liquid crystalline phases invariant. For sufficiently strong tip attraction the nematic state may be suppressed completely to get a direct isotropic liquid-to-smectic phase transition. Our findings provide insights into the rational design of building blocks for functional structures formed at low densities.

* eric.grelet@crpp.cnrs.fr

There is a considerable interest in the self-organization of fluid dispersions of nanoparticles into hierarchical structures and morphologies. On the one hand, there is a fundamental interest in elucidating the physical principles that govern the self-assembly of colloidal particles [1]. On the other hand, there is also a technological interest in the context of fabricating novel functional materials bottom-up, that is, via self-assembly [2, 3]. For both reasons, anisometric building blocks are seen as highly promising systems, because of their versatility in surface functionalization and their ability to form complex architectures, as the liquid crystalline phases [4–13].

Among the desired organizations relevant in the context of materials science and nanotechnology, layered structures stand out for their outstanding optical and mechanical properties [14–17]. Such lamellar or smectic phases usually appear at relatively high packing fractions, which tend to render them difficult to handle experimentally. [17–19]. It would therefore be appealing to develop methods and approaches to obtain the smectic ordering at lower particle loadings. We have recently shown that the self-organization and phase stability of highly ordered liquid crystalline states of filamentous viruses, including the smectic phases, is dominated by volume exclusion and hence by entropy [20], confirming the role of model colloidal system of these biological rods.

Here, we go beyond relying on a purely hard-core interaction and homogeneous surface functionalization [21, 22], and introduce a tunable localized directional attraction between the tips of the virus particles by specifically grafting hydrophobic fluorescent dyes to one of the two ends of our virus-based colloidal rods. We investigate experimentally the impact of this “enthalpic” patch on the self-assembly behavior of the particles and compare our findings with computer simulations. The regioselective functionalization of the tips of the rods into hydrophobic patches gives rise to highly localized attractive interactions, which strongly influence the relative stability and structure of the various liquid crystalline phases. In particular, we show how an increasing tip attraction stabilizes the smectic A phase at the expense of the nematic and eventually also the isotropic phase, extending the stability of the smectic A phase to relatively low concentrations. We demonstrate in this Letter the efficiency of introducing a single attractive patch in the design of anisotropic building blocks to sensitively control the balance between entropy and enthalpy, and thus to control the self-organization of these particles into the desired architecture.

In our experiments, we made use of mutants of the filamentous bacteriophages M13KE

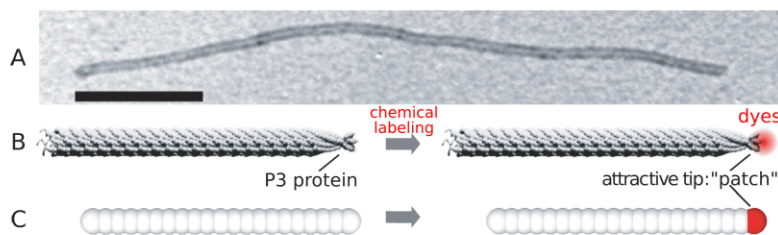


FIG. 1. **(A)** Transmission electron microscopy of the filamentous virus used in this work (Scale bar: 200 nm), and **(B)** schematic representation of pristine (left) and single-tip functionalized viral rod with red dyes (right), resulting in a localized directional attractive interaction. **(C)** Schematic of the semi-flexible rod-like particles, modeled as a bead-spring chain, used in computer simulations. The white beads from different particles interact via a repulsive soft-core potential, while the red ones located at one end of the rods are attractive.

and M13C7C, which only differ by the number of cysteine groups available at their proximal end on the P3 proteins (Fig. 1A-B). Both viruses are rod-shaped with a contour length of $L = 1 \mu\text{m}$, and a diameter of 7 nm . The particles are semi-flexible with a persistence length of $L_p \simeq 3L$ [23]. The presence of cysteine residues only at one of the ends allows, after chemical reduction, for their selective bioconjugation with maleimide activated fluorescent compounds (Dylight 550 and 594 Maleimide, ThermoFisher), as described elsewhere [24, 25]. This results in single-tip labeled viruses, whose degree of functionalization, i.e., the average number of fluorescent dyes per virus can be controlled in our experiments from $n_{\text{dyes}} = 1, 3$ to 10 by varying the molar excess during the labeling reaction (See the Supplemental Material [26].)

The dye molecules are partially hydrophobic due to the presence of aromatic rings [21], implying that the number of grafted dye molecules dictates the size of the hydrophobic patch on the otherwise hydrophilic surface of the virus. It is reasonable to presume that the strength of the attraction between the virus tips increases with the patch area. Whether there is a linear relationship between the number of dyes and the strength of the attraction is contentious, as the cysteine reduction and dye labeling leads to partial unfolding of the P3 tip proteins. This causes hydrophobic moieties of buried amino acids to become exposed to the aqueous solution. Still, it seems reasonable to assume that the number and size of these exposed hydrophobic groups increases with the degree of labeling, as confirmed by our experiments (See the discussion below).

Samples of single-tip functionalized virus suspensions have been prepared by dilution with BisTris-HCl-NaCl buffer, setting the pH at 7 and the ionic strength at 20 mM. These are then studied by optical microscopy [25] and small angle X-ray scattering (SAXS, [20]) (see the Supplemental Material [26]). In our molecular dynamics simulations, we model the chiral filamentous virus particles as achiral overlapping bead-spring chains, where 21 beads are connected via springs of rest length measuring half bead diameter and very large spring constant (Fig. 1C). Therefore, the aspect ratio of the simulated particles is 11, which is smaller by about one order of magnitude than the effective (i.e. accounting for the electrostatic repulsion between the charged viruses [20]) aspect ratio of the experimental particles. The consequences for the comparison between results from experiments and simulations are discussed below. The beads interact via a steeply repulsive potential. A bending potential has been introduced to mimic the flexibility of the virus particles in order to reproduce the ratio between the persistence and contour lengths of the virus, $L_p/L \sim 3$. One of the end beads (displayed in red in Fig. 1C) representing the labeled virus patch interacts attractively through a Lennard-Jones potential with the other tip beads, and with a purely repulsive interaction with the other beads forming the rod particles. The strength of the tip attraction u is the depth of the Lennard-Jones potential. Approximately 4600 chains are placed in size-adjustable simulation box initially organized in 8 AAA-stacked bilayers. We performed NPT simulations at various pressures, using the simulation package LAMMPS according to a method described in [27].

We construct the experimental phase diagram for patchy rods as a function of the concentration and the degree of functionalization (Fig. 2A), and compare this with the phase behavior of the pristine viral particles. By comparing the stability limits of the various mesophases, which includes nematic, smectic A, smectic B and columnar phases, we conclude that increasing the number of dye molecules grafted at the tips of the virus particles strongly affects the nematic-smectic A (N-SmA) transition, yet has almost no effect over the other phase transitions. Our main finding is the increased stabilization of the smectic phase, at the expense of the nematic phase, with increasing number of grafted dyes, and concomitant widening phase gap implying that the transition becomes more strongly first order.

Figure 2B presents our simulation phase diagram as a function of the strength of the tip attraction, u . The resulting phase behavior shows qualitative agreement with the ex-

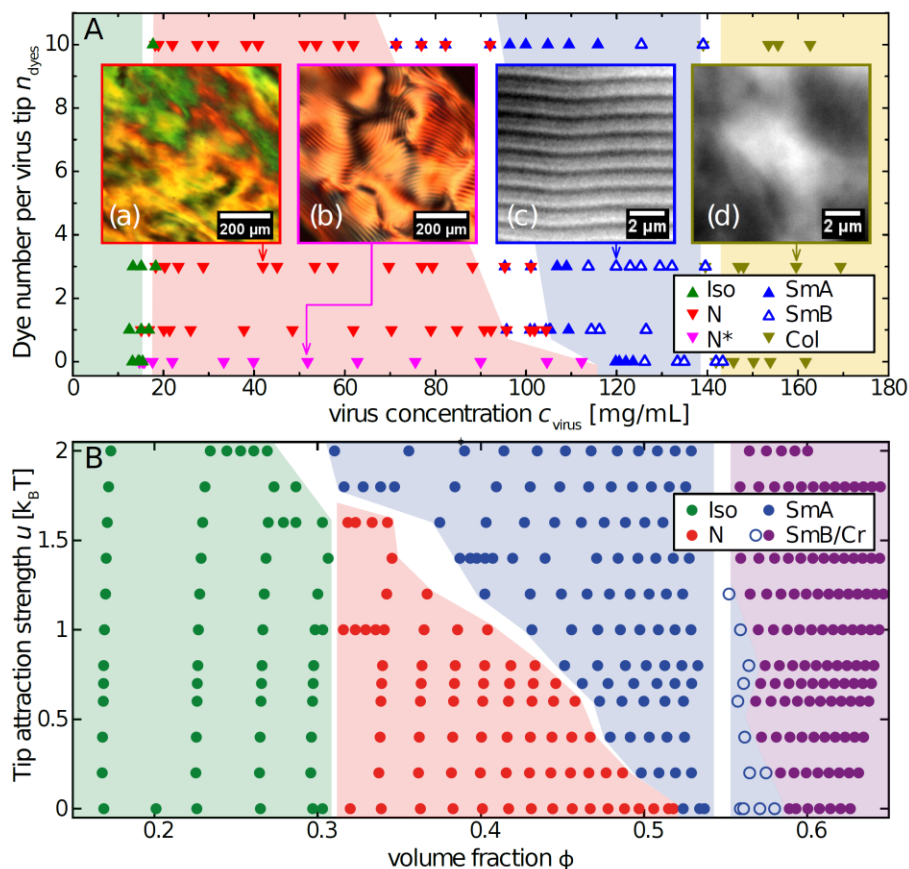


FIG. 2. **(A)** Phase diagram of tip-functionalized viruses as a function of the mean number of grafted dyes per rod n_{dyes} and the concentration c_{virus} . The system with 0 dyes corresponds to pristine (“raw”) viruses and the systems with $n_{\text{dyes}} = 1, 3,$ and 10 dyes represent the tip-functionalized, patchy particles. The isotropic liquid (Iso) and (chiral) nematic ($N^{(*)}$) phases (Images (a) and (b)) have been identified by polarizing microscopy. The layered texture observed by differential interference contrast (DIC) microscopy in the image (c) is characteristic of the smectic A (SmA) and B (SmB) phases, and it lacks in the columnar (Col) phase (d). The color coding for the different phases is given in the inset, and white regions indicate the phase gaps between the coexisting phases. **(B)** Calculated phase diagram in terms of the attraction strength u between the end groups of the semi-flexible rod-like particles as a function of their volume fraction ϕ . The different phases from isotropic liquid to the crystalline (Cr) state have been identified using global order parameters, as described in [27].

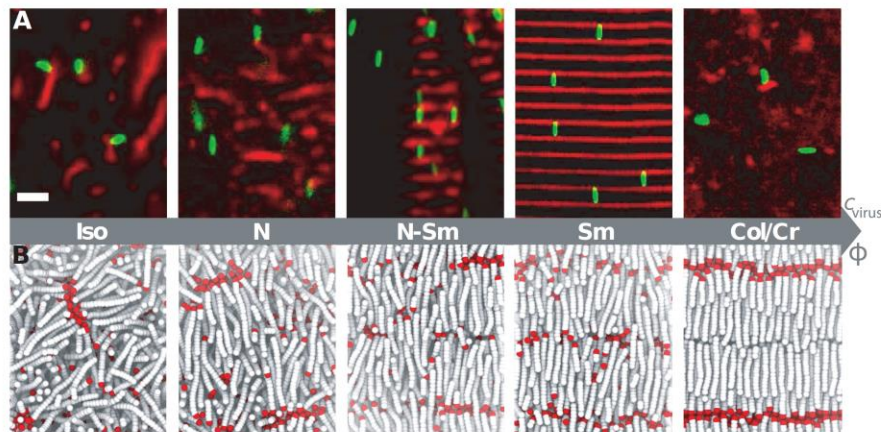


FIG. 3. **(A)** Optical textures of tip-labeled virus suspensions in the various liquid crystalline phases obtained by fluorescence microscopy. The red signal corresponds to the position of the patchy virus tips. The green signal represent body-functionalized viruses, which are added in a tracer amount to the suspension. Scale bar: $2 \mu\text{m}$. **(B)** Corresponding simulation snapshots highlighting the local ordering within the mesophases. White beads are purely repulsive and red ones are attractive. In the isotropic phase (Iso), the viruses have random orientations. In the nematic phase (N), viral particles have an average alignment along the director but no long-range positional order. There are some clusters in both phases, which are interpreted as precursors of smectic layers. The first order nematic-smectic A phase transition (N-SmA) is confirmed by the presence of sharp interface between the coexisting phases. In the smectic phases (SmA and SmB), all patches are localized in the interlayer spacing. Conversely, in the columnar phase (Col), the virus patches are uniformly distributed. In this mesophase, body-functionalized viruses are not aligned due to small domain size.

perimental data: increasing the stickiness of the tips affects mainly the nematic-smectic A phase transition. The stability of the smectic A phase increases with increasing strength of the tip attraction, as does the phase gap. For large enough attraction $u \gtrsim 1.8k_B T$, we find in our simulations a direct isotropic liquid-to-smectic A phase transition, exploring a range of attraction that we cannot access experimentally due to the limited number of exposed cysteine groups at the virus tip (see the Supplemental Material [26]). The isotropic liquid-to-nematic phase (I-N) transition remains unchanged in both phase diagrams, except for the highest tip attraction where the simulations point at a relatively weak widening of the coexistence range. This suggests that our patchy interaction is rather weak and localized,

as rods with stronger attractive interaction, driven by either depletion interaction [28, 29] or by a residual van der Waals interactions between the bodies of the rods [30], exhibit a significant widening of the I-N coexistence range.

The results from our experiments and the simulations diverge at very high packing fractions. We do not find a stable columnar phase in our simulations of rod-like particles. This could be due to the difficulty of stabilizing the columnar organization in numerical simulations for entropy driven, single-component systems [31]. It is also possible that the columnar phase does not form in suspensions of particles with aspect ratios below 30, as suggested in [32]. Another obvious difference between experiments and simulations is the strongly first order transition between the smectic A and smectic B phases in the latter. Experimentally, it is second order or weakly first order [20]. An extension of the smectic-B range by increasing the tip attraction that we find experimentally, is lacking in simulations for which there is also an intrinsic difficulty to clearly distinguish between the smectic B from the crystalline phase. The absence of one-to-one correspondence between the mass concentration in the experiments and the volume fraction in the simulations is not really surprising given the crude nature of the interaction potential, the modest aspect ratio of the particles in the simulations, and the overestimation of the size of the attractive bead in the simulations compared to the size of the attractive sites on the virus tip-proteins.

The overall qualitative agreement between experiments and simulations is however manifest. This is true for the dependence on tip attraction of the transitions between isotropic, nematic and smectic A phases (Fig. 2), but turns out to be true as well as for the local ordering displayed in these phases (Fig. 3). For the purpose of direct comparison, we added a tracer amount of body labeled viruses with green fluorescent dyes to our suspensions. The striking feature of the optical texture as seen by fluorescence microscopy is the presence of red colored clusters in the isotropic phase. By varying the depth of focus, we evidence the clusters to have a two-dimensional structure, forming bilayer “lamellae” in which the viruses assemble at their red tips and lie nearly perpendicular to them. We cannot exclude the possibility that some of these clusters are caused by chemical rather than physical cross-linking, during the tip functionalization process.

Similar lamellar structures can be observed in the nematic phase, except that in this case they are oriented perpendicular to the director (defined as the average rod orientation) whereas in the isotropic phase they are randomly oriented (Fig. 3A). Furthermore, the

disappearance of the chiral nematic or cholesteric phase in favor of the uniaxial nematic phase upon grafting even a single dye molecule to the virus tip (Fig. 2A), we ascribe to the presence of these lamellae. We argue that they must interfere with the chirality amplification on the mesoscopic scale. In our simulations we observe bilayer clusters similar to those seen experimentally with particles assembled by their attractive tips in both sides, as shown by the snapshots in the isotropic and nematic phases displayed in Fig. 3B.

At increased particle concentration, the lamellar aggregates grow and condense into smectic domains in a nematic background, corresponding to the N-SmA coexistence region (See Fig. 3, central images). As expected, the particles are aligned along the director in the two phases, in both experiments and simulations. An example of the single smectic domain is given in Fig. 3A, where the alignment of the rod-like particles is perpendicular to the layer allowing us to rule out any smectic C or other types of tilted smectic.

In contrast to the smectic A and B phases, which we are able to distinguish by means of SAXS measurements (see the Supplemental Material [26])[20, 33], and which do exhibit large single domains, the columnar phase is characterized by finite domain sizes of only a few micrometers width, as shown both in Figs. 2A and 3A. The absence of bright red localized signals supports the lack of layered structure and is therefore consistent with the liquid-like order along the columns. The variation of red fluorescence intensity arguably does not reflect strong clustering, but may be interpreted as the result of the integration over the sample thickness of the fluorescence signal coming from domains with different orientations.

As the main effect of the tip patchiness is to widen the smectic stability range, we have characterized this phase by determining the associated molecular field U_{layer} [34]. This unidimensional ordering potential can be obtained by measuring the distribution of longitudinal rod fluctuations with respect to the middle of the layers, from which the probability $P(z)$ of finding a particle at position z along the director. $P(z)$ is related to the ordering potential via the Boltzmann factor $P(z) \propto \exp(-U_{\text{layer}}(z)/k_B T)$. The free energy landscape of both experimental and simulated particles is presented in Fig. 4 and shows the same trends: (i) the magnitude of the ordering potential increases with increasing tip patchiness for a given particle packing fraction (Fig. 4A-B), and (ii) U_{layer} increases with the particle concentration, for both repulsive and attractive tips (Fig. 4C-D). Note in addition that the smectic potential also becomes narrower with increasing density and functionalizing the tips of the viruses. This implies that the amplitude of the fluctuations of the particles around their

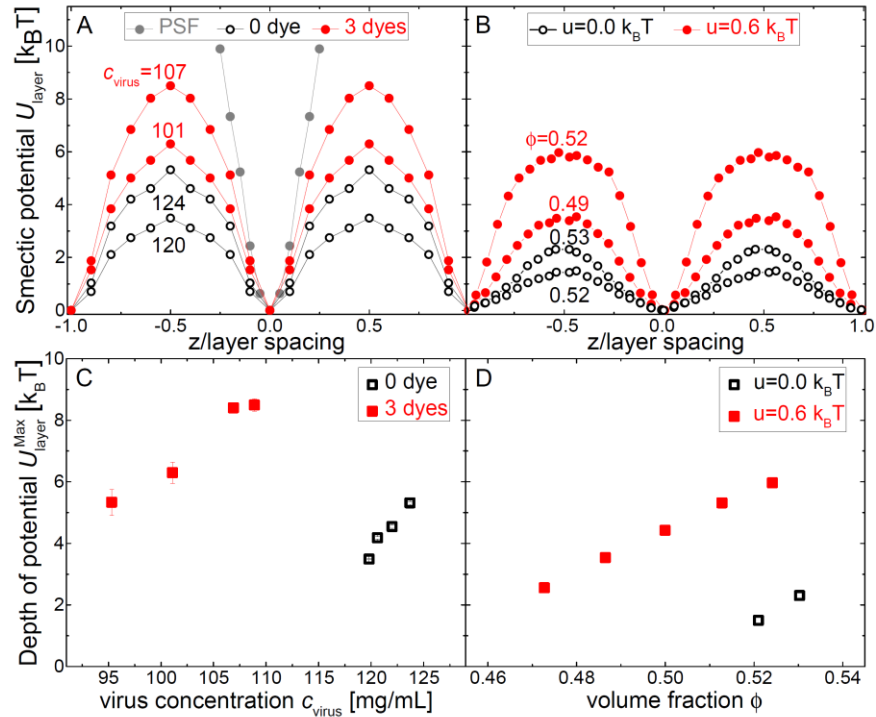


FIG. 4. Smectic ordering potentials or molecular fields calculated from experimental (A) and simulated (B) distribution of particles, as a function of the particle position, normalized by the smectic layer spacing, for different particle concentrations and volume fractions. In gray we indicate the experimentally measured potential of immobile particles, which is the equivalent for potentials of the point spread function (PSF) of the optical setup. Smectic potential barriers as a function of virus concentration for experiments (C) and as a function of volume fraction for simulations (D). In all graphs, open black and full red symbols correspond to “raw” repulsive and tip-functionalized rod-like particles, respectively.

equilibrium positions in the layers become weaker, and hence that the particle positions become more localized. As the aspect ratio of the particles is smaller in our numerical simulations, we expect lower smectic potentials compared to the experimental ones, as shown in Fig. 4. The reason is that the stability of the smectic A phase of repulsive rod-like particles reduces with decreasing length [35]. Notice that irrespective of the strength of tip attraction, we find the same slope of the ordering potential as a function of the particle concentration, both in the experiments and the simulations. This is to be expected because the molecular field a test particle experiences in a lyotropic smectic must be proportional to the average density [36]. Even though we have not been able to find a sensible mapping between our

experimental and simulation results because of the large disparity between the respective aspect ratios of the particles, our simulations do account for most of the features we observe in our experimental system. This is true both for the phase behavior and ordering potentials, suggesting that our prediction that a tip attraction strength as small as $u \approx 1 - 2 k_B T$ is sufficient to fully suppress the nematic phase and promote the smectic organization in dispersions of otherwise mutually repelling rod-like particles is plausible. This small value is actually not surprising, considering that free energy differences between particles in co-existing liquid crystalline phases of rod-like particles are typically of the order of a thermal energy and often much smaller than that.

In summary, we report on the achievement of tip-functionalized rod-like virus particles exhibiting sticky patches with tunable interaction. We find that the range of stability of the smectic phase of these particles can be enlarged continuously by increasing the strength of the patch attraction. Extending the stability of the smectic phase to lower concentrations happens at the expense of the nematic phase, in which bilayer lamellar aggregates form. Other phase transitions are, by and large, not affected by the tip functionalization. Our experiments and computer simulations suggest that the reason why only the smectic ordering responds to the tip functionalization, is that it brings together the interacting ends that are otherwise not highly correlated in the other phases. Our findings open up perspectives in the rational design and site-specific post-modifications of particulate building blocks for soft self-assembled materials, showing how the introduction of a single and tiny enthalpic patch is able to steer the structuring of complex fluids.

ACKNOWLEDGMENTS

This project has received funding from the European Union Horizon 2020 research and innovation programme under the Marie Skłodowska-Curie Grant Agreement No. 641839.

-
- [1] S. C. Glotzer and M. J. Solomon, *Nat. Mater.* **6**, 557 (2007).
 - [2] M. Grzelczak, J. Vermant, E. M. Furst, and L. M. Liz-Marzan, *ACS Nano* **4**, 3591 (2010).
 - [3] K. Zhao and T. G. Mason, *Rep. Prog. Phys.* **81**, 126601 (2018).

- [4] H. Zhang, J. K. Nunes, S. E. A. Gratton, K. P. Herlihy, P. D. Pohlhaus, and J. M. DeSimone, *New J. Phys.* **11**, 075018 (2009).
- [5] K. Chaudhary, J. J. Jurez, Q. Chen, S. Granick, and J. A. Lewis, *Soft Matter* **10**, 1320 (2014).
- [6] Y. Gao, A. K. Balin, R. P. A. Dullens, J. M. Yeomans, and D. G. A. L. Aarts, *Phys. Rev. Lett.* **115**, 248301 (2015).
- [7] Y. Gao, F. Romano, R. P. A. Dullens, J. K. Doye, and D. G. A. L. Aarts, *Phys. Rev. Materials* **2**, 015601 (2018).
- [8] N. F. Steinmetz, A. Bize, K. C. Findlay, G. P. Lomonosoff, M. Manchester, D. J. Evans, and D. Prangishvili, *Advanced Functional Materials* **18**, 3478 (2008).
- [9] Y. J. Lee, H. Yi, W.-J. Kim, K. Kang, D. S. Yun, M. S. Strano, G. Ceder, and A. M. Belcher, *Science* **324**, 1051 (2009).
- [10] T. Gibaud, E. Barry, M. Zakhary, M. Henglin, A. Ward, Y. Yang, C. Berciu, R. Oldenbourg, M. Hagan, D. Nicastro, R. Meyer, and Z. Dogic, *Nature* **481**, 348 (2012).
- [11] M. Nakata *et al.*, *Science* **318**, 1276 (2007).
- [12] M. Salamonczyk *et al.*, *Nat. Commun.* **7**, 13358 (2016).
- [13] G. Nyström and R. Mezzenga, *Current Opinion in Colloid & Interface Science* **38**, 30 (2018).
- [14] J.-C. P. Gabriel, F. Camerel, B. J. Lemaire, H. Desvaux, P. Davidson, and P. Batail, *Nature* **413**, 504 (2001).
- [15] S. Z. Butler, S. M. Hollen, L. Cao, Y. Cui, J. A. Gupta, H. R. Gutierrez, T. F. Heinz, S. S. Hong, J. Huang, A. F. Ismach, E. Johnston-Halperin, M. Kuno, V. V. Plashnitsa, R. D. Robinson, R. S. Ruoff, S. Salahuddin, J. Shan, L. Shi, M. G. Spencer, M. Terrones, W. Windl, and J. E. Goldberger, *ACS Nano* **7**, 2898 (2013).
- [16] S. Ferrari, E. Bianchi, and G. Kahl, *Nanoscale* **9**, 1956 (2017).
- [17] J. H. Lee, B. Fan, T. D. Samdin, D. A. Monteiro, M. S. Desai, O. Scheideler, H.-E. Jin, S. Kim, and S.-W. Lee, *ACS Nano* **11**, 3632 (2017).
- [18] Z. Dogic and S. Fraden, *Philos. Trans. R. Soc. A* **359**, 997 (2001).
- [19] A. Kuijk, D. V. Byelov, A. V. Petukhov, A. van Blaaderen, and A. Imhof, *Faraday Discuss.* **159**, 181 (2012).
- [20] E. Grelet, *Phys. Rev. X* **4**, 021053 (2014).
- [21] Z. Zhang and E. Grelet, *Soft Matter* **9**, 1015 (2013).
- [22] S. Liu, C. Zheng, Z. Ye, B. Blanc, X. Zhi, L. Shi, and Z. Zhang, *Macromolecules* **51**, 8013

- (2018).
- [23] E. Barry and Z. Dogic, Proc. Natl. Acad. Sci. USA **107**, 10348 (2010).
- [24] A. de la Cotte, C. Wu, M. Trevisan, A. Repula, and E. Grelet, ACS Nano **11**, 10616 (2017).
- [25] A. Repula and E. Grelet, Phys. Rev. Lett. **121**, 097801 (2018).
- [26] See Supplemental Material at <http://link.aps.org/> which includes Refs [37, 38], for the details of the virus tip functionalization, its characterization by UV-visible spectrophotometry, and the SAXS data.
- [27] B. de Braaf, M. Oshima Menegon, S. Paquay, and P. van der Schoot, J. Chem. Phys. **147**, 244901 (2017).
- [28] H. N. W. Lekkerkerker and R. Tuinier, *Colloids and the Depletion Interaction*, Vol. 833 (Springer, Dordrecht, Netherlands, 2011).
- [29] Z. Dogic, K. R. Purdy, E. Grelet, M. Adams, and S. Fraden, Phys. Rev. E **69**, 051702 (2004).
- [30] H. N. W. Lekkerkerker and G. J. Vroege, Phil. Trans. R. Soc. Lond. A **344**, 419 (1993).
- [31] S. Dussi, M. Chiappini, and M. Dijkstra, Molecular Physics **116**, 2792 (2018).
- [32] E. Grelet and R. Rana, Soft Matter **12**, 4621 (2016).
- [33] E. Grelet, Phys. Rev. Lett. **100**, 168301 (2008).
- [34] L. Alvarez, M. P. Lettinga, and E. Grelet, Phys. Rev. Lett. **118**, 178002 (2017).
- [35] P. Bolhuis and D. Frenkel, J. Chem. Phys. **106**, 666 (1997).
- [36] P. van der Schoot, J. Phys. II France **6**, 1557 (1996).
- [37] A. Kremser and I. Rasched, Biochemistry **33**, 13954 (1994).
- [38] S. A. Berkowitz and L. A. Day, J. Mol. Biol. **102**, 531 (1976).

Supplemental Material:
**Directing liquid crystalline self-organization of rod-like particles
through tunable attractive single tips**

Andrii Repula,¹ Mariana Oshima Menegon,² Cheng

Wu,¹ Paul van der Schoot,^{2,3} and Eric Grelet*

*Centre de Recherche Paul-Pascal,
CNRS & Université de Bordeaux,
115 Avenue Schweitzer,
F-33600 Pessac, France*

² *Department of Applied Physics,
Eindhoven University of Technology,
PO Box 513, 5600 MB Eindhoven,
The Netherlands*

³ *Institute for Theoretical Physics,
Utrecht University, Princetonplein 5,
3584 CC Utrecht, The Netherlands*

(Dated: March 13, 2019)

*eric.grelet@crpp.cnrs.fr

I. AVERAGE NUMBER OF FLUORESCENT DYES PER VIRUS

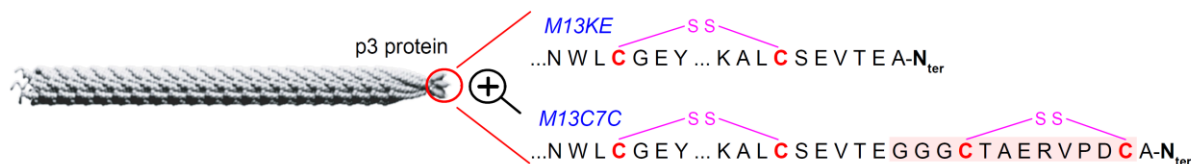


FIG. S1: Schematic representation of the amino acid sequence corresponding to the N-terminal part of the P3 protein exposed to the solvent and therefore accessible for chemical functionalization. M13KE virus possesses two cysteine groups at position 7 and 36 forming a disulfide bridge [37], while the genetically modified M13C7C virus has an additional fused polypeptidic sequence (highlighted in red) with two other cysteine residues also linked via a disulfide bond.

As systems of rod-like particles, we used two different mutants of filamentous bacteriophages, called M13KE and M13C7C, which only differ by the structure of their five tip proteins P3 located at the proximal end of the virus. M13KE possesses the wild-type P3 protein which has four disulfide bridges (otherwise absent from the other coat proteins of the virus) [37]. Among these disulfide bridges, mostly the last one is assumed to be sterically accessible for chemical bioconjugation (Fig. S1). In order to increase the number of cysteine groups available for functionalization, M13C7C was also employed, and it displays two other cysteine residues forming a disulfide bridge thanks to a fused peptide sequence on each of its five P3 proteins, as shown in Fig. S1.

After a reduction step of the disulfide bridges available on the P3 proteins, the resulting thiols have been chemically conjugated with different molar excess of maleimide activated fluorescent molecules (Dylight 550 and 594 Maleimide, ThermoFisher), following recently reported protocols [24-25]. In order to characterize the degree of labeling of the single-tip functionalized viruses, the mean number of grafted dyes per viral rod n_{dyes} has been determined by optical absorbance. The UV-visible spectra of four independent dilutions prepared from the different stock suspensions of tip-labeled viruses were recorded using a Lambda 950 (PerkinElmer) spectrophotometer (Fig. S2A), from which, after subtracting the background, n_{dyes} has been deduced as indicated in Fig. S2B.

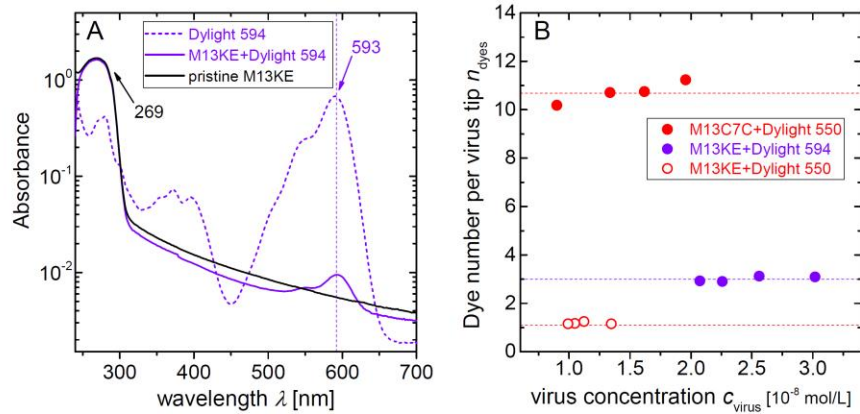


FIG. S2: **(A)** Absorbance of aqueous suspensions of pure dyes (Dylight 594), pristine M13KE viruses, and tip-functionalized ones with Dylight 594 fluorescent molecules measured with an optical path of 10 mm. The concentration of pristine and tip-labeled virus suspensions is 0.43 mg/mL (2.3×10^{-8} mol/L) and the dye concentration is 9×10^{-3} mg/mL (8.5×10^{-6} mol/L) **(B)** Mean number of dyes per virus tip, n_{dyes} , obtained from absorbance spectra and using the molar extinction coefficients provided by the dye supplier and the virus extinction coefficient given in [38].

II. SAXS EXPERIMENTS

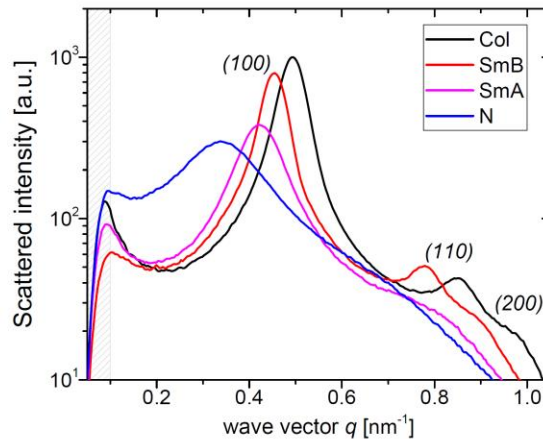


FIG. S3: X-ray scattering spectra of patchy virus suspensions ($n_{\text{dyes}} = 3$) self-organized into the different liquid crystalline phases reported in Fig. 2. The virus concentration of the nematic, smectic-A, smectic-B and columnar phases is 70, 109, 125 and 148 mg/mL, respectively. The gray dashed area indicates the unphysical region of the spectra near the beam stop.

Investigations by Small angle X-ray scattering (SAXS) have provided the signature of both the smectic-B phase and the columnar mesophase, with the presence of (110) Bragg reflections (Fig. S3) characteristic of a hexagonal positional order in the direction normal to the long rod axis. Such high order Bragg reflections lack in the Smectic-A and nematic phases, which both exhibit liquid-like order as shown by their broad (100) reflection (Fig. S3). SAXS experiments were performed using a NanoStar-Bruker AXS setup, working at a wavelength of 1.54 Å (Cu K α emission) and with a sample-to-detector distance of 1.06 m.

Chapter 2

Elementary edge and screw dislocations visualized at the lattice periodicity level in smectic phase of colloidal rods

The results reported in this Chapter have been published in *Physical Review Letters* in 2018. In this study, thanks to the tip-labeling of colloidal rods, we are able to visualize the lamellar liquid crystalline structure of viral suspensions including linear topological defects with improved resolution and contrast. Highly resolved optical images of the edge and screw dislocations are obtained in the smectic phase at the lattice periodicity level. The detailed structure of defect cores is shown, as well displacement field around an edge dislocation is established experimentally and compared to the theoretical predictions [30]. Single particle tracking experiments evidence “melted” rod organization within the screw dislocation cores.

Elementary edge and screw dislocations visualized at the lattice periodicity level in smectic phase of colloidal rods

Andrii Repula¹ and Eric Grelet^{1,*}

¹*Centre de Recherche Paul-Pascal, CNRS & Université de Bordeaux,
115 Avenue Schweitzer, F-33600 Pessac, France*

(Dated: March 18, 2019)

Abstract

Compelling justification: Topological defects such as dislocations play a major role in science, from condensed matter and geophysics to cosmology. Line defects in periodically ordered structures, called dislocations, mediate phase transitions and determine many distinctive features of materials, from crystal growth to mechanical properties. However, despite many theoretical predictions, the detailed structure of dislocations remains largely unexplored. By using a model system of tip-labeled colloidal rod-shaped particles enabling improved resolution and contrast by optical microscopy, *in situ* visualization of dislocations has been performed at the lattice periodicity level in a self-organized layered phase. The local morphology of dislocations has been quantitatively determined, evidencing experimentally a “melted” defect core.

Abstract: We report on the identification and quantitative characterization of elementary edge and screw dislocations in a colloidal smectic phase of tip-labeled rods. Thanks to the micrometer layer spacing, direct visualization of dislocations has been performed at the *smectic periodicity scale* by optical fluorescence microscopy. As a result, the displacement field around an edge dislocation has been experimentally established and compared with the profile predicted by elastic theory. Elementary screw dislocations have been also evidenced, for which the core size as well as the *in situ* handedness have been determined. Self-diffusion experiments performed at the individual particle level reveal for the first time nematic-like or “melted” ordering of the defect core.

* grelet@crpp-bordeaux.cnrs.fr

Topological defects are ubiquitous in all ordered systems, and are generated either extrinsically as in plastic deformation, or intrinsically in frustrated materials such as liquid crystalline blue phases [1–4]. Recently, they have been widely used to manipulate micro- and nanoparticles in different mesophases [5–8]. Among topological singularities, dislocations are linear defects with broken translational symmetry, and they determine many properties of regular solids [9, 10], including important mechanical ones in metals [11]. In systems with reduced dimensionality, such as layered phases usually found in soft condensed matter, dislocations exhibit substantial differences compared with their 3D counterparts [4, 9, 12, 13]. Despite their major role in liquid crystals [14–17] and in recently evidenced colloidal self-assembly where dislocations have been shown to mediate chirality transfer from constituent particles to helical superstructures [18], quantitative experimental characterizations of the dislocation displacement field as well as the core structure of elementary dislocations are scarce to date [4]. Such investigations rely on the observation of dislocations at length scales corresponding to the lamellar periodicity, which is of a few nanometers for most thermotropic, amphiphilic and block copolymer based liquid crystals [12, 19, 20]. This therefore usually requires electron microscopy techniques to gain access to nanometer resolved images, combined with a control of the sample alignment [21, 22]. If such difficulties have been partially bypassed by studying by optical microscopy some cholesteric mesophase whose fingerprint texture is reminiscent of a lamellar ordering [23–25], the detailed structure of elementary dislocations in real smectics is not yet fully achieved [17, 22, 26]. Specifically, the local order within the dislocation core is expected to be “melted” into a higher-symmetry phase; however, the nature of this order, either liquid-like or nematic-like, did not receive yet a full experimental confirmation. In this work, we have successfully produced tip functionalized rod-like particles, namely fd viruses fluorescently labeled at one end, whose monodisperse micrometer length results in the formation of colloidal smectic phase at high enough volume fractions. Taking advantage of its micrometer periodicity which enables its study by optical microscopy, the tip-labeled virus based colloidal smectic phase with planar alignment is found to exhibit elementary dislocations, namely edge and screw ones, as schematically represented in Fig. 1.

Experimentally, we used M13KE filamentous viruses, as system of rod-like particles. Each of the five P3 proteins localized at the virus proximal end displays pairs of cysteine residues (otherwise absent from the other coat proteins of the virus), forming disulfide bridges. After

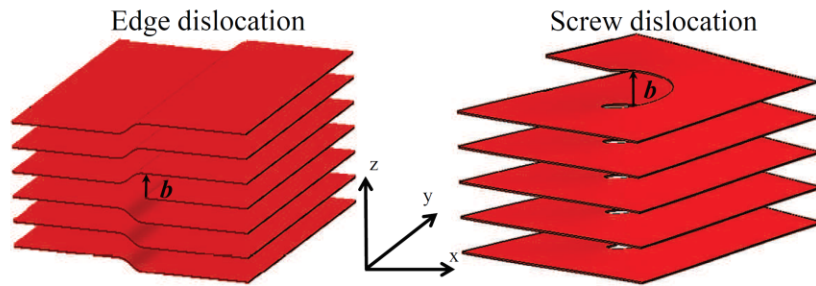


FIG. 1. Schematic representations of an edge and a screw dislocations in a lamellar system. The Burgers vector b is perpendicular to the dislocation line along y for an edge dislocation and it is parallel to the dislocation line along z in a screw dislocation.

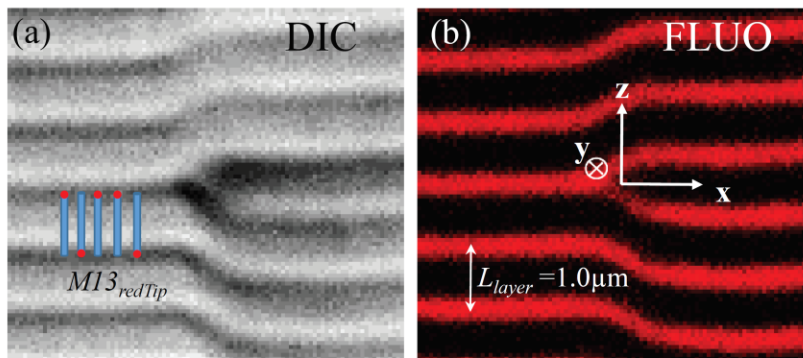


FIG. 2. Imaging of smectic layers and an edge dislocation in suspensions of tip-functionalized colloidal rods ($M13_{redTip}$, schematically represented by blue dashes with red dots) observed respectively by (a) differential interference contrast (DIC) and (b) fluorescence optical microscopy. The length scale is provided by the micrometer layer spacing, L_{layer} . The origin for profile measurement is located at the dislocation core. In the observation plane, the x and z axes are parallel and perpendicular to the layers, while the focal depth is along the y axis.

reduction by Tris(2-carboxyethyl)phosphine hydrochloride (TCEP, Thermo Scientific), the resulting thiol groups are available for conjugation with maleimide activated compounds. We chose to specifically label these thiol groups present at the virus tip with red dyes (DyLight 550 Maleimide, ThermoFisher) according to a protocol reported elsewhere [27]. This results in $1.0 \mu m$ long tip-labeled viral particles, called $M13_{redTip}$, whose phase behavior in aqueous suspension presents liquid crystalline ordering, as the lamellar organization including smectic-A and smectic-B phases in the dense regime [28, 29]. Part of these tip-functionalized

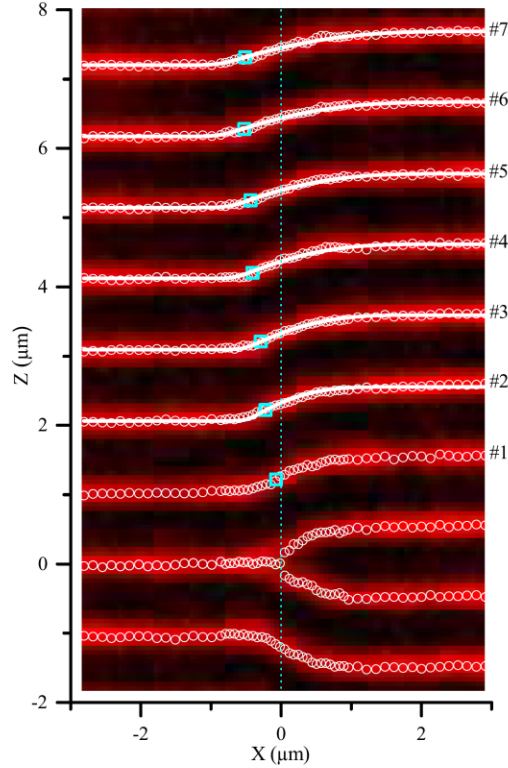


FIG. 3. Edge dislocation observed by fluorescence microscopy and the corresponding displacement field (white open circles) of the adjacent smectic layers around the defect core. The white solid lines represent the global fitting of the dislocation profile according to the nonlinear elastic theory (Eq. 3) from which the elastic length λ (Eq. 2) can be deduced. The inflection points are marked by blue open squares, and are all shifted toward the same direction ($x < 0$) as predicted by the theory (Eq. 3).

viruses were body-labeled with green fluorescent dyes (Alexa488-NHS ester activated, Molecular Probes) [27] and added in tracer amounts to a few $M13_{redTip}$ samples for single particle tracking experiments. A set of samples with concentrations in the smectic-A range were prepared (in 17mM BisTris-HCl-NaCl buffer, pH 7, with 3 mM NaN_3 as bactericide, for a total ionic strength of 20 mM) between cover slip and glass slides, and observations were performed using an optical microscope (IX-71 Olympus), equipped with a high-numerical aperture (NA) oil objective (100X PlanApo NA 1.40), a piezo device for objective vertical positioning (P-721 PIFOC Piezo Flexure Objective Scanner, PI), a fluorescence excitation light source (X-cite series 120 Q) and an ultra-fast electron-multiplying camera (NEO sC-

MOS Andor) with a pixel size of $6.5 \mu\text{m}$. An equilibrium time of typically a few days was applied in order to get homogeneous and uniform smectic-A samples. This could result sometimes in a partial drying of the samples, leading possibly to some smectic-B ordering.

The resulting smectic phase formed by the tip-labeled rod-like viruses, is observed both by differential interference contrast and fluorescence microscopy, as shown in Figure 2. Both contrast modes reveal the lamellar periodicity of the smectic organization, with improved resolution and contrast in case of fluorescence microscopy. As the tips of our colloidal rods have been labeled with red dyes, the smectic layer positions as well as the layer spacing, L_{layer} , can be experimentally determined with a good level of precision. This allows for the quantitative analysis of the displacement field around an elementary edge dislocation, as reported in Fig. 3. The general expression of the nonlinear elastic free energy density of a smectic phase is, by accounting for the higher order derivatives in the displacement field, $u(x, z)$ [3]:

$$f = \frac{B}{2} \left(\frac{\partial u}{\partial z} - \frac{1}{2} \left(\frac{\partial u}{\partial x} \right)^2 \right)^2 + \frac{K_1}{2} \left(\frac{\partial^2 u}{\partial x^2} \right)^2 \quad (1)$$

with B the compressibility modulus and K_1 the bending elastic constant, analogous to the nematic splay elastic constant. The elastic length λ can then be defined as:

$$\lambda = \sqrt{\frac{K_1}{B}} \quad (2)$$

providing the intrinsic length scale over which an imposed distortion relaxes in a lamellar system. Using Eq. 1, Brener and Marchenko found the analytical edge dislocation profile [30]:

$$u(x, z) = 2\lambda \ln \left[1 + \frac{\exp(b/4\lambda) - 1}{2} \left(1 + \text{erf} \left(\frac{x}{2\sqrt{\lambda z}} \right) \right) \right] \quad (3)$$

where $\text{erf}(\dots)$ is the error function. In the limit of small Burgers vector $b \ll \lambda$, Eq. 3 reduces to the classical result of the linear elastic theory [9, 31]:

$$u(x, z) = \frac{b}{4} \left[1 + \text{erf} \left(\frac{x}{2\sqrt{\lambda z}} \right) \right] \quad (4)$$

Figure 3 shows the measured displacement field of the smectic layers around a dislocation core. Note that it is difficult experimentally to have fully isolated edge dislocations: most are disturbed by elastic distortion stemming either from the presence of other defects and grain boundaries, or from heterogeneous anchoring at the cell walls, which can result in a lack of mirror symmetry of the defect. As expected for an edge dislocation of Burgers vector

$b/L_{layer} = 1$, the total displacement of a given layer is $b/2$ regardless the layer distance from the defect core. This has been experimentally checked within an accuracy greater than 95% for the 6 considered layers (Fig. 3), proving *a posteriori* that the chosen edge dislocation is nearly isolated. This is also confirmed from the quantitative analysis of the dislocation profile, performed according to Eq. 3. The smectic layers of interest have been globally fitted with a single value of the elastic length λ to account for the overall displacement field. With a resulting value of $\lambda = 0.02 \pm 0.01 \mu m$, a very good agreement with the nonlinear elastic theory is found far enough from the dislocation core (from layers #3 to #7, Fig. 3). The first layers, which are too close to the defect core, have been either disregarded from the quantitative analysis (layer #1), or are approximatively fitted by the model (layer #2). As $\lambda \ll b$, only the nonlinear elastic theory is expected to apply, with some intrinsic features clearly evidenced in our experimental data. This includes a shift of the inflection points towards the smectic region with the missing layer ($x < 0$, Fig. 3) and an asymmetry of the dislocation profile with a sharp rise at $x < 0$ and a smooth saturation at $x > 0$ [23, 30]. It is worth mentioning that if the nonlinear elastic theory (Eq. 3) is able to account for the experimental displacement field, the quantitative comparison remains quite sensitive to any extrinsic disturbance of the defect profile.

From the determination of the elastic length λ , the compressibility modulus B can be calculated knowing the bending modulus K_1 (Eq. 2). In fluid-like membranes composed of one-rod length thick monolayer of aligned viruses, the bending modulus has been found to be $\kappa_c \simeq 150 k_B T$ [32]. To extend this value found for a single membrane to a bulk smectic phase composed of similar colloidal viral rods, we have to renormalize κ_c by the smectic layer spacing L_{layer} to give an estimation of the 3D bending modulus $K_1 = \kappa_c / L_{layer} \approx 150 k_B T / \mu m$. It is worth pointing out that this value is in good agreement with the value obtained from the one-Frank constant approximation $K_1 \approx K_2 = 0.5 pN = 100 k_B T / \mu m$, where K_2 is the twist elastic constant measured by unwinding the cholesteric phase of virus suspensions under magnetic field [33]. Knowing K_1 and λ , we can therefore estimate, according to Eq. 2, the smectic compressibility modulus $B \simeq 4 \times 10^5 k_B T / \mu m^3$ for a smectic phase of colloidal rods. This value can be compared with the typical one found in thermotropic smectics [34], $B_{thermotropic} \sim 10^8 \text{ dyn/cm}^2 \simeq 2 \times 10^9 k_B T / \mu m^3 = 2 k_B T / nm^3$. This means that if the absolute value of the compressibility modulus is higher by a few orders of magnitude in thermotropic liquid crystals, the same value rescaled by the molecular length (nanometers in

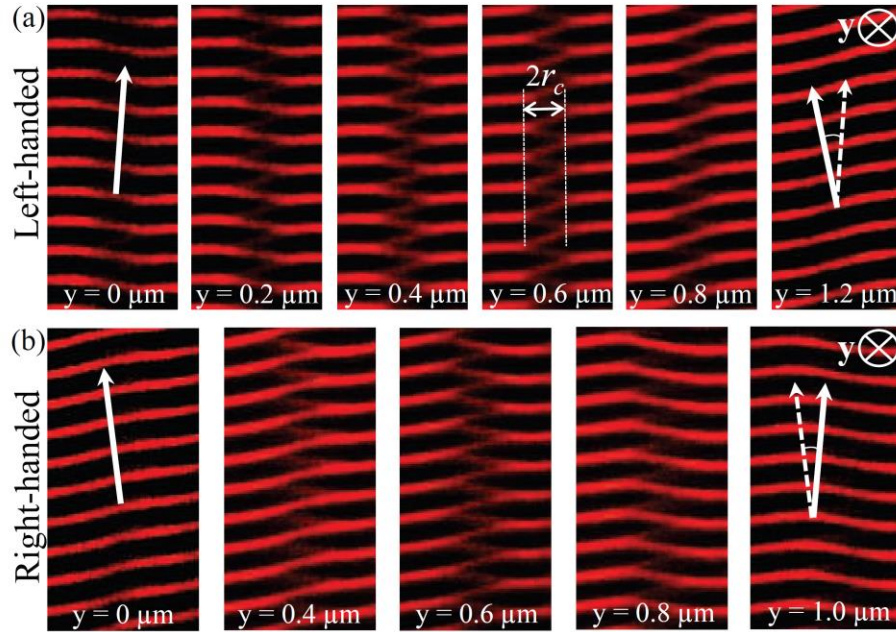


FIG. 4. Screw dislocations with opposite handedness observed by fluorescence microscopy in smectic phase of tip-labeled viruses. The handedness has been determined by capturing images at different focal depths y , resulting in (a) left- and (b) right-handed screw dislocations, as indicated by the rotation of the normal to the smectic layers shown by the white arrows. The length scale is provided by the $1 \mu m$ long smectic layer spacing.

size in thermotropics compared with the micrometer length for viral colloidal rods) indicates a softer rescaled layer compressibility in molecular systems.

In our smectic samples of tip-labeled-viruses, only elementary dislocations have been observed, with a Burgers vector magnitude $b = 1 \times L_{layer} = 1 \mu m$ (Fig. 1) whatever the dislocation type (either edge type or screw type). Examples of screw dislocations are shown in Fig. 4, where, remarkably, their core extension can be clearly distinguished. This allows for the *in situ* handedness determination by varying the optical microscope focus through the sample thickness, y , resulting in the presence of both left-handed and right-handed screw dislocations (Fig. 4), as expected in an achiral smectic-A mesophase. Here, we benefit from the micrometer length scale of our experimental system, enabling structural investigations that are otherwise very tricky to achieve using usual molecular nanometric liquid crystals [22]. Specifically, the screw dislocation core size $2r_c$ can be measured, as indicated in Fig. 4.

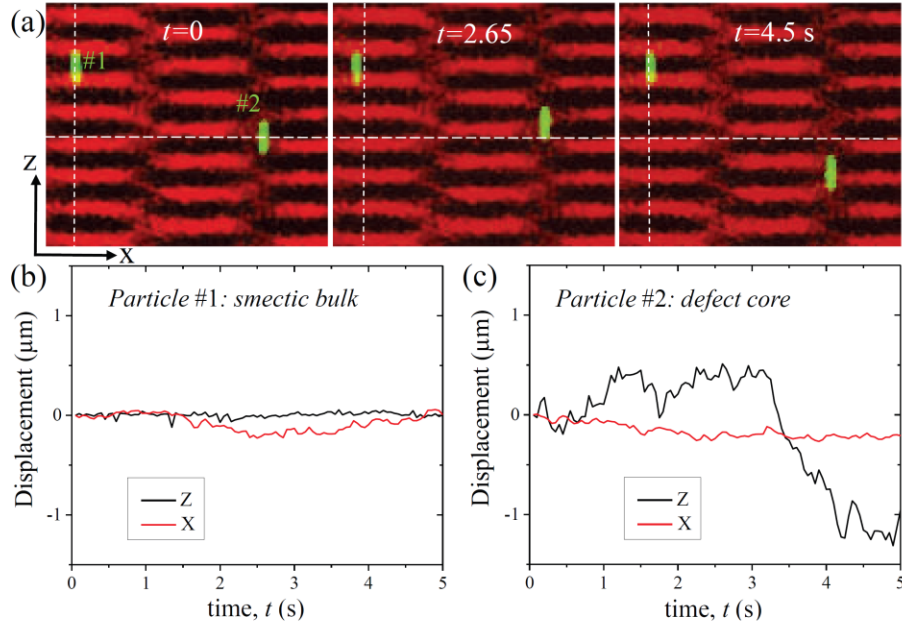


FIG. 5. (a) Overlays at different times of fluorescence microscopy images showing red smectic layers from $M13_{redTip}$ particles, in which tracer amounts of $M13_{redTip}$ particles body-labeled with green fluorescent dyes have been added, enabling single particle tracking experiments. The vertical dotted and horizontal dashed lines are visual guides to emphasize the displacements of green viral particles #1 and #2, respectively. The length scale is provided by the $1 \mu\text{m}$ long smectic layer spacing. (b) Example of a trajectory within the smectic-A bulk where the particle mainly displays lateral motion within the layers. (c) Trajectory of a viral rod-like particle within the defect core evidencing its rapid parallel (i.e. along the z axis) diffusion, characteristic of nematic-like behavior.

The distribution of core radii has been determined and is shown in the Supplemental Material [35]: a mean value of $2r_c = 0.98 \mu\text{m} \simeq b$ is found. This value of the screw dislocation core size is in good agreement with the one determined by Zhang *et al.* [26], but is larger than the theoretical prediction $2r_c \approx b/\pi$ performed by Pleiner [36, 37]. Theoretical models should therefore be developed for a more detailed description of the microstructure of the screw dislocation core [38] to account for the experimental observations. The introduction of tracer amounts of additionally body-labeled viruses with green fluorescent dyes in the smectic samples provides further information about the dislocation core. Figure 5 reveals the dynamics at the single particle level, and a main difference distinguishes the self-diffusion within the dislocation core, where a body-labeled rod has been trapped, from the smectic

bulk: contrary to viral particles in the smectic bulk which diffuse slightly within the layers with rare hopping type events [39] (See the Supplemental Material [35]), the diffusion of the particles within the defect core is strongly enhanced, with a large displacement, for a given observation time, along the director (or, equivalently, along the normal to the smectic layers indicated by the z axis). This dynamics with a motion mainly along the long rod axis and without significant rotational diffusion, is characteristic of nematic-like behavior [39], and represents to the best of our knowledge, the first demonstration of the nematic ordering associated with the higher-symmetry phase forming the dislocation core in smectic defects. This nematic order is in qualitative agreement with phenomenological Landau-de Gennes type modeling of screw dislocation core structures [36, 40], and our experimental results therefore rule out dislocation models based on either isotropic liquid core or strongly distorted smectic layers at the vicinity of the defect core [36, 37, 40, 41]. Despite the larger number of screw dislocations observed in our samples compared to edge ones, which is consistent with their respective free energy [3, 9], it turns out that only a very few labeled particles have been seen in the defect core (See the Supplemental Material [35]), making further quantitative analysis of the dynamics of this system difficult.

To conclude, we have identified and quantitatively characterized the microscopic structure of edge and screw dislocations in a smectic phase of functionalized colloidal rod-like particles. Thanks to a regioselective labeling of the filamentous virus tips by fluorescent dyes, high resolution and contrast imaging of the topological defects has been achieved by fluorescence microscopy, revealing the displacement field around elementary edge dislocation, as well as some unprecedented detailed information of the screw dislocation core, such as its size, helical handedness and local structure with a nematic-like ordering. A perspective of our work is the use of topological defects formed by *colloidal liquid crystals* to organize nano- and microparticle assemblies.

ACKNOWLEDGMENTS

This project has received funding from the European Union Horizon 2020 research and innovation programme under the Marie Skłodowska-Curie Grant Agreement No. 641839. We thank A. de la Cotte for preliminary experiments, C. Wu for help in sample preparation, P. Merzeau for drawing the schemes, and F. Nallet for discussions.

Author contributions: A.R. prepared the samples and performed experiments, E.G. analyzed the data and wrote the paper.

-
- [1] P. M. Chaikin and T. C. Lubensky, *Principles of Condensed Matter Physics* (Cambridge Univ Press, Cambridge, 1995).
 - [2] M. Kleman, O. D. Lavrentovich, and Y. A. Nastishin, in *Dislocations in Solids*, edited by F. R. N. Nabarro and J. P. Hirth (Elsevier, Amsterdam Vol. 12, p. 147, 2004).
 - [3] M. Kleman and O. D. Lavrentovich, *Soft Matter Physics: An Introduction* (Springer-Verlag, New York, 2002).
 - [4] P. Oswald and P. Pieranski, *Smectic and Columnar Liquid Crystals: Concepts and Physical Properties Illustrated by Experiments* (Taylor and Francis/CRC Press, London, 2005).
 - [5] Y. Iwashita and H. Tanaka, *Phys. Rev. Lett.* **90**, 045501 (2003).
 - [6] U. Tkalec, M. Ravnik, S. Čopar, S. Žumer, and I. Muševič, *Science* **333**, 62 (2011).
 - [7] D. Coursault, J. Grand, B. Zappone, H. Ayeb, G. Lévi, N. Félidj, and E. Lacaze, *Adv. Mater.* **24**, 1461 (2012).
 - [8] X. Wang, D. S. Miller, E. Bukusoglu, J. J. de Pablo, and N. L. Abbott, *Nature Mater.* **15**, 106 (2016).
 - [9] M. Kleman, *Points, Lines and Walls* (Wiley, New York, 1983).
 - [10] D. Hänschke, A. Danilewsky, L. Helfen, E. Hamann, and T. Baumbach, *Phys. Rev. Lett.* **119**, 215504 (2017).
 - [11] J. Friedel, *Dislocations* (Pergamon Press, Oxford, 1964).
 - [12] R. Holyst and P. Oswald, *Int. J. Mod. Phys. B* **9**, 1515 (1995).
 - [13] P. Pieranski, *C. R. Physique* **17**, 242 (2016).
 - [14] R. B. Meyer, B. Stebler, and S. T. Lagerwall, *Phys. Rev. Lett.* **41**, 1393 (1978).
 - [15] R. D. Kamien and T. C. Lubensky, *J. Phys II France* **7**, 157 (1997).
 - [16] R. P. Trivedi, I. I. Klevets, B. Senyuk, T. Lee, and I. I. Smalyukh, *Proc. Natl. Acad. Sci. USA* **109**, 4744 (2012).
 - [17] H. Aharoni, T. Machon, and R. D. Kamien, *Phys. Rev. Lett.* **118**, 257801 (2017).
 - [18] B. Sung, A. de la Cotte, and E. Grelet, *Nat. Commun.* **9**, 1405 (2018).
 - [19] W. K. Chan and W. W. Webb, *J. Phys. Lett. (Paris)* **42**, 1007 (1981).

- [20] M. Maaloum, D. Ausserré, D. Chatenay, G. Coulon, and Y. Gallot, *Phys. Rev. Lett.* **68**, 1575 (1992).
- [21] J. A. N. Zasadzinski, *J. Phys. France* **51**, 747 (1990).
- [22] C. Zhang, A. M. Grubb, A. J. Seed, P. Sampson, A. Jakli, and O. D. Lavrentovich, *Phys. Rev. Lett.* **115**, 087801 (2015).
- [23] T. Ishikawa and O. D. Lavrentovich, *Phys. Rev. E* **60**, R5037 (1999).
- [24] I. I. Smalyukh and O. D. Lavrentovich, *Phys. Rev. E* **66**, 051703 (2002).
- [25] D. Engström, R. P. Trivedi, M. Persson, M. Goksör, K. A. Bertness, and I. I. Smalyukh, *Soft Matter* **7**, 6304 (2011).
- [26] C. Zhang, B. K. Sadashiva, O. D. Lavrentovich, and A. Jákli, *Liq. Cryst.* **40**, 1636 (2013).
- [27] A. de la Cotte, C. Wu, M. Trevisan, A. Repula, and E. Grelet, *ACS Nano* **11**, 10616 (2017).
- [28] Z. Dogic and S. Fraden, *Curr. Opin. Colloid Interface Sci.* **11**, 47 (2006).
- [29] E. Grelet, *Phys. Rev. X* **4**, 021053 (2014).
- [30] E. A. Brener and V. I. Marchenko, *Phys. Rev. E* **59**, R4752 (1999).
- [31] P. G. de Gennes, *C. R. Hebd. Séances Acad. Sci.* **275B**, 939 (1972).
- [32] E. Barry and Z. Dogic, *Proc. Natl. Acad. Sci. USA* **107**, 10348 (2010).
- [33] Z. Dogic and S. Fraden, *Langmuir* **16**, 7820 (2000).
- [34] S. Shibahara, J. Yamamoto, Y. Takanishi, K. Ishikawa, H. Takezoe, and H. Tanaka, *Phys. Rev. Lett.* **85**, 1670 (2000).
- [35] See Supplemental Material at <http://link.aps.org/> for the width distribution of screw dislocation cores, a movie displaying the self-diffusion of tip-labeled rod-like particles within the defect core and the smectic bulk, with an example of rare hopping-type events.
- [36] H. Pleiner, *Liq. Cryst.* **1**, 197 (1986).
- [37] H. Pleiner, *Liq. Cryst.* **3**, 249 (1988).
- [38] E. A. Matsumoto, R. D. Kamien, and C. D. Santangelo, *Interface Focus* **2**, 617 (2012).
- [39] L. Alvarez, M. P. Lettinga, and E. Grelet, *Phys. Rev. Lett.* **118**, 178002 (2017).
- [40] S. Kralj and T. J. Sluckin, *Phys. Rev. E* **48**, R3244 (1993).
- [41] S. Kralj and T. J. Sluckin, *Liq. Cryst.* **18**, 887 (1995).

Supplemental Material:
**Elementary edge and screw dislocations visualized at the lattice
periodicity level in smectic phase of colloidal rods**

Andrii Repula¹ and Eric Grelet*
*Centre de Recherche Paul-Pascal,
CNRS & Université de Bordeaux,
115 Avenue Schweitzer,
F-33600 Pessac, France*

(Dated: July 18, 2018)

*grelet@crpp-bordeaux.cnrs.fr

I. SUPPLEMENTARY FIGURES

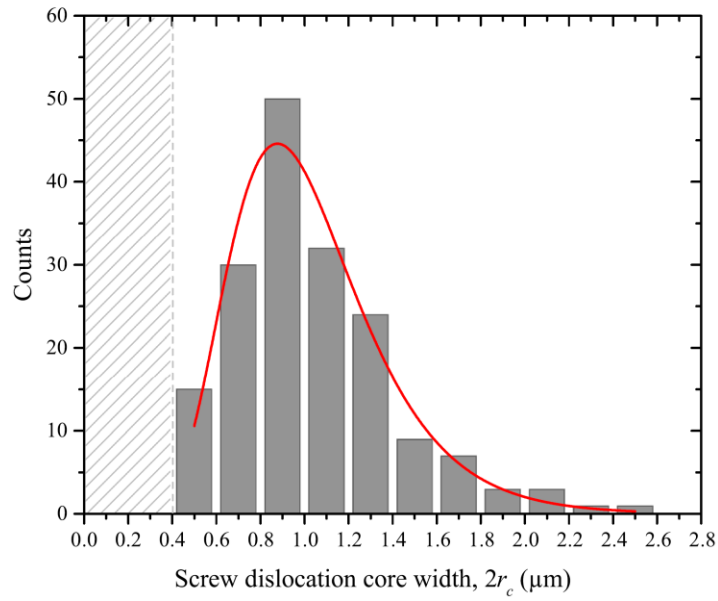


FIG. S1: Width distribution of the screw dislocation cores, as typically observed in Figure 4. The red solid line is a lognormal fit, from which the mean core width $2r_c = 0.98 \mu\text{m} \simeq b$ can be extracted. The gray vertical dashed line indicates the optical resolution, corresponding to about twice the $x - z$ microscope one, above which the dislocation core size can be measured.

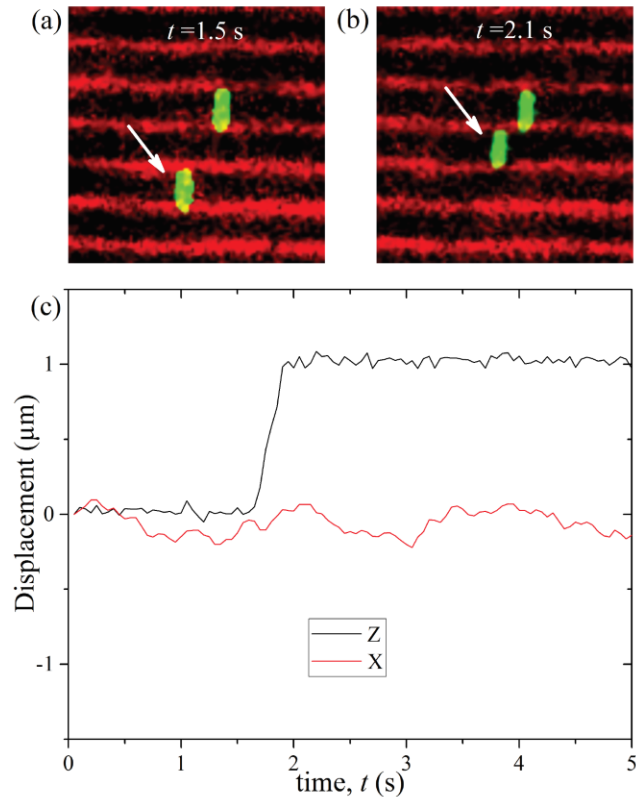


FIG. S2: Example of hopping-type event observed by fluorescence microscopy ((a) and (b)) in smectic-A phase of tip-labeled viral rods, and the corresponding trajectory (c). The white arrow indicates the jumping particle. It has to be emphasized that such events are rare in this system where most of the particles exhibit lateral (i.e. along the x axis) motion within the layers, as shown in Fig. 5(b). The length scale is provided by the 1 μm length of labeled viruses.

II. MOVIE

Real time dynamics of green labeled viral particles inserted in smectic phase of tip-functionalized viruses, from which Figure 5 has been extracted. Note the presence of many equidistant screw dislocations characteristic of twist grain boundary. The two yellow arrows indicate particles trapped in screw dislocation cores, which display enhanced self-diffusion compared to the other labeled particles within the smectic bulk.

Chapter 3

Effect of patchy interaction on dynamics of rod-like colloids

3.1 Introduction.....	90
3.2 Results and Discussion.....	91
3.2.1 Mean square displacements in different phases	91
3.2.1.1 Columnar and Smectic B phases.....	92
3.2.1.2 Smectic A phase.....	94
3.2.1.3 Nematic phase.....	99
3.2.1.4 Isotropic liquid phase.....	103
3.2.2 Self-diffusion coefficients of patchy and pristine rods	106
3.2.3 Orientational order parameter in patchy and pristine suspensions.....	108
3.3 Conclusions.....	109
3.4 References.....	110

3.1 Introduction

Dynamical properties of concentrated colloidal dispersions are of great importance in modern soft matter science. Structure of complex fluids cannot be fully understood without deep insight into transport processes occurring in media. Due to low Reynolds numbers, self-diffusion is the main transport process in colloidal dispersions defining their dynamical properties [18]. Dynamics in colloidal dispersions where constituting particles interact via hard-core repulsion has been fruitfully investigated experimentally in case of rod-like filamentous viruses [1]-[4], PMMA (polymethyl methacrylate) ellipsoids [29], and silica spheres [30]. Dynamical properties of some protein solutions have been also explained based on hard-core interaction between particles [5]-[7], [19]-[21]. However, despite increased attention to colloidal systems with directional attractive interaction or "patchiness", experimental investigations of their dynamical properties are presently lacking. Some studies based on neutron scattering have reported on the self-diffusion of nearly spherical proteins with weak patchy interaction and the comparison with the self-diffusion of their hard-core counterparts [8]. Nevertheless, a quantitative comparison of these two systems cannot be carried out due to difference of particle hydrodynamic radii ($R_h = 2.3$ nm and 9.6 nm for patchy and hard-core particles respectively) and their size polydispersity. Thus, our system of patchy colloidal rods is more appealing from this perspective, as the effect of local attraction on self-diffusion can be studied by direct comparison of two viral systems which only differ by presence of highly localized sticky inclusions on the particle tips in one of them, whereas other parameters characterizing size and shape of both particle types remain unchanged (see Chapter 1). Besides, the colloid motion can be visualized by fluorescence optical microscopy at the single particle level providing detailed understanding of the dynamical features of patchy dispersions.

Therefore in this Chapter, we have performed an investigation of the translational self-diffusion of tip-functionalized and pristine (purely repulsive) rod-like colloids covering a wide range of particle concentration: from isotropic liquid states up to highly concentrated regimes including different liquid crystalline phases.

3.2 Results and Discussion

In order to study the effect of local directional interaction on the dynamical properties of viral dispersions, we chose to work with filamentous virus mutants M13C7C and M13KE (see Chapter 0.4), and with hydrophobic fluorescent dye molecules Dylight 550 and Dylight 594 (ThermoFisher) which has been shown to act as patchy inclusions. As we already mentioned in Chapter 1, those two types of viruses only differ by the number of cysteine bonds at the viral proximal tips. Using this fact and varying the dye molar excess during chemical reactions for the tip functionalization, the number of dye molecules grafted on one of the viral ends can be controlled from $n_{dyes} = 1, 3$ to 10 dyes per particle tip. In Chapter 1, we have shown that number of grafted dyes defines the strength of local attraction between viral tips and thus affects the phase behavior of patchy dispersions. However, exposed hydrophobic moieties of unfolded p3 proteins which appeared after cysteine reduction and dye labeling can also contribute to the patchy effect on rod tips. Still, it is reasonable to assume that the amount and size of these exposed groups increases with the degree of labeling, as shown by our experiments in Chapter 1.

Self-diffusion was studied employing tracking of rod displacements by fluorescence optical microscopy adding a tracer amount of viruses with *full body labeling* (green dyes cover the whole viral surface) and *combined labeling* (red dyes on viral tip inducing patchiness, and green dyes cover the rest of the rod surface), into dispersions of pristine and patchy particles respectively (see section 0.4.3).

3.2.1 Mean square displacements in different phases

To characterize the differences in dynamical features between pristine and patchy viruses, for these two types of dispersions with respect to the main rod axis we quantified and compared parallel and perpendicular mean square displacements (MSD_{\parallel} and MSD_{\perp}), and then we determined the self-diffusion rates $D_{\parallel,\perp}$ and the *diffusion exponents* $\gamma_{\parallel,\perp}$ via the expression $MSD_{\parallel,\perp} = 2D_{\parallel,\perp}t^{\gamma_{\parallel,\perp}}$ (see Chapter 0.4.2). MSD calculations rely on the individual trajectories of body-labeled viruses obtained via fluorescence optical microscopy. By performing the observation of tip-functionalized rod motion in all phases of viral dispersions, we discriminated two populations of patchy viruses. The first population is the fraction of patchy particles which diffuse qualitatively similarly to pristine ones meaning that their translational displacement parallel to the main rod axis direction is much more pronounced than in perpendicular direction

in the nematic and smectic states [1]-[4], whereas they have no preferential direction of motion in isotropic phase [1]. The second population is the fraction of patchy viruses which are bound at one of their tips to the two-dimensional clusters (see Chapter 1, Fig. 3). Having such constraint they perform "anchored" self-diffusion i.e. local rotational self-diffusion with one rod end being immobile. To achieve an adequate comparison between dynamics in tip-functionalized and pristine colloidal dispersions, we calculated MSD only of patchy particles from the first population disregarding the second one, whose specific behavior will be discussed in section 3.2.3.

Local attraction between rods is expected to strongly affect the dynamical properties of particles in crowded conditions [23] resulting in subdiffusive behavior of viral dispersions characterized by diffusion exponent $\gamma < 1$ (see Chapter 0.4.2). Subdiffusive behavior with $\gamma < 1$ have been detected recently for the smectic phase of filamentous viruses [4], due to effect of crowding when approaching the crystalline phase, where voids are created in the adjacent smectic layers.

Below we reported the results on MSD of patchy rods and compared them to the MSD of pristine rods in order of decreasing particle concentration in dispersions.

3.2.1.1 Columnar and Smectic B phases

The most concentrated states which have been achieved experimentally in patchy and pristine rod dispersions are columnar and smectic B liquid crystalline phases. It has been shown recently by means of SAXS experiments on raw fd suspensions that both phases possess positional order in the directions perpendicular to the director [9]. Dynamical studies by fluorescence microscopy revealed the lack of significant viral self-diffusion except very rare half- and full-rod-length jumps in columnar phase (a particle jumps one time per around 12 hours) stemming from particle moving into defects and due to collective dynamics in which particles move in and between columns, respectively [4], [10]. Our experimental study has evidenced the existence of positional order in columnar and smectic B phases in dispersions of patchy viruses (see Chapter 1, Fig. S3). Self-diffusion experiments have not revealed any significant motion of tip-labeled viruses in these highly concentrated states. We have not detected any half- and full-rod-length jumps in our patchy dispersions within time observation

window of around 10 seconds, which was limited by the green dye photobleaching. The examples of single patchy particle trajectories in columnar and in layered B phases are shown in Fig. 3.1, indicating only signals which are less than microscope x-z resolution corresponding to about $0.2 \mu\text{m}$. Slightly higher signal magnitude in parallel direction can be caused by asymmetry of 2D Gaussian fit during particle detection [1].

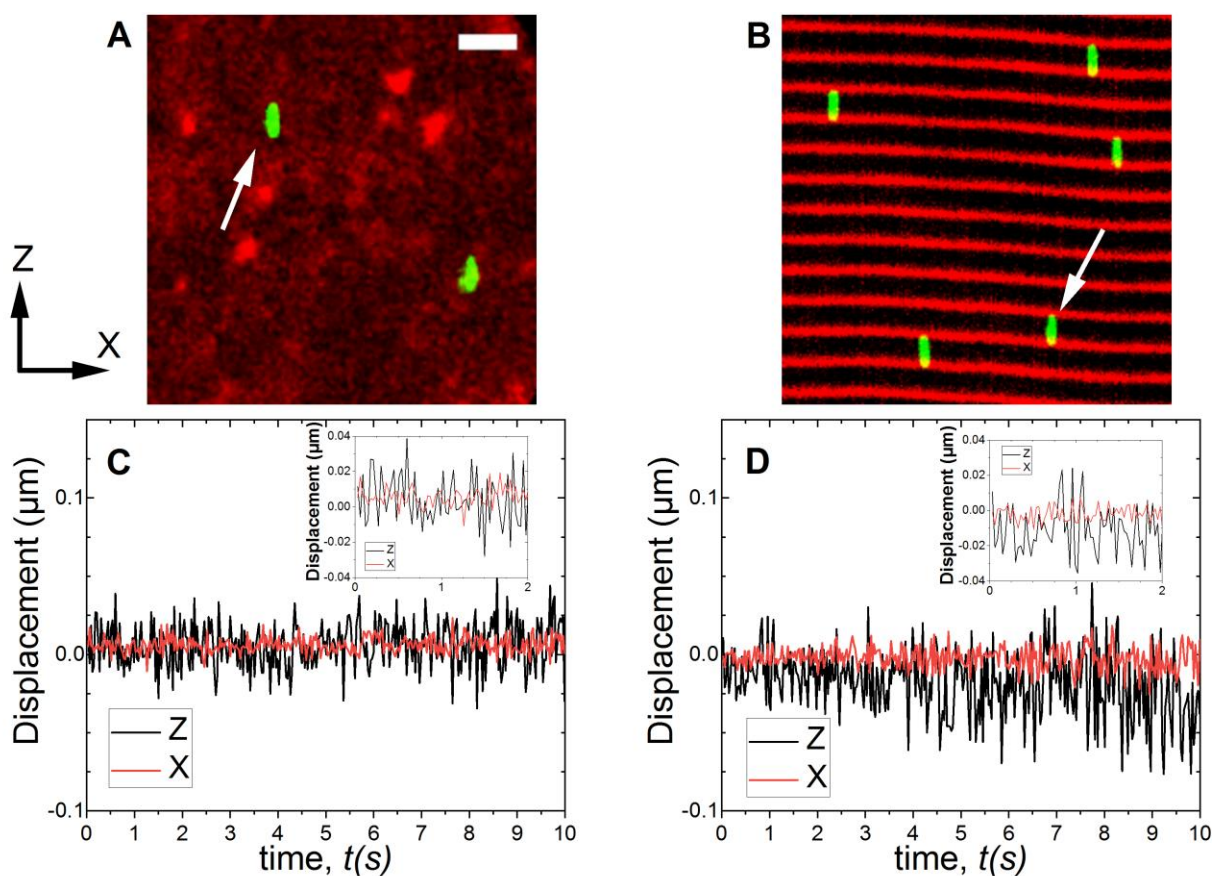


Fig. 3.1. Overlay of fluorescence microscopy images showing red signal coming from tip-functionalized viruses (3 dyes per tip) in (A) columnar ($c_{\text{virus}} = 151 \text{ mg/ml}$) and (B) layered smectic B ($c_{\text{virus}} = 124 \text{ mg/ml}$) phases. Tracer amount of particles with combined labeling (red dyes on the tip, green fluorescent dyes on the body) has been added to enable single rod tracking experiments. Scale bar: $2 \mu\text{m}$. Examples of trajectories in (C) columnar and (D) smectic B phases where particles do not show self-diffusion. Insets represent the signal magnitude in parallel and perpendicular directions. White arrows indicate the particles whose trajectories are plotted in (C) and (D).

MSD of both patchy and pristine dispersions in directions parallel and perpendicular to the main rod axis have been calculated relying on single particle trajectories and revealed no

time evolution confirming the lack of significant motion in columnar and smectic B phases. Each MSD curve (Fig. 3.2) has different positive offset coming from localization uncertainty during particle detections [11]. As there is no time evolution of MSD, we have not performed the numerical analysis to determine self-diffusion rates in the columnar and smectic B phases.

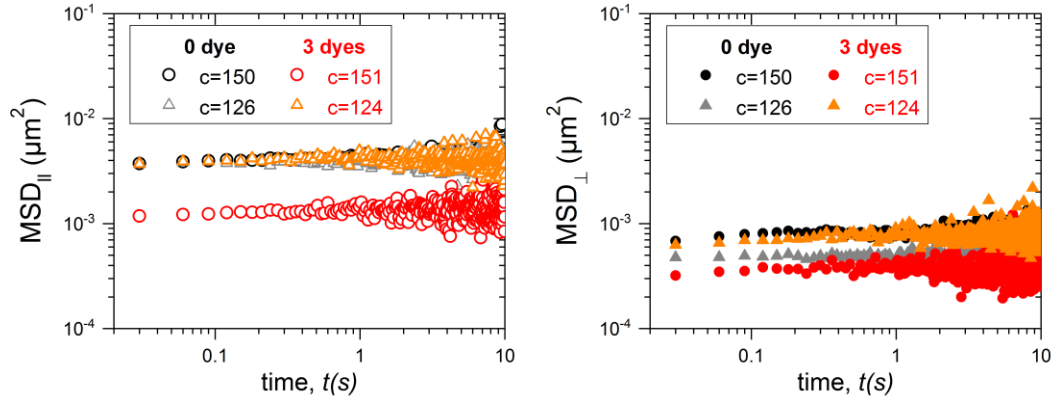


Fig. 3.2. Log-log representation of the parallel (left, open symbols) and perpendicular (right, solid symbols) mean square displacements (MSD) for the columnar and smectic B phases of pristine (0 dyes) and patchy (3 dyes) viral dispersions. The rod concentration in the columnar phase is 150 mg/ml (pristine particles) and 151mg/ml (patchy particles), and in the smectic B phase is 126 mg/ml (pristine) and 124 mg/ml (patchy).

3.2.1.2 Smectic A phase

Dilution of smectic B leads to one more lamellar phase which is smectic A. There is liquid-like order within the smectic layers. Due to decreasing concentration, patchy and pristine rods gain mobility in smectic A, thus tip-functionalized viruses can be discriminated in two populations according to their dynamical behavior. Dynamics of the first population of patchy rods is qualitatively similar to the one found for pristine rods: discontinuous hopping-like displacements between adjacent layers parallel to the viral rod axis and continuous motion perpendicular to it within layers [2]-[4]. We evidenced that the tip-functionalized particles from the first population usually belong to the cluster-free homogeneous smectic domain (Fig. 3.5). Residence time of sticky rods within one smectic layer is longer meaning that their jumps between layers take place much more rarely compared to raw particles. Examples of patchy rod trajectories with lateral (motion within the layer) and hopping-like self-diffusion are shown in Fig. 3.4. Due to local attraction between tips, rods prefer to stay close to each other performing displacements within the layers rather than jump abruptly to a neighbor layer. This behavior

results in higher smectic ordering potential of tip-functionalized particles measured in Chapter 1. It has values within the range $5 - 9k_B T$ for tip-labeled rods compared to $3 - 5k_B T$ for pristine ones (Fig. 3.3).

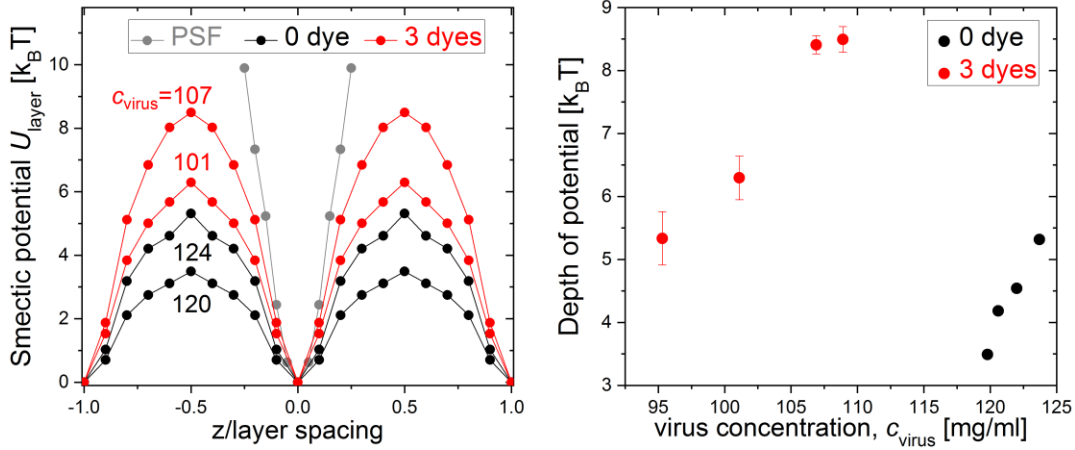


Fig. 3.3. **(Left)** Smectic ordering potentials calculated from experimental distribution of particles, as a function of the particle position, normalized by the smectic layer spacing, for different rod concentrations. In gray we indicate the experimentally measured potential of immobile particles, which is equivalent for the potentials of point spread function (PSF) of the optical setup. **(Right)** Smectic potential barriers as a function of virus concentration. In all graphs, black symbols correspond to pristine i.e. repulsive rods, while red ones correspond to tip-labeled particles.

Typical trajectory of patchy rod from the second population (which corresponds to viruses bound by one of their tips to the two-dimensional cluster) is shown in Fig. 3.5C. Two-dimensional clusters have been defined as the regions with increased red signal compared to the signal coming from homogeneous smectic domains (Fig. 3.5A). Patchy rods with “anchored” self-diffusion do not show significant displacements compared to the “free” (from the first population) particles (Fig. 3.5 B,C). We have also characterized two types of sticky viruses in smectic A by plotting their angular distribution with respect to director (Z-axis). Gaussian fits of these distributions $y = A \exp \left[-\frac{1}{2} \left(\frac{\alpha - \alpha_0}{w} \right)^2 \right]$, where y is the probability, α_0 is the center of the distribution α is angle value, give the same standard deviation values of around $w \approx 3.5^\circ$ for both anchored and free particles (see details in Appendix, section A5). It means, that local particle concentration within clusters and far from them within homogeneous smectic layers is similar.

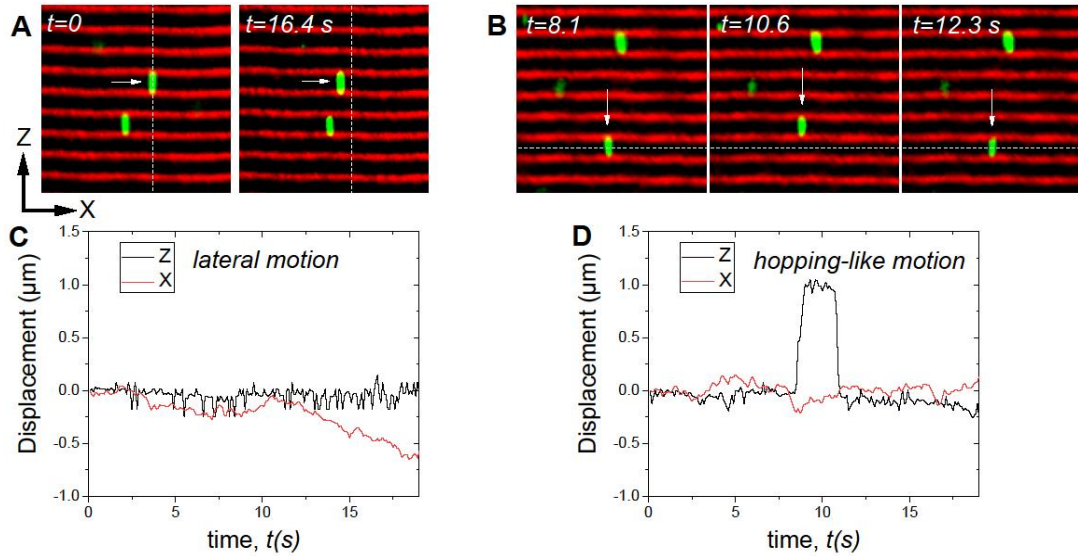


Fig. 3.4. Optical fluorescence microscopy images at different times displaying lateral (A) and hopping-like (B) motions in smectic A ($c_{\text{virus}} = 101 \text{ mg/ml}$) bulk of patchy rods. The vertical and horizontal dashed lines are plotted to point out the particle displacements within and between smectic layers, respectively. Scale bars are provided by the $1 \mu\text{m}$ smectic layer spacing periodicity. Examples of the trajectories which reveal the patchy rod motion within the layer (C), and rare jump events between adjacent layers (D). White arrows indicate the particles whose trajectories are plotted in (C) and (D).

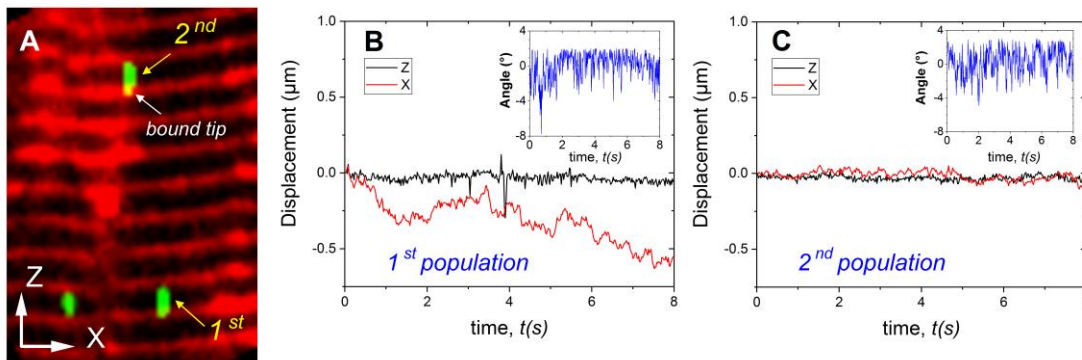


Fig. 3.5. (A) Optical fluorescence microscopy image of smectic A ($c_{\text{virus}} = 101 \text{ mg/ml}$) phase showing patchy virus from cluster-free homogeneous smectic domain which perform translational diffusion (first population); and tip-labeled virus which perform "anchored" self-diffusion as one of its ends is bound to a cluster (second population). Clusters have been identified as the regions with increased red signal compared to the signal coming from homogeneous smectic domains. Scale bars are provided by the $1 \mu\text{m}$ smectic layer spacing periodicity. Examples of patchy rod trajectories which belong to homogeneous smectic domains

(**B**), and of the particles which bound to the cluster at their tip (**C**). Insets in (**B**) and (**C**) represent the angle time evolution of the patchy viruses with respect to the Z-axis.

MSD of the first population of patchy rods in smectic A phase are calculated and compared to MSD of pristine viruses (Fig. 3.6). The log-log representations of data points indicate two different slopes for parallel and perpendicular MSD values. At short times, we find a subdiffusive behavior ($\gamma < 1$) for both types of viruses, while at long times the diffusive regime ($\gamma \approx 1$) is recovered. The crossover between the two diffusion modes occurs at approximately $\tau = 0.4 \div 0.5$ s for both pristine and patchy viruses (see details in Appendix, section A1). Both parallel and perpendicular diffusion exponents lie within the range of $\gamma_{\parallel,\perp} = 0.4 - 0.8$ for patchy viruses while they span the interval of $\gamma_{\parallel,\perp} = 0.7 - 0.9$ for pristine rods (see details in Appendix, section A3). As γ decreases when approaching crystalline states in suspension of fd viruses, we can use this parameter to characterize the ordering of colloidal dispersions. Therefore, due to lower values of γ we can conclude that patchy viruses in smectic A phase are more ordered compared to their pristine counterparts.

Dynamics in smectic A phase can be considered as the virus motion in periodic one dimensional potential field induced by layers. Each smectic layer acts as a “cage” which constrains rod motion in parallel direction. The cage effect is evident from the particle MSD [25] (Fig. 3.6). When particle motion is compatible with the size of the cage, their diffusion is impeded by other rods which results in subdiffusive behavior characterizing by $\gamma < 1$ at short times. When virus displacement is larger than the size of the cage, it corresponds to the diffusion in the colloidal dispersion describing by diffusive behavior with $\gamma = 1$. Therefore, crossover time τ between the two diffusion modes can be used to estimate the width of the cage in smectic A phase of our colloidal rods by using expression $l_{cage} = \sqrt{2D\tau}$, where D is the translational diffusion rate. Taking typical values of D_{\parallel} for pristine viruses (see section 3.2.2) which are $0.1 \div 0.23 \frac{\mu\text{m}^2}{\text{s}}$, and value of $\tau = 0.4 \div 0.5$ s, we can estimate the typical cage width as $l_{cage} = 0.2 \div 0.6 \mu\text{m}$. These values are compatible with the smectic layer spacing value which is of $1 \mu\text{m}$. Therefore for non-labeled rods, smectic layers can be considered as cages which confine their motion. As parallel and perpendicular rod displacements are not independent due to particle penetration into adjacent layers, cage effect and, thus, subdiffusive behavior should also emerge in the direction normal to the main virus axis.

Overall, from MSD curves in Fig 3.6, we conclude that self-diffusion of patchy rods is more hindered compared to self-diffusion of pristine ones due to presence of local directional interaction which induce higher smectic ordering potential in tip-labeled viral dispersions (see section 3.2.2).

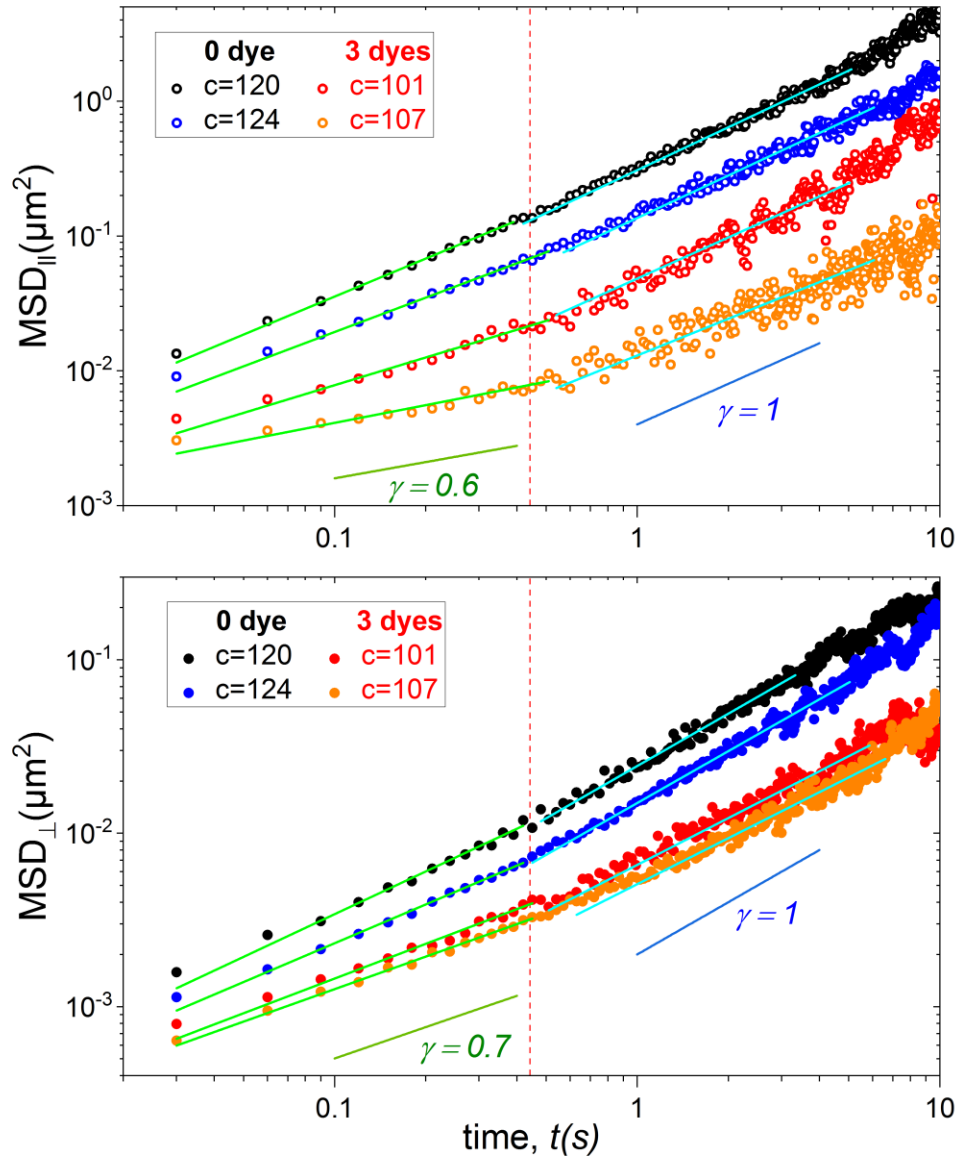


Fig. 3.6. Log-log representations of parallel (top) and perpendicular (bottom) examples of MSD at different rod concentrations of pristine and patchy viruses in and smectic A phase. Virus concentrations for 0 and 3 dyes are indicated in units of mg/ml. Subdiffusive regime is found at short times, whereas diffusive mode is recovered at long times. Green and blue lines indicate the slopes corresponding to subdiffusive and diffusive regimes respectively. Dashed red lines indicate the crossover time $\tau = 0.4 \div 0.5$ s between two diffusion regimes.

3.2.1.3 Nematic phase

Patchy rods from the first population in the nematic domains diffuse qualitatively in the same way as pristine particles do: there is mainly continuous anisotropic diffusion along viral main axis which corresponds to the nematic director. Detailed analysis of patchy rod self-diffusion from the first population in nematic phase shows that their motion is more complex compared to that of pristine rods.

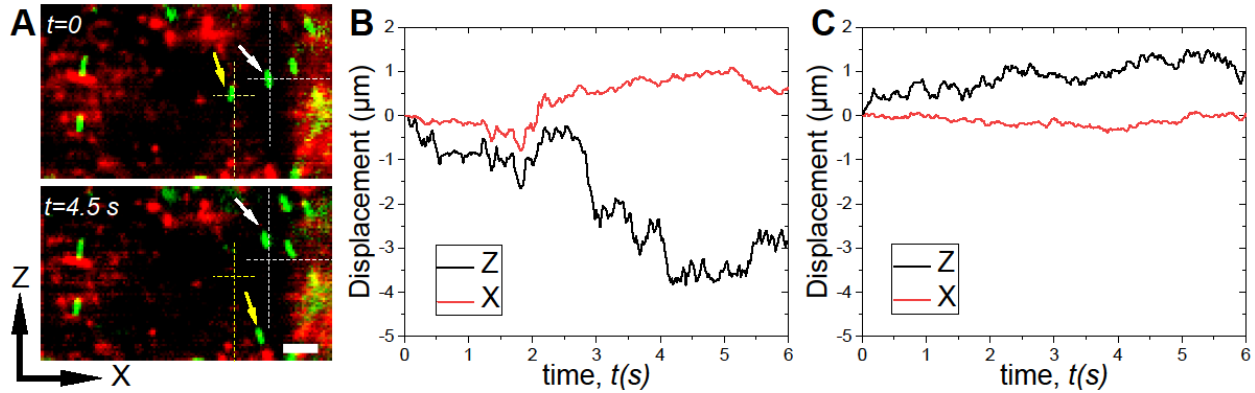


Fig. 3.7. (A) Optical fluorescence microscopy images at different times representing the nematic phase ($c_{\text{virus}} = 79 \text{ mg/ml}$) of patchy rods where the director corresponds to Z-axis. The crossed dashed lines are drawn for visual guide to bring attention to the particles which exhibit relatively long (B) and short (C) parallel displacements. Scale bar: $2 \mu\text{m}$. Yellow arrows indicates the particle with longer displacement, whereas white ones indicate the particles with short displacement.

We found that tip-labeled viruses reveal wide distributions of trace extension values in both parallel and perpendicular directions to nematic director: from up to several micrometers down to the fractions of micrometer (Fig. 3.7), whereas raw rods show in average uniform distribution for a given time range. For a given rod concentration, it results in relatively wide distribution of MSD curves calculated individually for each patchy particle, while the distribution for pristine particles is much narrower (see details in Appendix, section A2). In Fig. 3.7 we presented the trajectory examples for two patchy rods demonstrating relatively long (Fig. 3.7B) and short (Fig. 3.7C) parallel viral displacements. We argue that these two viruses belong to two clusters made of different amount of patchy rods. If cluster is relatively small (relatively low number of constituent rods), the red signal coming from the viral tips is too low to be measured and observed by optical microscopy, thus, we can observe only the biggest clusters. As

we added only a tiny amount of viruses with combined labeling into patchy dispersions (roughly one green virus per ten thousands of patchy viruses $1:10^4$), not all rods which belong to the cluster are expected to be body-labeled. It is reasonable to presume that the mobility of cluster decreases with increasing its number of constituting particles. Therefore patchy viruses with varied parallel displacements represent the displacements of two-dimensional clusters with different number of constituting rods.

However, if the two-dimensional cluster is big enough to be detected by fluorescent microscopy, we can observe binding (Fig. 3.8) and unbinding (Fig. 3.9) events for patchy rods. Binding event is a rod transition from the nematic background to the state when rod is bound to the cluster and exhibits anchored self-diffusion characterizing by only local rotation with one rod end being immobile (anchored self-diffusion will be discussed in section 3.2.1.4, Fig.3.11A). Unbinding event occurs in the opposite direction: from anchored self-diffusion to anisotropic motion in the nematic domains.

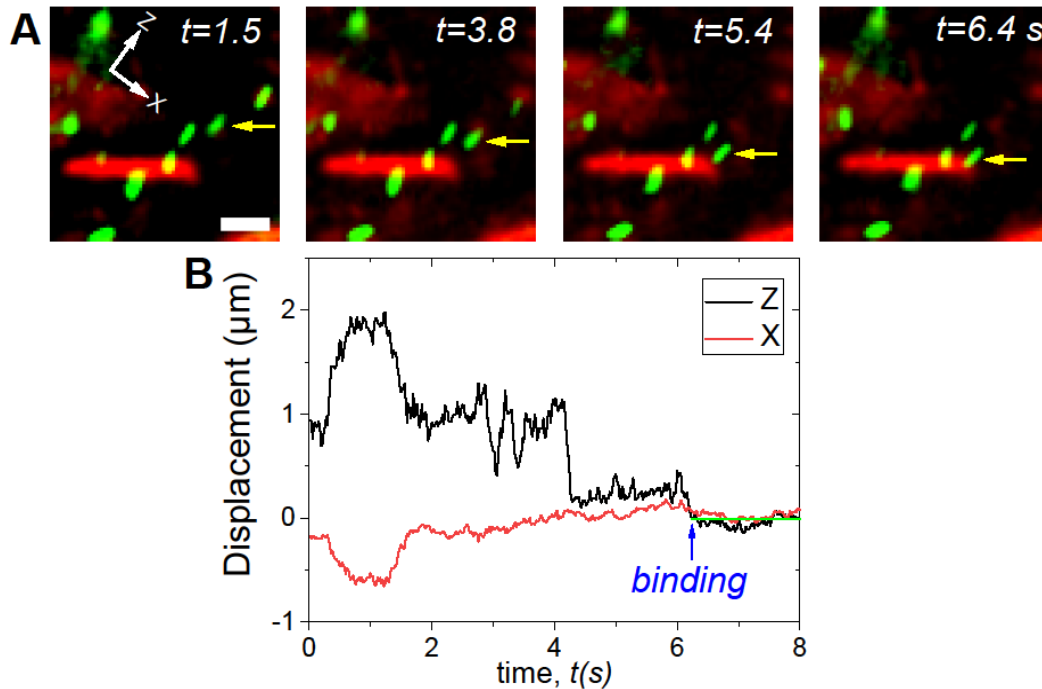


Fig. 3.8. (A) Optical fluorescence microscopy snapshots showing the binding of a patchy rod to bilayer “lamellae” dispersed in a nematic background ($c_{virus} = 70 \text{ mg/ml}$). Yellow arrows indicate the binding particle. Nematic director corresponds to Z-axis. Scale bar: $2 \mu\text{m}$. (B) Typical trajectory of a particle displaying binding event. Green horizontal line is plotted to emphasize the time interval when patchy rod is bound to cluster and exhibits the anchored self-diffusion.

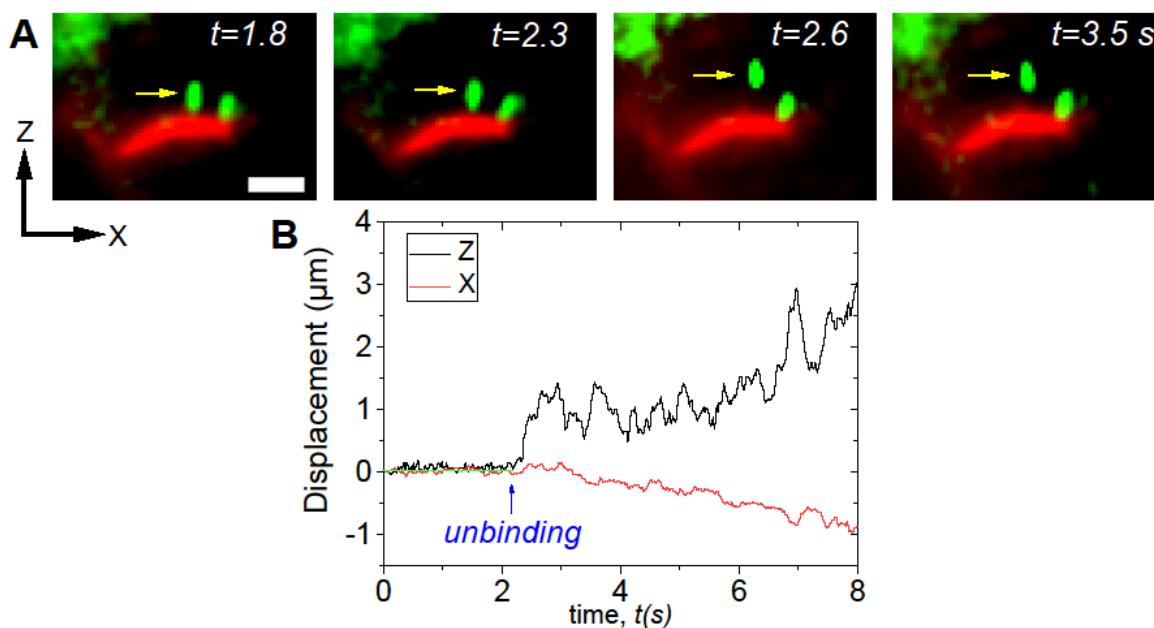


Fig. 3.9. (A) Optical fluorescence microscopy snapshots representing the unbinding event of a patchy rod from the bilayer “lamellae” toward a nematic background ($c_{\text{virus}} = 70 \text{ mg/ml}$). Scale bar: $2\mu\text{m}$. (B) Typical trajectory of the particle showing an unbinding event. Green horizontal line is drawn to emphasize the time interval when patchy rod reveals the anchored self-diffusion before being transferred from the cluster to the nematic bulk.

Parallel and perpendicular MSD of patchy viruses based on trajectories from the first population (typical anisotropic self-diffusion in nematic phase with displacement mainly occurring along the director) are calculated and compared to that of raw viruses. We found that both pristine and patchy rods exhibit diffusive regime $\gamma_{\parallel,\perp} \approx 1$ in the direction parallel to the director. In perpendicular direction, raw rods are found to reveal subdiffusive regime $\gamma_{\parallel,\perp} < 1$ at short time ($t < 0.4 \text{ s}$), and diffusive regime at long time, while patchy rods reveal subdiffusive behavior over all observation window (Fig. 3.10). The reason of subdiffusive behavior in perpendicular direction ($\gamma_{\perp} < 1$) of our pristine dispersions in the nematic phase is not clear. Previous study on fd evidenced diffusive regime in nematic state for perpendicular self-diffusion in all time range [4]. One might expect the same behavior for our M13 viruses, thus, this question remains open. In case of perpendicular self-diffusion of patchy rods, we argue that diffusive regime is not recovered because rod motion is suppressed due to their involvement into relatively small clusters.

Overall in nematic phase, we have found decreasing of tip-labeled rod mobility compared to raw rods, which can be explained by local attraction between viral ends as well as patchy rods involvement into two-dimensional clusters of varied size.

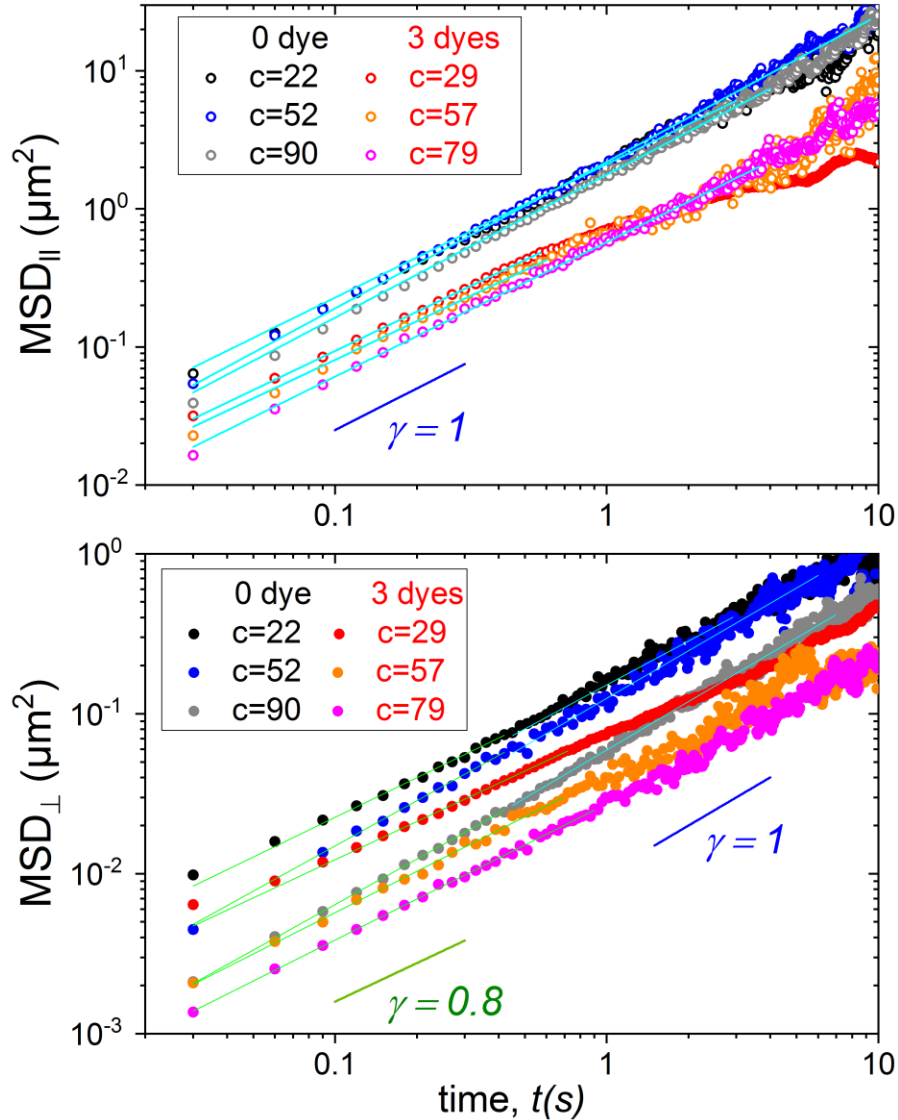


Fig. 3.10. Parallel (top) and perpendicular (bottom) MSD of patchy and raw viruses in nematic phase. Virus concentrations for 0 and 3 dyes are indicated in units of mg/ml. Pristine and patchy rods exhibit diffusive regime $\gamma_{||,\perp} \approx 1$ in parallel direction. In perpendicular direction there is subdiffusive regime at short times and diffusive regime at long times for pristine rods; and only subdiffusive regime for patchy rods. Green and blue lines indicate the slopes corresponding to subdiffusive and diffusive modes respectively.

3.2.1.4 Isotropic liquid phase

The main feature of patchy dispersions in isotropic liquid phase is that the majority of patchy rods are bound to the two-dimensional clusters by one of their ends revealing anchored self-diffusion. Therefore, most of tip-labeled rods belong to the second population of patchy viruses. In Fig. 3.11A we demonstrated the large field of view capturing tip-functionalized viruses anchored to the lamellae. They perform local rotational self-diffusion with significant angular displacement (Fig. 3.11B). Gaussian fit of distributions of angular displacements for anchored rods in isotropic phase gives standard deviation value of around 10° (see details in Appendix I, section A5). Angle distributions for patchy rods from the first population in the isotropic phase are expected to be uniform as there is no orientational order, therefore the value of angle standard deviations should be zero. Translational self-diffusion of patchy rod reveals no significant displacement of a single anchored particle (Fig. 3.11C), but it demonstrates the global motion performed by the whole cluster in colloidal suspensions.

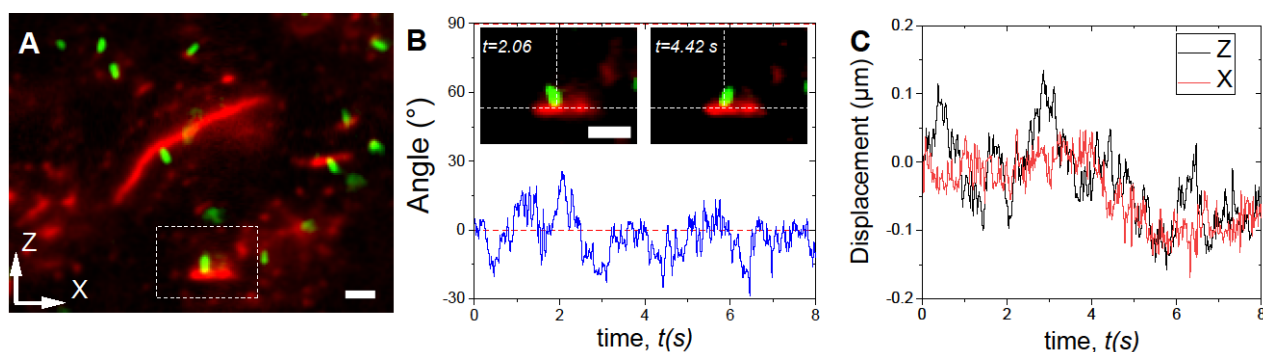


Fig. 3.11. (A) Overlay of fluorescence microscopy images of patchy viruses in dense isotropic phase ($c_{virus} = 15 \text{ mg/ml}$) showing anchored viruses to the clusters. Scale bar: $2\mu\text{m}$. (B) Angle evolution of patchy rod anchored to lamellae with respect to Z-axis [dotted white box in (A)]. The insets represent the two maximum virus deviations from its average orientation shown by the vertical dashed line (horizontal dashed line indicated the “lamellae” orientation). Scale bar: $2\mu\text{m}$. (C) Corresponding displacement of center of mass of the patchy virus involved into bilayer cluster evidencing the anchored self-diffusion combined with collective motion of whole cluster.

In order to evidence the motion of single patchy rods from the first population (not involved into two-dimensional clusters), we have prepared isotropic suspension with viral

concentration lower than overlap one ($c^{overlap} = 3/4\pi L_{virus}^3$; $c_{M13KE,M13C7C}^{overlap} = 0.04$ mg/ml) in which *all* particles received combined labeling meaning all patchy rods are body-labeled by green dye molecules. At these conditions all two-dimensional clusters are fully dissolved and only single patchy particles are observed (Fig. 3.12A). To avoid overlap of particle traces, we have prepared dispersion at very low particle concentration of about $c_{virus} \sim 10^{-4}$ mg/ml. It is worth stressing that the red signal coming from viral tips is too low to be measured and detected for this range of rod dilution. Typical trajectory of single patchy rod with no preferential direction of motion, contrary to smectic and nematic phases, is reported in Fig. 3.12B.

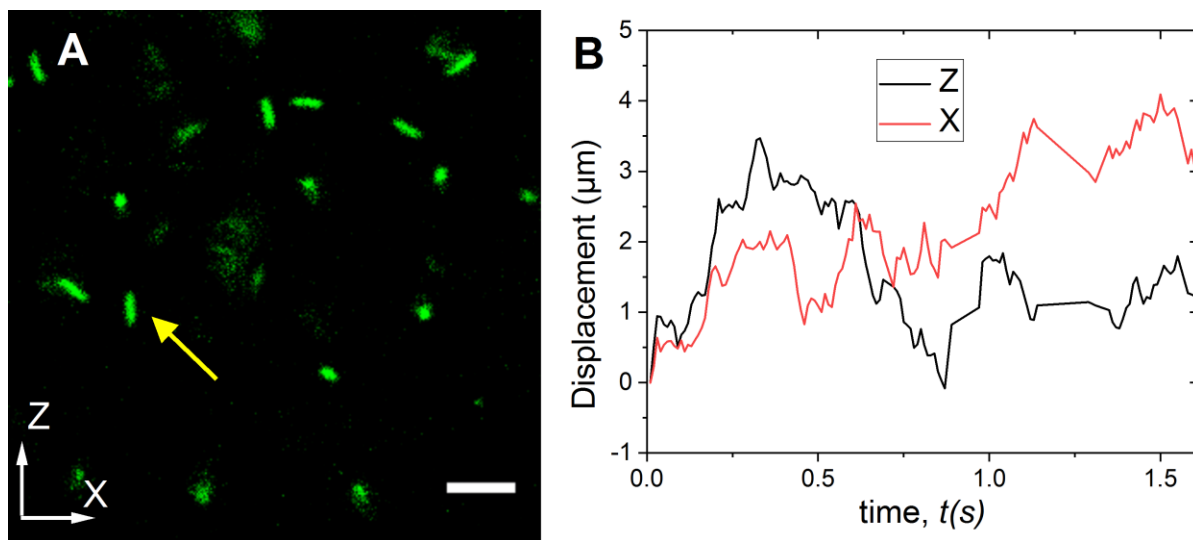


Fig. 3.12. (A) Optical fluorescence microscopy image showing patchy viruses at very low virus concentration ($c_{virus} \sim 10^{-4}$ mg/ml) where all particles have received green dyes body-labeling. Scale bar: $2\mu\text{m}$. (B) Typical trajectories of center of mass of a single virus. Yellow arrow indicates the rod whose trajectory is plotted in (B).

In our experiments we detect 2D-projection of 3D isotropic rod motion, thus, we cannot properly distinguish parallel and perpendicular components of viral displacements due to difficulties of determining the angle between rod main axis and *Z*-axis for a given snapshot (Fig. 3.12.A). Thus, when quantifying MSD, we set *Z*-axis as a *pseudo-parallel* "(||)" and *X*-axis as a *pseudo-perpendicular* "(⊥)" component of particle displacements (Fig. 3.12A). Results reported in Fig. 3.13 indicate diffusion regime ($\gamma = 1$) for patchy and pristine rods at very low rod concentration.

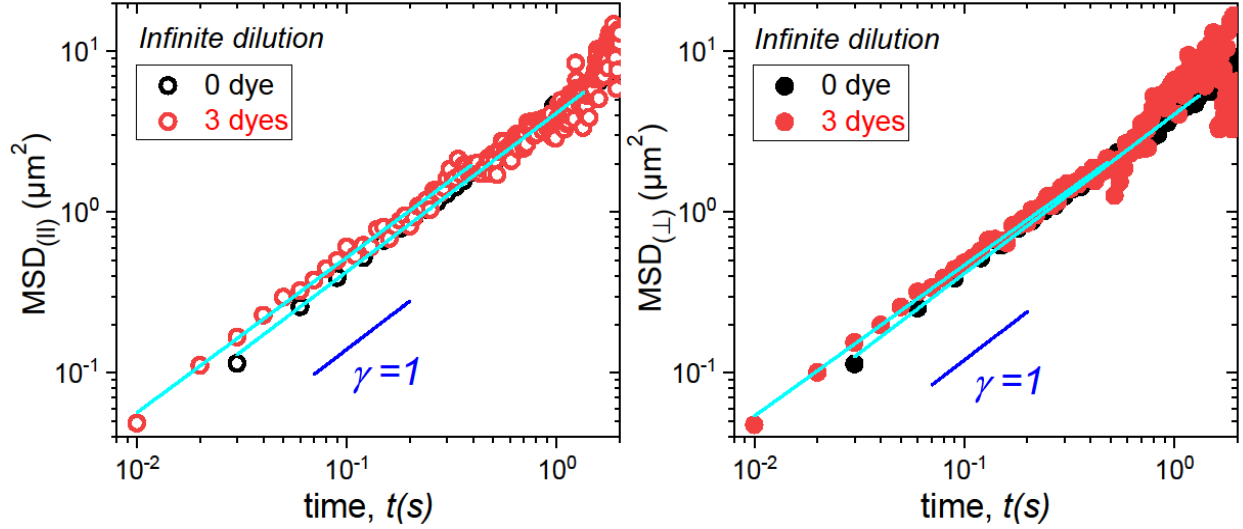


Fig. 3.13. Pseudo-parallel (left) and pseudo-perpendicular (right) MSD of pristine and patchy viruses at very low rod concentration ($c_{virus} \sim 10^{-4}$ mg/ml). Blue sloped lines are for eye guide to illustrate the diffusive regime $\gamma = 1$.

Our experimental finding show that both patchy and pristine self-diffusion values in pseudo-parallel and pseudo-perpendicular (Z-axis and X-axis in Fig. 3.12.A) directions are nearly equal: $D_{(||)} \approx D_{(\perp)} \approx 2.2 \mu\text{m}^2/\text{s}$. It is reasonable to assume that from our experimental output the total virus self-diffusion equals to $D_{tot}^{exp} = \frac{1}{2}(D_{(||)} + D_{(\perp)})$. It gives experimental value of total self-diffusion to be equal $D_{tot}^{exp} \approx 2.2 \mu\text{m}^2/\text{s}$. According to the theoretical predictions [17], rod diffusion at infinite dilution is $D^{theor} = \frac{1}{3\pi} \frac{k_B T \cdot \ln(L/D)}{\eta_0 L}$, where L and D is rod length and diameter respectively, and η_0 is solvent viscosity. Taking parameters of our viral rods $L = 1 \mu\text{m}$, $D = 7 \text{ nm}$ and viscosity of colloidal water dispersion $\eta_0 = 10^{-3} \text{ Pa} \cdot \text{s}$, we have calculated the theoretical value of virus self-diffusion $D_{tot}^{theor} = 2 \mu\text{m}^2/\text{s}$ at very low particle concentration. We found a quantitative agreement between theoretical and experimental self-diffusion values for rods in the deep isotropic phase indicating that local attraction between viral tips (induced by 3 and 10 dyes per rod end) has no effect on particle mobility at rod concentration which is lower than the overlap concentration.

3.2.2 Self-diffusion coefficients of patchy and pristine rods

To characterize and compare dynamical behavior in liquid crystalline dispersion of tip-functionalized and pristine viral rods, the translational self-diffusion coefficients D_{\parallel} and D_{\perp} for both systems are calculated via expression $MSD_{\parallel,\perp} = 2D_{\parallel,\perp}t^{\gamma_{\parallel,\perp}}$.

In columnar and smectic B liquid crystalline states, due to lack of significant rod self-diffusion, we did not calculate self-diffusion rates for these phases.

In smectic A phase of both patchy and raw viral dispersions, we detect two types of behavior: subdiffusive regime at short times and diffusive regime at long times (Fig. 3.6). Self-diffusion rates which correspond to two diffusion regimes are found to be nearly equal: $D_{\parallel,\perp}^{short} \approx D_{\parallel,\perp}^{long}$. We find that both D_{\parallel} and D_{\perp} for patchy rods are roughly one order of magnitude lower than that for rods with purely repulsive interaction (Fig. 3.14). This slowing down of tip-labeled rod self-diffusion can be explained mainly by higher smectic ordering potential in patchy dispersions induced by local attraction between viral tips.

In nematic state of patchy and in chiral nematic state of pristine rods, we detected diffusive behavior during the whole observation time in parallel direction. In perpendicular direction, raw rods are shown to possess slight subdiffusive behavior at short times, and diffusive one at long times, while patchy rods exhibit subdiffusive regime over all time observation range. The origin of subdiffusive behavior in perpendicular direction ($\gamma_{\perp} < 1$) for pristine rods is unknown and requires further studies. In case of patchy viruses, we interpret subdiffusive behavior as rod involvement into two-dimensional clusters of varying size. Numerical fit yielded self-diffusion values for tip-labeled viruses in both directions to be around five times lower than the values for raw particles (Fig. 3.14). We argue that tip-labeled rod mobility in nematic phase is hindered compared to pristine non-labeled rods due directional attraction between viruses and their involvement into clusters.

Self-diffusion values of patchy and pristine rods converge at very high rod dilution below viral overlap concentration. This can be caused by relatively short range of patchy attraction between viral tips, which does not affect the viral mobility at highly diluted states.

In Fig. 3.14, we report the evolution of parallel and perpendicular diffusion rates (D_{\parallel} and D_{\perp}) in nematic and smectic A ranges of viral dispersions. Anisotropy D_{\parallel}/D_{\perp} of self-diffusion

rates is also shown as a function of rod concentration. Anisotropy of raw rods is around twice as high as one of patchy rods in smectic A phase, while it is about 50% higher in nematic state.

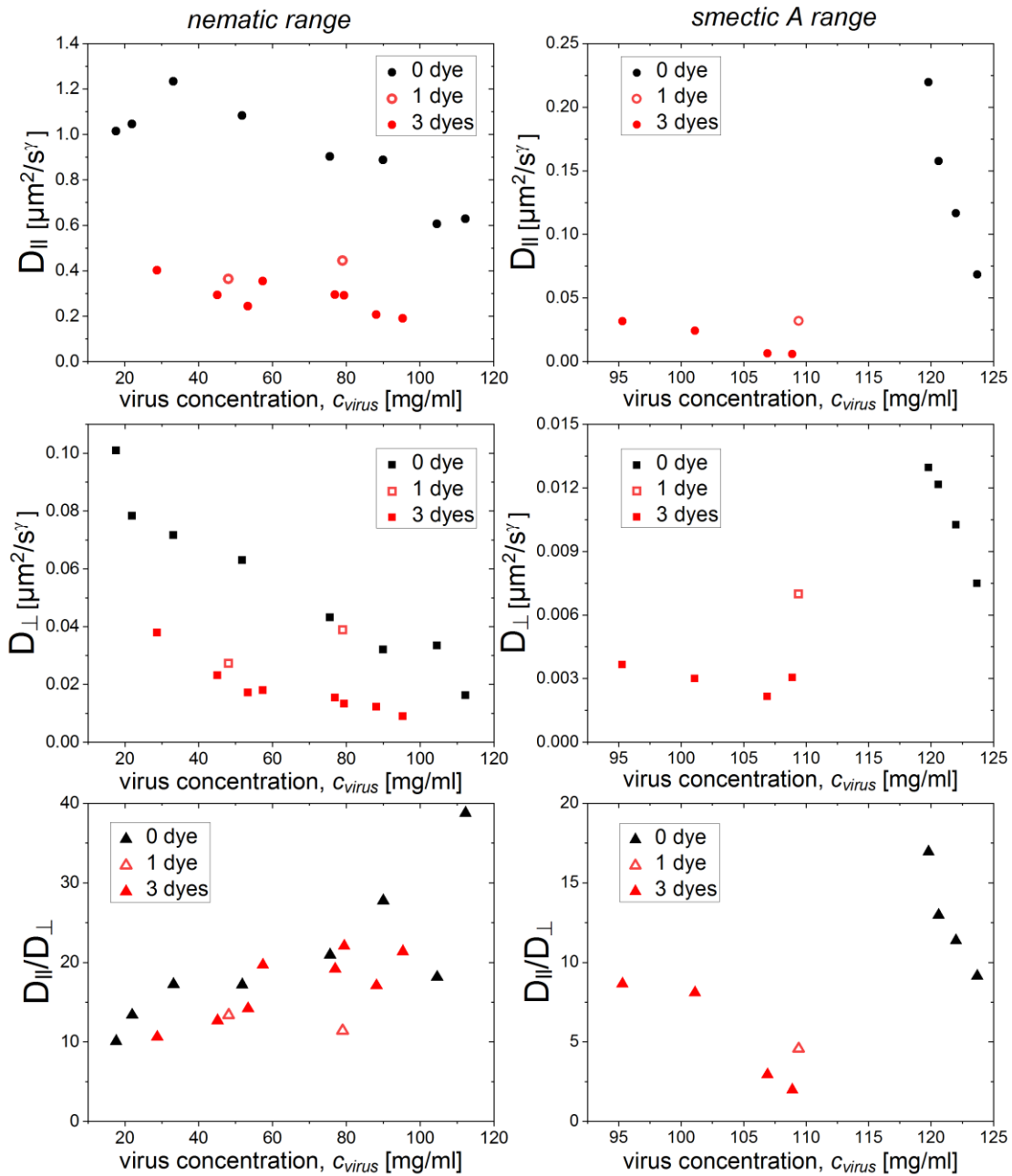


Fig.3.14. Parallel D_{\parallel} and perpendicular D_{\perp} self-diffusion rates as well as their ratio D_{\parallel}/D_{\perp} for raw and patchy viruses (for suspensions with both 1 and 3 dyes) in nematic (left) and smectic (right) phases. D_{\parallel} and D_{\perp} values are obtained via fit of MSD using expression $\text{MSD}_{\parallel,\perp} = 2D_{\parallel,\perp}t^{\gamma}$.

3.2.3 Orientational order parameter in patchy and pristine suspensions

By using angular displacement distributions which reveal typical anisotropic self-diffusion occurring mainly along the director in nematic and smectic A phases (see Appendix, section A4) of raw and patchy rods (first population of patchy particle), we have calculated the orientational order parameter $P_2 = \langle \frac{3}{2} \cos^2 \alpha - \frac{1}{2} \rangle$, where α is local angle value characterizing rod main axis deviation from the director. We found that the behavior of P_2 is nearly the same for raw and patchy viruses in both nematic and smectic A phases (Fig. 3.15). It is consistent with the fact, that local attraction between viruses does not affect the isotropic-nematic phase transition.

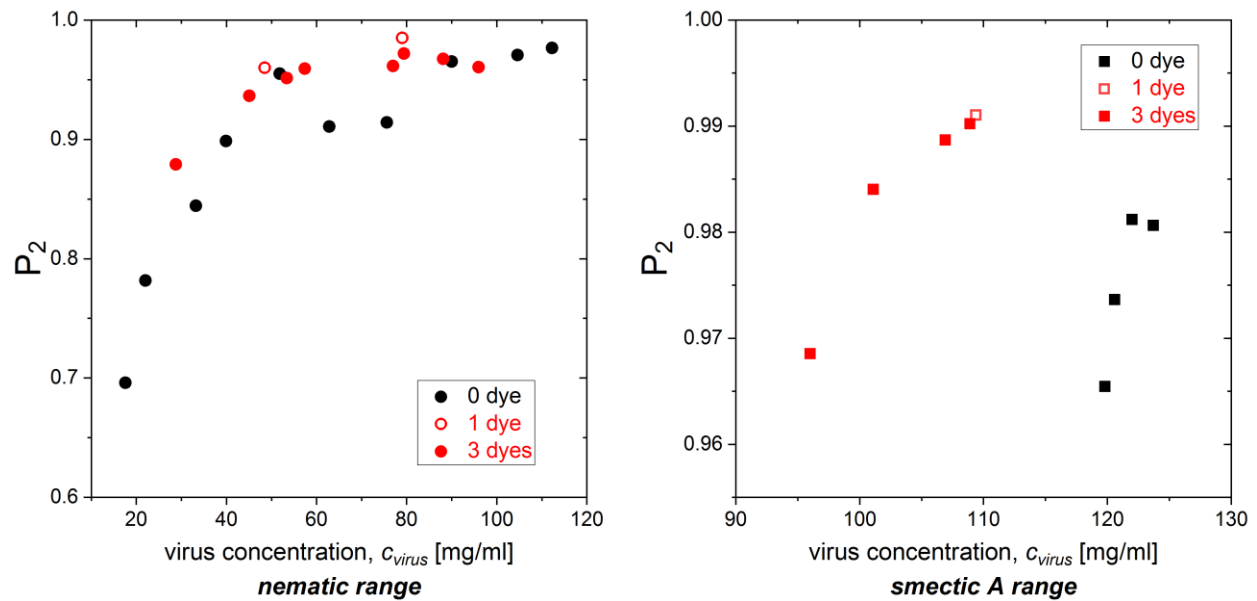


Fig.3.15. Orientational order parameter $P_2 = \langle \frac{3}{2} \cos^2 \alpha - \frac{1}{2} \rangle$, where α is local angle value characterizing rod main axis deviation from the director, for 0, 1, and 3 dyes in nematic (left) and smectic (right) phases.

We also compare angular displacement distributions for patchy rods with typical anisotropic self-diffusion (first population) and anchored self-diffusion of rods involved into two-dimensional clusters (second population) [see Appendix, section A5]. Orientational order parameters P_2 are, thus, also calculated for two populations of rods showing nearly the same values for both types of sticky particles in nematic and smectic A states (Fig. 3.16). Therefore, the local concentration of rods which bound to clusters is the same to the rod concentration in the bulk. Note that P_2 for the first population of particles is zero in the isotropic phase, whereas it

has non-zero value for the anchored particles as their rotational self-diffusion is restricted due to attachment to the two-dimensional clusters.

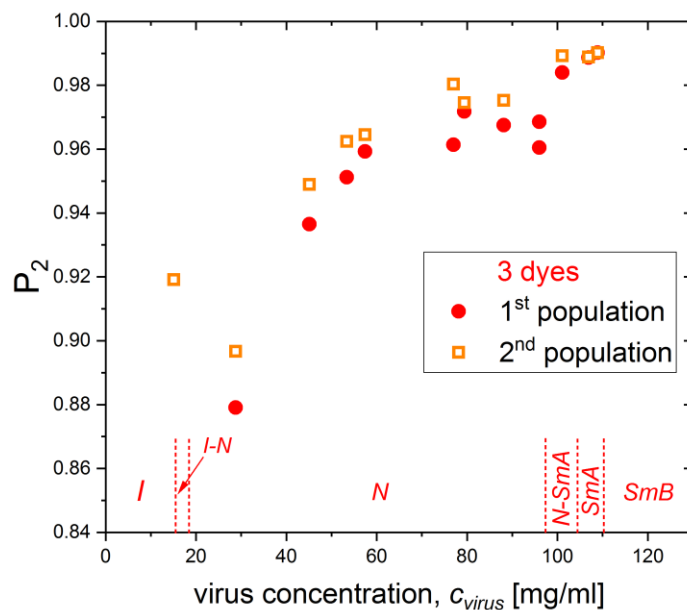


Fig.3.16. Orientational order parameter P_2 for patchy particles (3 dyes system) from the first population (typical anisotropic self-diffusion in nematic and smectic A) and the second population (anchored self-diffusion). The red dashed lines at the bottom of the graph indicate the phase diagram of patchy virus suspension.

3.3 Conclusions

Our findings show that dynamical behavior of patchy and pristine i.e. purely repulsive rods is markedly different. We distinguish two populations of patchy viruses. The first population behaves qualitatively similarly to the rods with purely repulsive interaction showing anisotropic self-diffusion with main displacement along the director in nematic and smectic phases. This fraction of viruses has been used to establish the concentration evolution of translational self-diffusion coefficients. The second population is unique to patchy viral dispersions, and contains sticky rods which are bound at one of their ends to the two-dimensional clusters revealing “anchored” self-diffusion and lack of significant translational motion

The comparison of self-diffusion coefficients reveals stark contrast between the mobility of patchy and raw viruses. Lower values for tip-functionalized rods suggest the existence of a mean-field attraction in patchy dispersions induced by sticky inclusions on particle tips

uniformly distributed throughout the suspensions volume. This mean-field promotes increasing smectic ordering potential in lamellar state and appearance of two-dimensional clusters in all phases of viral dispersion hindering the self-diffusion of patchy rods. Directional attraction is shown not to affect the orientational order parameter of tip-labeled rod suspensions compared to pristine ones.

Overall, our dynamical studies provided deeper understanding of colloidal suspension structure with local directional interactions emphasizing the strong impact of weak patchy inclusions on properties of complex fluids.

3.4 References

- [1] M. P. Lettinga, E. Barry, and Z. Dogic. Self-diffusion of rod-like viruses in the nematic phase. *Europhys. Lett.*, 2005, 71: 692–698.
- [2] M. P. Lettinga and E. Grelet. Self-diffusion of rodlike viruses through smectic layers. *Phys. Rev. Lett.*, 2007, 99: 197802.
- [3] E. Pouget, E. Grelet, and M. P. Lettinga. Dynamics in the smectic phase of stiff viral rods. *Phys. Rev. E*, 2011, 84: 41704.
- [4] L. Alvarez, M. P. Lettinga, and E. Grelet. Fast Diffusion of Long Guest Rods in a Lamellar Phase of Short Host Particles. *Phys. Rev. Lett.*, 2017, 118: 178002.
- [5] F. Roosen-Runge et al. Protein self-diffusion in crowded solutions. *PNAS*, 2011, 108: 11815-11820.
- [6] F. Roosen-Runge et al. Protein diffusion in crowded electrolyte solutions. *Biochim. et Biophys. Acta*, 2010, 1804: 68–75.
- [7] M. Grimaldo et al. Diffusion and Dynamics of γ -Globulin in Crowded Aqueous Solutions. *J. Phys. Chem. B*, 2014, 118: 7203–7209.
- [8] S. Bucciarelli et al. Dramatic influence of patchy attractions on short-time protein diffusion under crowded conditions. *Sci. Adv*, 2016, 2: e1601432.
- [9] E. Grelet. Hexagonal order in crystalline and columnar phases of hard rods. *Phys. Rev. Lett.*, 2008, 100: 168301.

- [10] S. Naderi, E. Pouget, P. Ballesta, P. van der Schoot, M. P. Lettinga, and E. Grelet. Fractional hoppinglike motion in columnar mesophases of semiflexible rodlike particles. *Phys. Rev. Lett.*, 2013, 111: 37801.
- [11] X. Michalet. Mean square displacement analysis of single-particle trajectories with localization error: Brownian motion in an isotropic medium. *Phys. Rev. E*, 2010, 82: 041914.
- [12] A. de la Cotte, C. Wu, M. Trévisan, A. Repula, and E. Grelet. Rod-like virus based multiarm colloidal molecules. *ACS Nano*, 2017, 11: 10616-10622
- [13] E. Grelet. From soft to hard rod behavior in liquid crystalline suspensions of sterically stabilized colloidal filamentous particles. *Soft Matter*, 2016, 4621: 12.
- [14] Z. Cheng. Phase diagram of hard spheres. *Mat. and Des.*, 2001, 22: 529-534.
- [15] D. J. Kraft et al. Surface roughness directed self-assembly of patchy particles into colloidal micelles. *PNAS*, 2012, 109: 10787–10792.
- [16] A. C. Newton et al. Rotational diffusion affects the dynamical self-assembly pathways of patchy particles. *PNAS*, 2015, 112: 15308–15313.
- [17] M. M. Tirado, J. G. de la Torre. Translational friction coefficients of rigid, symmetric top macromolecules. Application to circular cylinders. *J. Chem. Phys.*, 1979, 71: 2581.
- [18] E.M. Purcell. Life at low Reynolds number. *Am. J. Phys.*, 1977, 45: 3–11.
- [19] R. Piazza. Protein interactions and association: an open challenge for colloid science. *Curr. Opin. Colloid In.*, 2004, 8: 515–522.
- [20] D.S. Banks, C. Fradin. Anomalous diffusion of proteins due to molecular crowding. *Biophys J.*, 2005, 89: 2960–2971.
- [21] M. Weiss, M. Elsner, F. Kartberg, T. Nilsson. Anomalous subdiffusion is a measure for cytoplasmic crowding in living cells. *Biophys. J.*, 2004, 87: 3518–3524.
- [22] M.J. Saxton. Anomalous diffusion due to obstacles: a Monte Carlo study. *Biophys. J.*, 1994, 66: 394–401.
- [23] M.J. Saxton. Anomalous diffusion due to binding: a Monte Carlo study. *Biophys. J.*, 1996, 70: 1250–1262.
- [24] R. Gorenflo, F. Mainardi, D. Moretti, G. Pagnini, and P. Paradisi. Discrete random walk models for space-time fractional diffusion. *Chem. Phys.*, 2002, 284: 521–541.

- [25] E. R. Weeks, D. A. Weitz. Subdiffusion and the cage effect studied near the colloidal glass transition. *Chem. Phys.*, 2002, 284: 361–367.
- [26] E. Grelet. Hard-rod behavior in dense mesophases of semiflexible and rigid charged viruses. *Phys. Rev. X*, 2014, 4: 21053.
- [27] L. Colón-Meléndez et al. Binding kinetics of lock and key colloids. *Jour. of Chem. Phys.*, 2015, 142: 174909.
- [28] T. C. B. McLeish. Tube theory of entangled polymer dynamics. *Adv. in Phys.*, 2002, 51: 1379.
- [29] A. van Blaaderen *et al.* Long-time self-diffusion of spherical colloidal particles measured with fluorescence recovery after photobleaching. *J. Chem. Phys.*, 1992, 96, 4591.
- [30] Y. Han *et al.* Brownian Motion of an Ellipsoid. *Science*, 2006, 314: 626-630.

Appendix

Effect of patchy interaction on dynamics of rod-like colloids

A1. Numerical fitting of MSD curves averaged over particles

A1.1 0 dye or pristine viral system

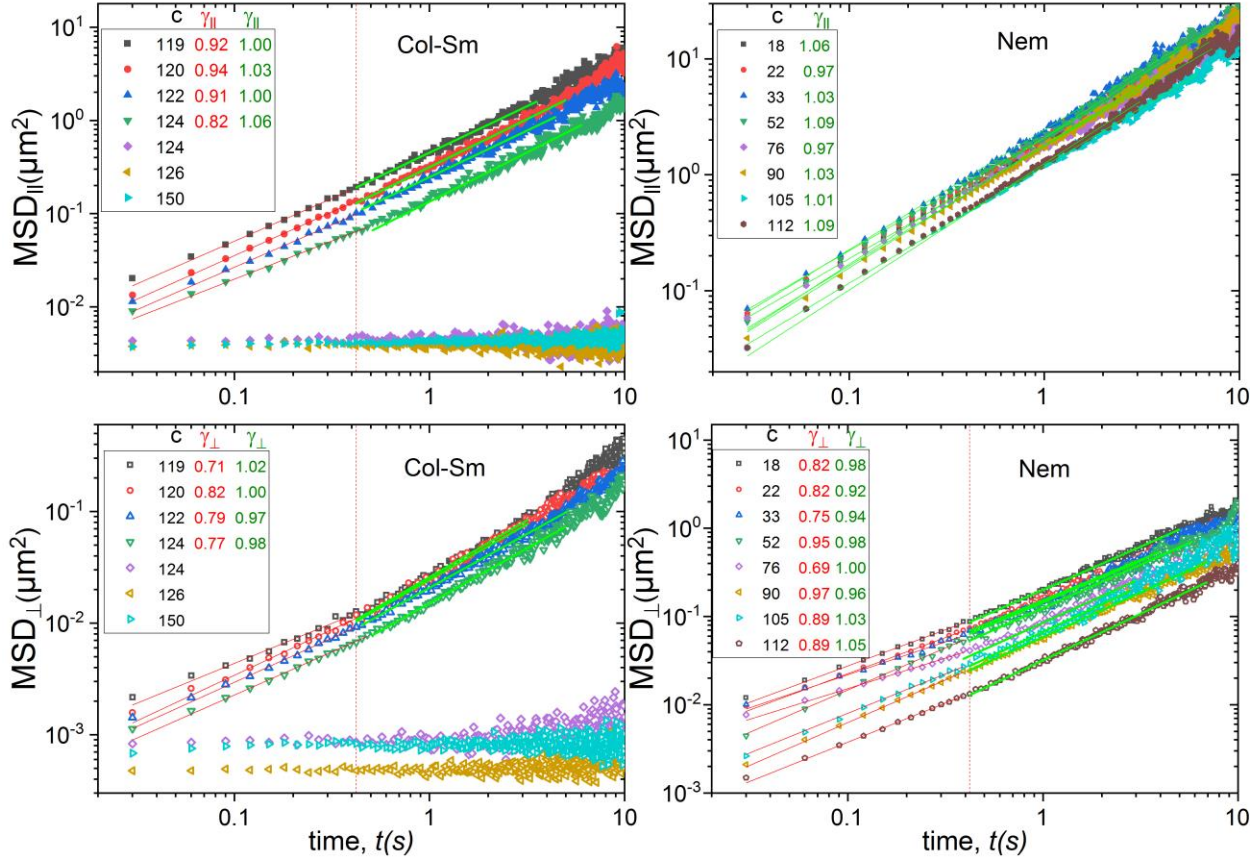


Fig. 1. Log-log representation of the parallel (top) and perpendicular (bottom) mean square displacements (MSD) for pristine viral dispersions in the columnar/smectic (left) and nematic (right) range. Black values indicate the rod concentrations in mg/ml; the red and green values indicate anisotropic exponents γ obtained from the numerical fit by a power law $MSD_{||,\perp} = 2D_{||,\perp}t^{\gamma_{||,\perp}}$ at short (subdiffusive regime) and long time scale (diffusive regime) respectively. Red dashed lines indicate the crossover time $\tau \approx 0.4 \div 0.5$ s between the two diffusion regimes.

The mean square displacements (MSD) of the pristine (0 dye) and patchy (1 and 3 dyes) systems are reported in Fig. 1, 2, and 3 respectively. The anisotropic diffusion rates $D_{\parallel,\perp}$ and exponents $\gamma_{\parallel,\perp}$, parallel (\parallel) and perpendicular (\perp) to the director, are extracted from the numerical fits of the MSD curves performed employing a power law $MSD_{\parallel,\perp} = 2D_{\parallel,\perp}t^{\gamma_{\parallel,\perp}}$ for the different virus concentrations. For consistency of the results, we adjusted the time range of the fit to keep its high quality with a minimum value for the reduced chi-square.

A1.2 Patchy system with 1 dye per rod tip

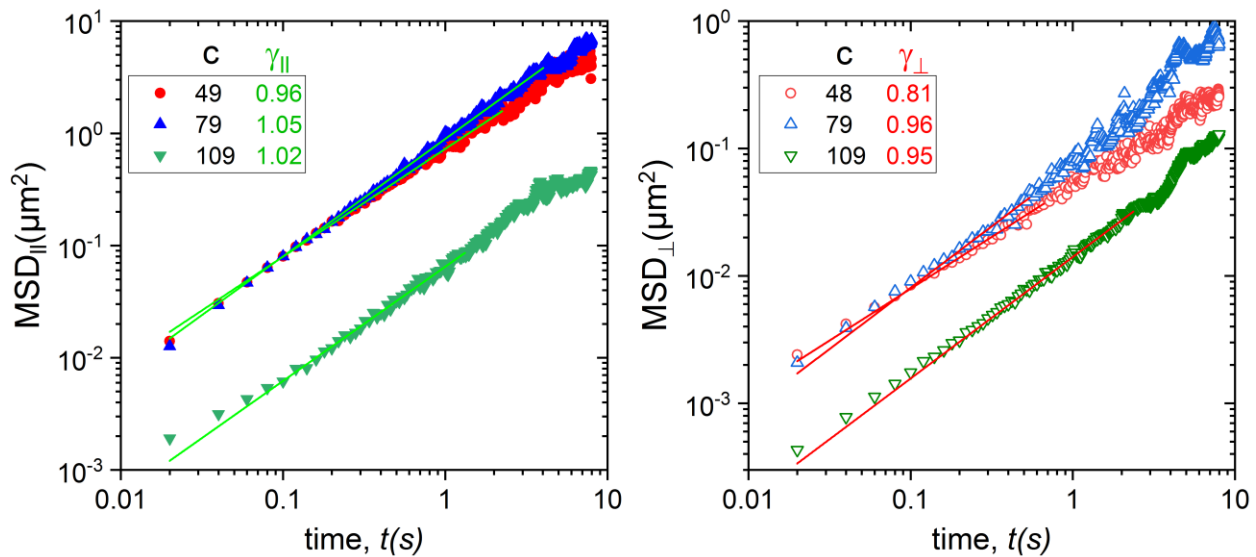


Fig. 2. Log-log representation of the parallel (left) and perpendicular (right) MSD curves for patchy (1 dye per tip) viral dispersions. Black values indicate the rod concentrations in mg/ml; green and red values indicate anisotropic exponents γ obtained from the numerical fit by a power law $MSD_{\parallel,\perp} = 2D_{\parallel,\perp}t^{\gamma_{\parallel,\perp}}$ of parallel and perpendicular component of MSD respectively. Relatively short (of around 8 s) time observation range recorded experimentally for this set of data does not allow for discrimination between different diffusion regimes at short and long time scales.

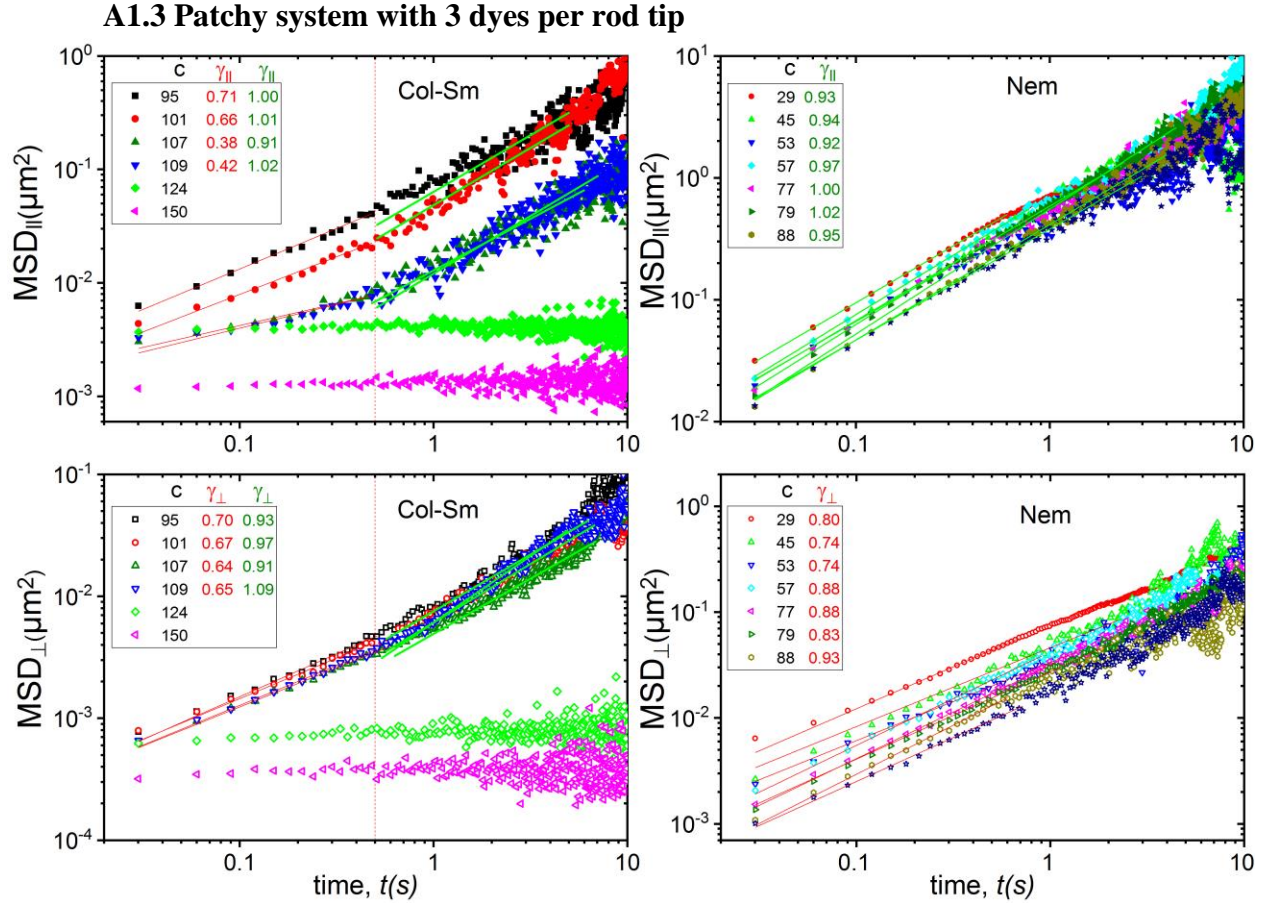


Fig. 3. Log-log representation of the parallel (top) and perpendicular (bottom) MSD for patchy (3 dyes per tip) viral dispersions in the columnar/smectic (left) and nematic (right) range. Black values indicate the rod concentration in mg/ml; red and green values indicate anisotropic exponents γ obtained from the numerical fit by power law $MSD_{||,\perp} = 2D_{||,\perp}t^{\gamma_{||,\perp}}$ at short (subdiffusive regime) and long time scale (diffusive regime) respectively. Red dashed lines indicate the crossover time $\tau \approx 0.4 \div 0.5$ s between the two diffusion regimes.

A2. Individual MSD curves of single particles

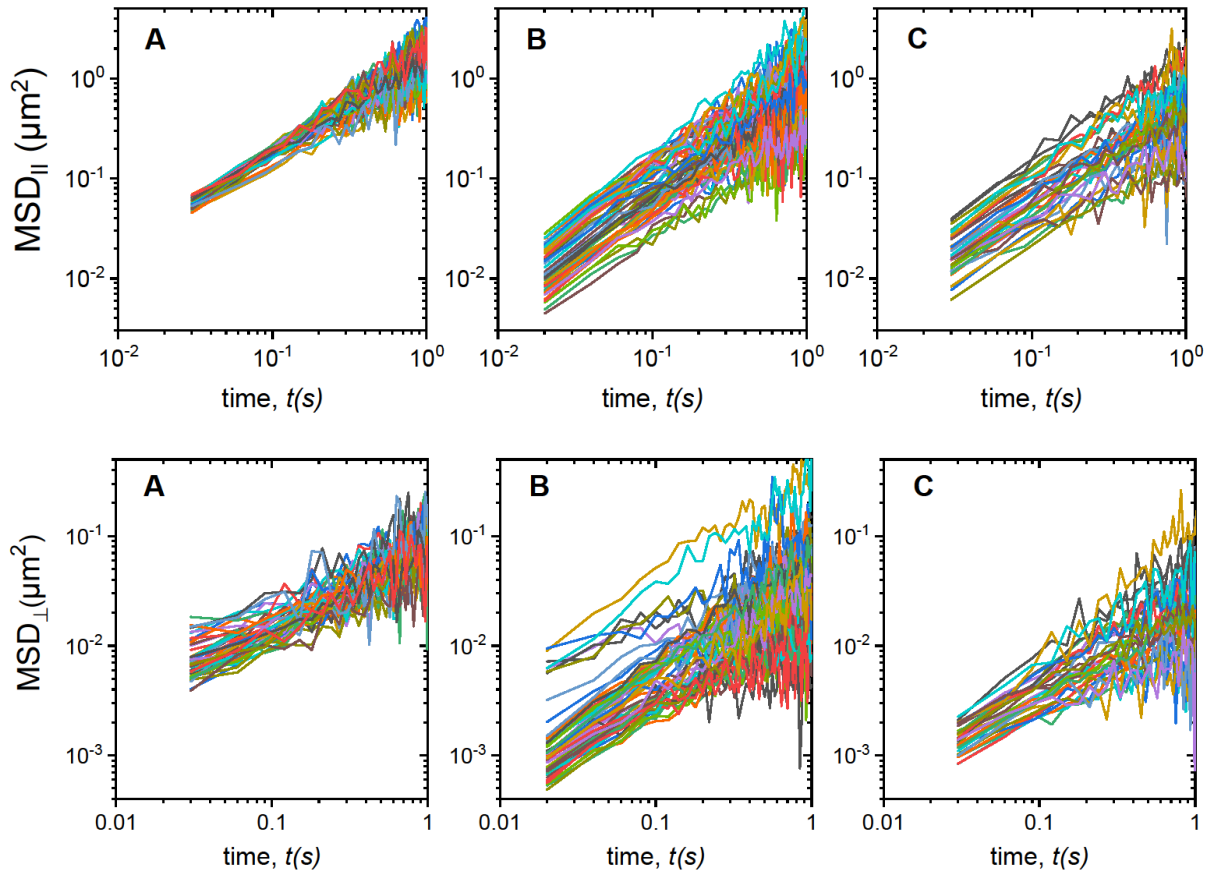


Fig. 4. Collection of parallel (top panel) and perpendicular (bottom panel) of about 50 MSD curves corresponding to each individual trajectories for (A) 0 dye (pristine viruses) system at virus concentration $c=75.6$ mg/ml, (B) 1 dye patchy system at $c=79.0$ mg/ml, and (C) 3 dyes patchy system at $c=79.4$ mg/ml. Lowering and widening of "patchy" MSD curves compared to "raw" ones indicates hindered viral self-diffusion due to attraction between rods and particle involvement into the two-dimensional clusters of varying size.

A3. Subdiffusive exponents evolution with virus concentration

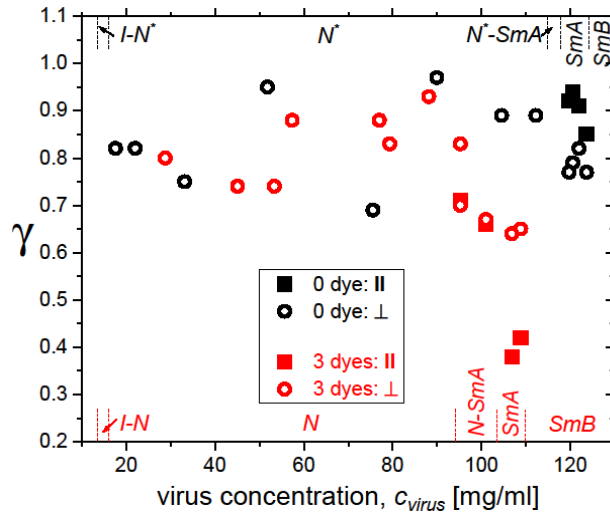


Fig. 5. Parallel (solid symbols) and perpendicular (open symbols) anisotropic exponents γ obtained from the numerical fit by a power law $MSD_{\parallel,\perp} = 2D_{\parallel,\perp}t^{\gamma_{\parallel,\perp}}$ at short time scale indicating subdiffusive behavior of patchy (red symbols) and pristine (black symbols) rods. The red dashed lines at the bottom of graphs indicate phase diagram of patchy suspension, while the black dashed lines at the top indicate phase diagram of pristine viruses (I is isotropic, N (N^*) is nematic (cholesteric), SmA is smectic A, and SmB is smectic B).

A4. Angle distributions of raw and patchy viruses from first population (typical anisotropic self-diffusion in nematic and smectic A phases)

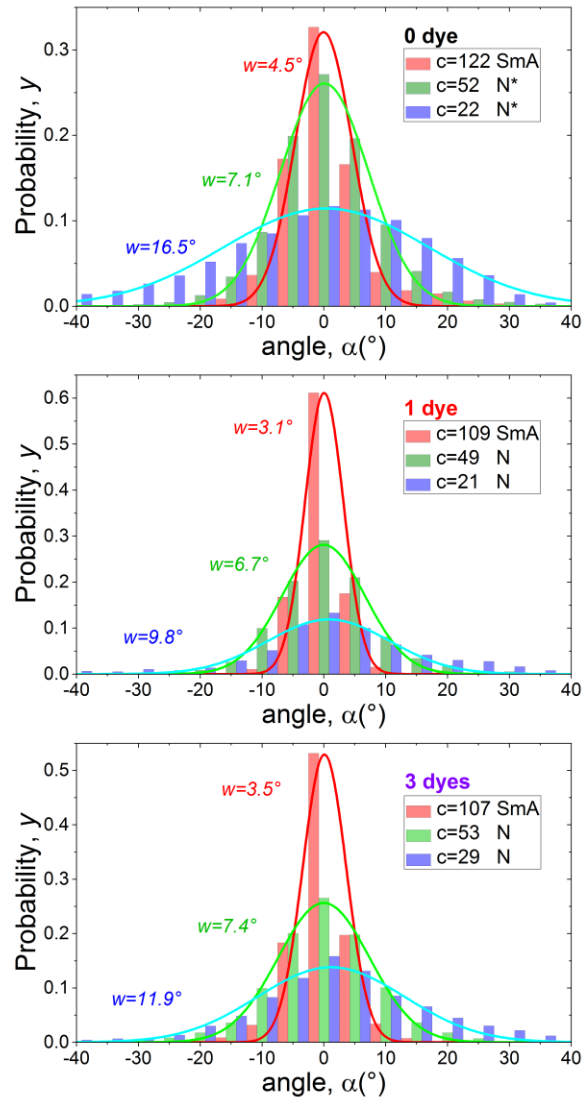


Fig. 7. Examples of the angle distributions which characterize rod deviations from the director for pristine (top) and patchy (middle and bottom) viruses from first population at three different particle concentrations. Numerical fits are performed using Gaussian function $y = A \exp \left[-\frac{1}{2} \left(\frac{\alpha - \alpha_0}{w} \right)^2 \right]$, where α_0 is the center of the distribution, and w is proportional to the full width at half maximum (FWHM) and has been used to calculate orientational order parameter (see main text, section 3.2.2)

A5 Angle distributions of patchy viruses from second population (“anchored self-diffusion”)

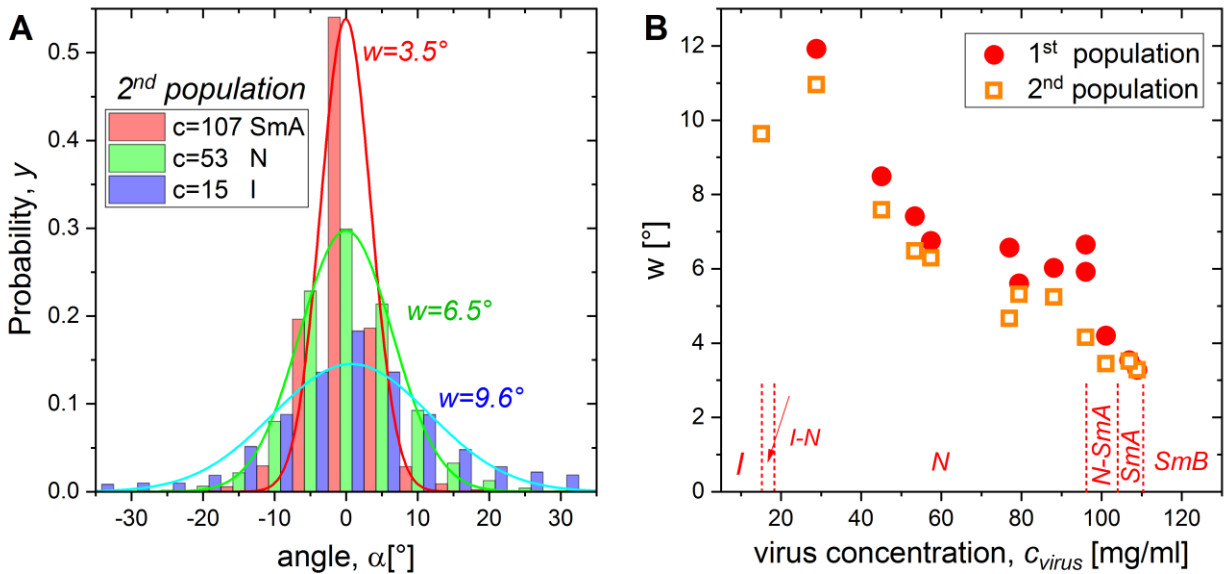


Fig. 8. (A) Examples of the angle displacement distributions at three different concentrations showing the anchored rod deviations (second population of patchy particles) with respect to the direction perpendicular to the cluster whose they are bound to. Numerical fits are performed using Gaussian function $y = A \exp \left[-\frac{1}{2} \left(\frac{\alpha - \alpha_0}{w} \right)^2 \right]$, where α_0 is the center of the distribution, and w is standard deviation of distribution. (B) Standard deviation comparison of patchy rods from first and second particle populations indicating slightly weaker fluctuations of anchored viruses. Angle distributions for patchy rods from the first population in the isotropic phase are expected to be uniform as there is no orientational order, therefore the value of angle standard deviations should be zero. The red dashed lines at the bottom of graph indicate phase diagram of patchy suspension.

Chapter 4

Self-organization of rod-like particles with combination of both entropic and enthalpic patchiness

Contents

4.1 Introduction.....	122
4.2 Material and Methods	123
4.2.1 Enthalpic patchiness: virus tip-labeling with fluorescent dyes	123
4.2.2 Entropic patchiness: choice of depleting agent.....	124
4.3 Results and discussions.....	126
4.3.1 Effect of PEG 20k on tip-labeled suspension	126
4.3.1.1 Phase diagram of fd Y21M+PEG20k	126
4.3.1.2 SAXS experiment on fd Y21M suspension with combined patch.....	128
4.3.1.3 Single rod dynamics within the assemblies	131
4.3.2 Effect of PEG 8k on tip-labeled viral suspension	132
4.4 Conclusions.....	134
4.5 References.....	135

4.1 Introduction

Colloids anisotropic in shape and in surface chemical functionality have attracted recent interest in soft matter science due to their promising role as constituent blocks for self-assembly into novel functional materials [1]. One can distinguish two complementary concepts of interaction directionality or patchiness between particles [5]: the first concept is related to enthalpic patchiness characterized by sticky chemical functions covering some fraction of colloid surface (discussed in Chapter 1); the second one is entropic patchiness characterized by topological surface irregularities such as corners, dimples, edges *etc.* which are able to mechanically induce directed interactions between building boxes under entropy driven depletion attraction.

The examples of enthalpic patchiness have been reported for colloidal spheres [11] and rods [12]. In case of entropic patchiness, there were also several studies by computer simulation on self-assembly of non-spherical particles, which, in particular, have predicted the existence of diamond lattice exhibiting a full photonic gap [2]-[4]. Several experimental studies demonstrated the use of microparticles possessing dimples [6], and edges [7] to assemble them into colloidal molecules, polymers, and crystals under attractive depletion interaction. Other type of anisotropic particles such as rod-like colloidal fd-viruses has been shown to self-organize into ribbon-like structures [8], membranes [9], and platelets [10] under depletion.

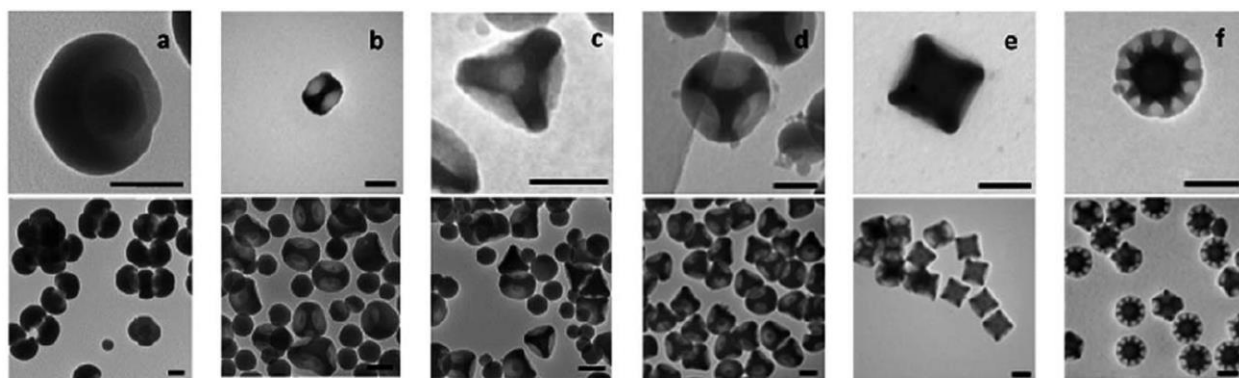


Fig. 4.1. Transmission electron microscopy (TEM) images at different magnification of silica particles with (a) 1, (b) 2, (c) 3, (d) 4, (e) 6, and (f) 12 dimples. Scale bars: 100nm.

Finally, the concept of patchiness has been extended by obtaining silica particles combining both entropic and enthalpic contributions that can be tuned in order to enhance a particular desired particle alignment [13], [14]. It has been shown that preparation of colloids

with a controlled number of dimples from 1 to 12 can be performed adjusting the size of these topological irregularities (Fig. 4.1). Functionalization by sticky propyl groups at the bottom of the dimples and on the conventional particle surface has been reported providing the evidence of getting the particles with two types of patchinesses.

Although, the synthesis of colloids with synergistic effect of combined patchinesses has been reported, the structural and dynamical properties of dispersions containing such objects have not been studied yet. Therefore in this Chapter, using fd-viruses as a model system of colloidal rods, we aim to go beyond depletion studies which have been done on pristine particles [8]-[10], and investigate how localized enthalpic patchiness on rod tips affect the self-organization of viral particle mixture with non-adsorbing polymers. Interaction strength of both entropic and enthalpic contributions can be tuned by varying polymer volume fraction in the suspension and by varying the number of grafted dyes per virus tip respectively. Moreover, the range of depletion interaction can be adjusted by employing polymers with different radius of gyration R_g [17]. Micrometer length scale of colloidal rods allows for studying viral self-diffusion within the structures formed under action of entropic and enthalpic patchinesses at single particle level. In this Chapter, we discuss the competition between two types of directional attractive interaction, and present how it affects the structure morphology formed in virus-polymer mixtures.

4.2 Material and Methods

In this section we introduce, that enthalpic patchiness can be locally achieved at one of the rod tips, while entropic patchy sites can be located on the rod sides.

4.2.1 Enthalpic patchiness: virus tip-labeling with fluorescent dyes

In order to study the effect of combined patchiness, we chose to work with virus mutant fd-Y21M (see section 0.4) as a system of rod-like particles. These viral rods possess two cysteine groups bound by a disulfide bridge at the exposed to the solvent part of P3 protein. Thus, enthalpic patchiness can be induced by performing chemical reaction of fd-Y21M tip-functionalization as reported in Chapter 1. Fluorescent dyes Dylight 594 have been chosen for rod tip-labeling. The average number of grafted dyes per virus tip n_{dyes} has been quantified by optical absorbance measurements. The UV spectra of four independent dilutions of tip-labeled

fd-Y21M were recorded employing Lambda 950 (PerkinElmer) spectrophotometer (Fig. 4.2A), from which, after background subtraction, n_{dyes} has been found to be equal 1 (Fig. 4.2B).

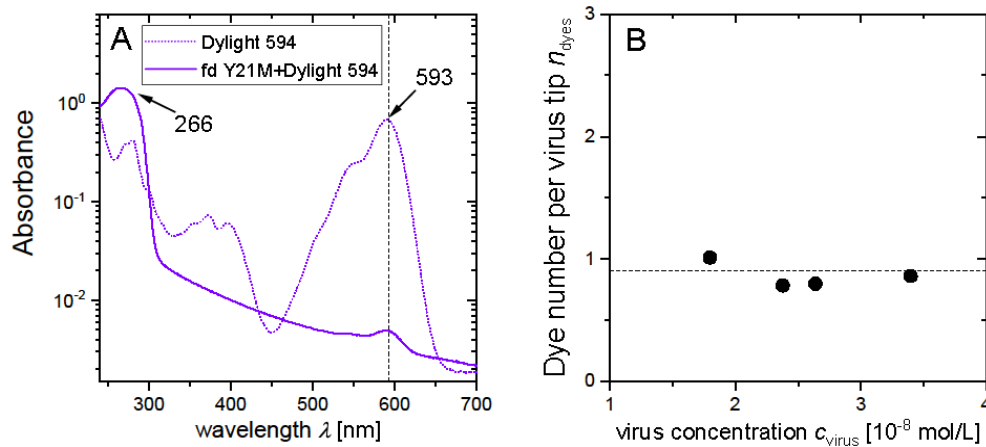


Fig. 4.2. (A) Absorbance of dispersions of pure dyes (Dylight 594) and tip-functionalized fd Y21M viruses measured with the optical path of 10 mm. The concentration of tip-labeled virus suspension is 0.39 mg/mL (2.4×10^{-8} mol/L) and the dye concentration is 9×10^{-3} mg/mL (8.5×10^{-6} mol/L). The numbers represent the wavelength of the maximum absorption. (B) Average number of dyes per virus tip, n_{dyes} , obtained from the absorbance spectra of four dilutions of tip-labeled virus suspension and using the molar extinction coefficient given in [19].

4.2.2 Entropic patchiness: choice of depleting agent

Entropic patchiness for the suspension of anisotropic colloidal particles can be induced by adding non-adsorbing polymers [5]. As the diameter of fd-Y21M mutant is of around $D = 7$ nm, we chose to work with two types of non-adsorbing polymers PEG 20k and PEG 8k to promote different types of morphologies formed under depletion interaction [9], [10]. To facilitate the access of polymers to the viral surface in water dispersion, we use relatively high ionic strength i.e. $I = 260$ mM to reduce the Debye screening length, which is equal to 0.6 nm in this case [15]. The relationship between the radius of gyration $R_g(\text{\AA})$ of PEG and its molar mass M in units of g/mol is $R_g(\text{\AA}) = 0.215M^{0.583}$ [16]. Therefore, the radius of gyration of PEG 20k is $R_g^{20k} = 7$ nm (around twice as high as the radius of fd-Y21M) and of PEG 8k is $R_g^{8k} = 4$ nm (approximately the same as the radius of fd-Y21M). To deduce the maximum depth of depletion potential induced by polymers in viral suspension $U_{dep}^{max}(r = D) = -\Pi V_{overlap}^{Max}$, where Π is osmotic pressure, $V_{overlap}^{Max}$ is the maximized overlap volume between rods (when

parallel rods are in contact with each other, see section 0.3.2), let us assume that our mixture is in dilute polymer regime (below polymer overlap concentration $n_b^{PEG} = 3/(4\pi R_g^3)$, which is 23 mg/ml and 50 mg/ml for PEG 20k and PEG 8k respectively). Thus, osmotic pressure exerted on the colloidal particles is proportional the depletant number density n_b^{PEG} : $\Pi = n_b^{PEG} k_B T$. Using the expression $n_b^{PEG} = c_b^{PEG} \frac{N_A}{M}$ (where c_b^{PEG} is polymer mass concentration in units of mg/ml and N_A is Avogadro's number), and the maximum value of overlap volume for both polymers (for PEG 20k: $V_{overlap}^{Max} = 661 \cdot 10^3 \text{ nm}^3$, and for PEG 8k: $V_{overlap}^{Max} = 236 \cdot 10^3 \text{ nm}^3$, see Appendix, section 3) we can now write down an equation which describes the dependence of the depletion potential depth between two parallel fd-Y21M on polymer volume concentration:

$$U_{dep}^{Max}(r = D) = -c_b^{PEG} \cdot \frac{N_A}{M} \cdot V_{overlap}^{Max} \cdot k_B T \quad (4.1)$$

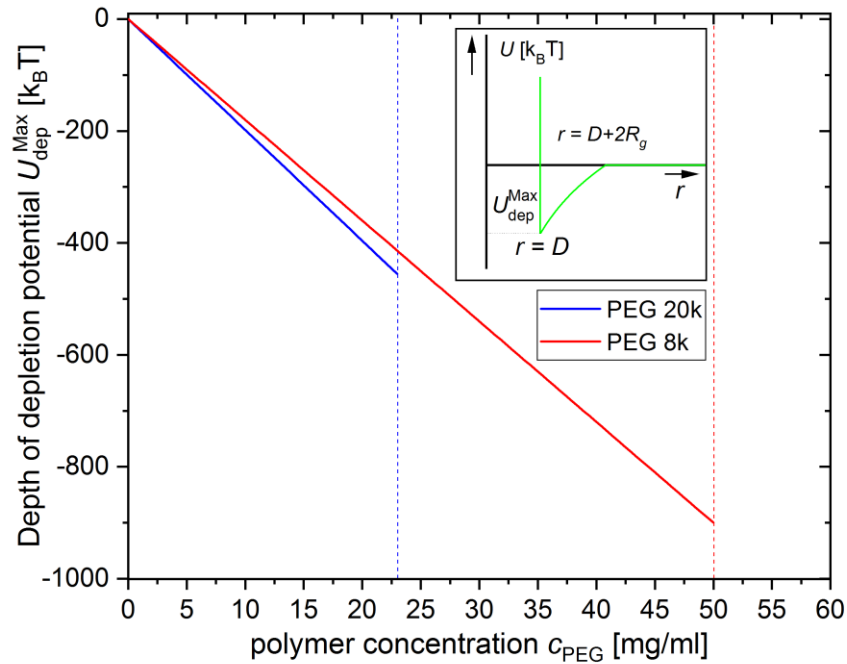


Fig.4.3 Evolution of depth of depletion potential between two parallel fd-Y21M viruses with polymers PEG 20k (blue line) and PEG 8k (red line) volume concentration. Inset: sketch of depletion potential between two parallel hard rods indicating depth of depletion potential U_{dep}^{Max} (r is the center-to-center distance between two rods, D is rod diameter, R_g is polymer radius of gyration or half of the thickness of depletion layer surrounding rod). Dashed blue and red lines correspond to PEG 20k and PEG 8k overlap concentrations.

The evolutions of U_{dep}^{Max} in the units of $k_B T$ with polymer mass concentration are plotted in Fig. 4.3 for two types of polymers. It is worth mentioning that the values of U_{dep}^{Max} given by expression (4.1) are overestimated in our experiments as the rod diameter is compatible with the size of polymers resulting in colloid penetration into open polymer structure [20] (see illustration in Appendix, section 4). This leads to the weaker depth of depletion attraction than the one predicted by expression (4.1).

4.3 Results and discussions

Strictly speaking, the range of enthalpic patchy attraction between functionalized viral tips in our system is not known. Therefore, to probe the competition between entropic and enthalpic patchiness and its effect on viral self-assembly, we employ two types of polymers with different sizes to induce attractive depletion interaction of varying range.

4.3.1 Effect of PEG 20k on tip-labeled suspension

4.3.1.1 Phase diagram of fd Y21M+PEG20k

All data on fd Y21M and PEG 20k mixtures reported below have been obtained by the former postdoc in our group Baeckkyoung Sung.

At zero polymer concentration pristine fd-Y21M rods form stable isotropic, (chiral) nematic, and smectic phase [22], [23] with increasing viral volume fraction in agreement with theoretical and computer simulation predictions [24], [25]. The phase diagram of non-labeled rod-like viruses with effective attraction interaction induced by non-adsorbing polymers has been reported elsewhere [20], [21]. Our experimental phase diagrams of pristine fd-Y21M and tip-labeled mixtures with PEG 20K are reported in Fig. 4.4 being qualitatively similar to the one reported by Dogic [21]. Depletion interaction between rods has been shown to widen the isotropic-nematic phase coexistence region with polymers mainly located into the isotropic phase. In this case, nematic droplets (tactoids) are formed in the isotropic background (Fig. 4.4E). Unwound chiral nematic phase within individual tactoids has been observed because cholesteric order cannot be developed due relatively high strength of planar anchoring of rods at the isotropic-nematic interface.

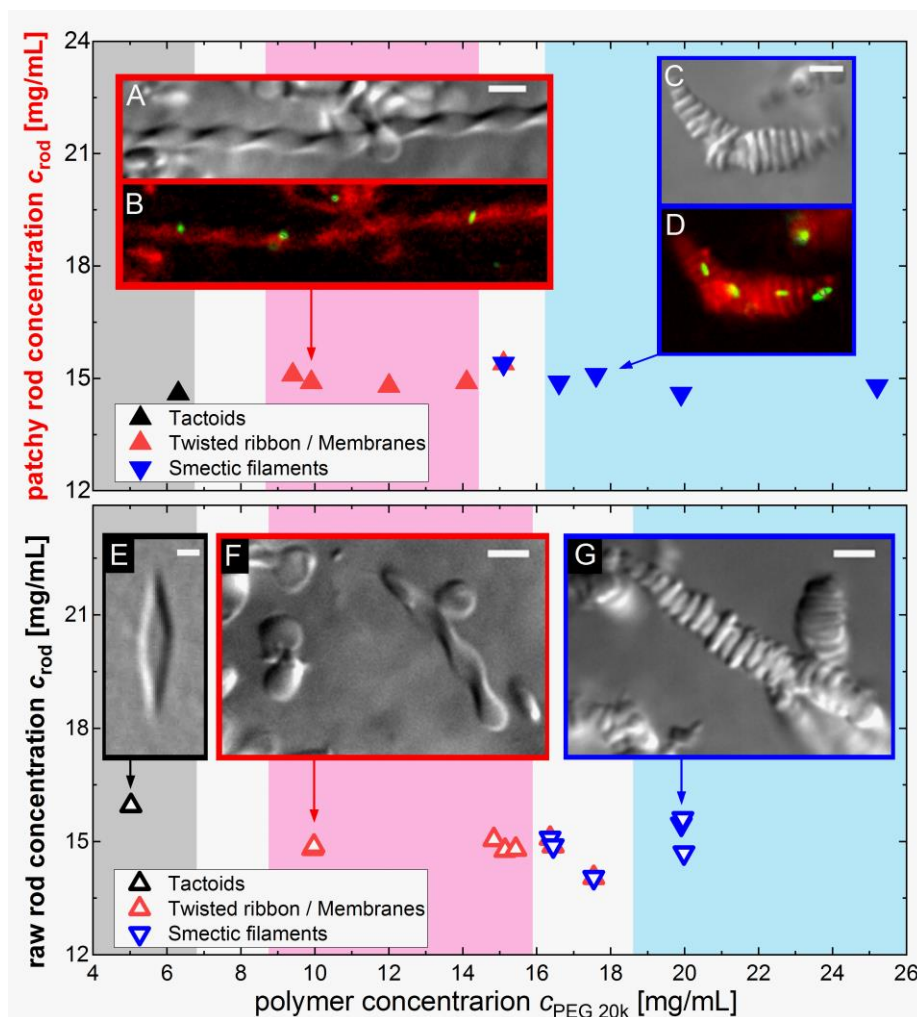


Fig. 4.4. Phase diagram of tip-labeled *fd*-Y21M (top panel) and pristine *fd* Y21M (bottom panel) virus suspension under depletion interaction. **Top panel:** inserted images indicate DIC (A) and fluorescent (B) microphotographs of twisted ribbons with membranes as well as DIC (C) and fluorescent (D) pictures of smectic filaments formed in tip-labeled viral suspensions. **Bottom panel:** DIC images of tactoids (E), twisted ribbons with membranes (F), and smectic filaments (G) in pristine virus dispersions. Green signals represent the positions of tip-labeled viruses which additionally received full body labeling and were added into suspension with ratio of 1:10⁴. Color coding for the different structures is given in the inset, and the white regions indicate the phase gaps between coexisting states. Scale bars: 3 μ m.

At higher polymer concentrations, right after mixing both pristine and tip-labeled fd-Y21M dispersions with PEG 20k, we observed a self-assembly of rods into ribbon-like and membrane-like structures (Fig. 4.4 A, B, and F). These assemblies have the same morphology as the ones recently reported for fd-wt mixture with Dextran polymers [8], [9]. Membranes are composed of a monolayer of aligned rod in the smectic A configuration with twisted edges. Twisted ribbons are identical to membranes except they possess inhomogeneous tilting of the rods (see section 0.3.2, Fig. 0.12F). Increasing further the depletant concentration leads the disappearance of twisted ribbons, and colloidal membranes are found to stack up on top of each other and form filaments with smectic structure (Fig.4.4 C, D, and G).

Structure morphologies in virus-polymer mixture are determined by the depletant concentration. One would presume that the phase diagram region of tip-labeled rods with smectic A type of ordering (with twisted ribbons and membranes) should be extended into lower polymer concentration, as it has been shown for bulk smectic A phase in Chapter 1. In our experiments, the phase behavior of raw and patchy viruses under depletion interaction is the same (Fig. 4.4), meaning that phase transition between nematic-like (tactoids) and smectic A-like structures is not affected by hydrophobic patchy functions on the rod tips. It could be explained by the weak strength of enthalpic patchiness, which, as deduced from computer simulations, is not higher than $1-2 k_B T$ (see Chapter 1), compared to strength of depletion attraction equal to tens of $k_B T$ (Fig. 4.3). We can also speculate that the range of enthalpic patchiness is relatively short (fractions of nanometer) compared to the maximum range of depletion which is of around 7 nm for PEG 20k. Thus, entropic patchiness overcomes the local attraction between viral tips and fully determines phase behavior of tip-functionalized rods mixture with PEG 20k. According to these results, we can also conclude that the range of enthalpic patchiness between rod ends is significantly lower than that of depletion attraction given by a size of polymer.

4.3.1.2 SAXS experiment on fd Y21M suspension with combined patch

In order to probe the internal order of structures assembled in raw and tip-labeled viral systems under depletion and, thus, measure the average inter-rod distances, we performed SAXS experiments. Scattered profiles of tip-labeled viral dispersion at different polymer concentrations are reported in Fig.4.5. From the width of (100) peaks which correspond to average inter-rod distance, we can conclude, that spectra corresponding to polymer concentrations from $c^{PEG} =$

$9.4 \frac{mg}{ml}$ to $14 \frac{mg}{ml}$ represent liquid-like order of twisted ribbons and membranes, while range of polymer concentrations from $c^{PEG} = 15.4 \frac{mg}{ml}$ to $25.2 \frac{mg}{ml}$ correspond to smectic B filaments with positional order. Using expression $d=4\pi/\sqrt{3}q_{100}$ [22], where q_{100} is the position of (100), we calculated the average inter-rod distance d within structures formed under depletion in case of both pristine and tip-functionalized rods (Fig. 4.6A). We have not detected (110) Bragg reflection, which is supposed to be located at around $q_{110} \approx 1.2 \text{ nm}^{-1}$ (as $q_{100} = \sqrt{3}q_{110}$), and it would be the signature of hexagonal long-ranged positional order especially at highest polymer concentrations [10], [22]. Peak at q_{110} is not visible, probably, due to interference with the rod form factor. Another parameter to characterize and compare raw and tip-labeled systems is the average number of closest neighbors in radial direction for a given depletion strength which has been estimated as the ratio of translational correlation length and inter-rod distance (Fig. 4.6B). Correlation length has been calculated via expression $\xi = \frac{2\pi}{FWHM}$, where $FWHM$ is the full width at half maximum of (100) peak [22].

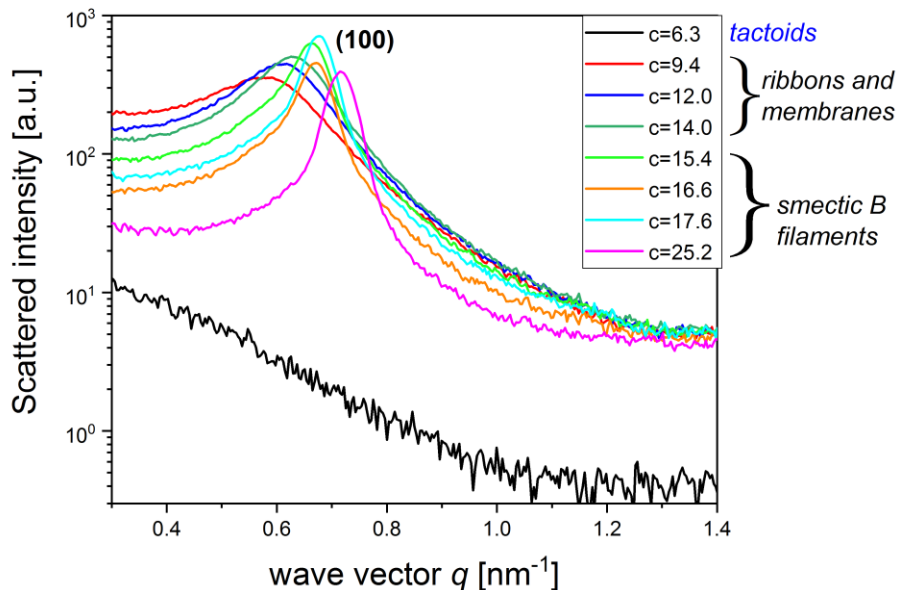


Fig. 4.5. SAXS spectra of tip-labeled *fd* Y21M viruses self-organized into different structures under depletion interaction shown in Fig.4.4. Numbers in the inset correspond to polymer concentration in mg/ml . Spectra which correspond to twisted ribbons and membranes span the range from $c^{PEG} = 9.4 \frac{mg}{ml}$ to $14 \frac{mg}{ml}$ revealing broad (100) Bragg reflection; smectic B filaments are within the range from $c^{PEG} = 15.4 \frac{mg}{ml}$ to $25.2 \frac{mg}{ml}$ showing the narrow (100) Bragg

reflection. As wave vector of structure peak for $c^{PEG} = 6.3 \frac{mg}{ml}$ is too low, it is out of accessible range.

Fig.4.6 demonstrates the same evolution of inter-rod distances and number of closest neighbors with concentration for both raw and tip-labeled viral assemblies formed under depletion. From the discontinuity of neighbors number values, we can conclude that transition from liquid-like order to positional order occurs at polymer concentration $c^{PEG} = 15 \frac{mg}{ml}$ for both types of system. Thus, sticky inclusions at viral tips have no effect on local ordering of tip-functionalized rods and their structural properties are determined by effective depletion attraction.

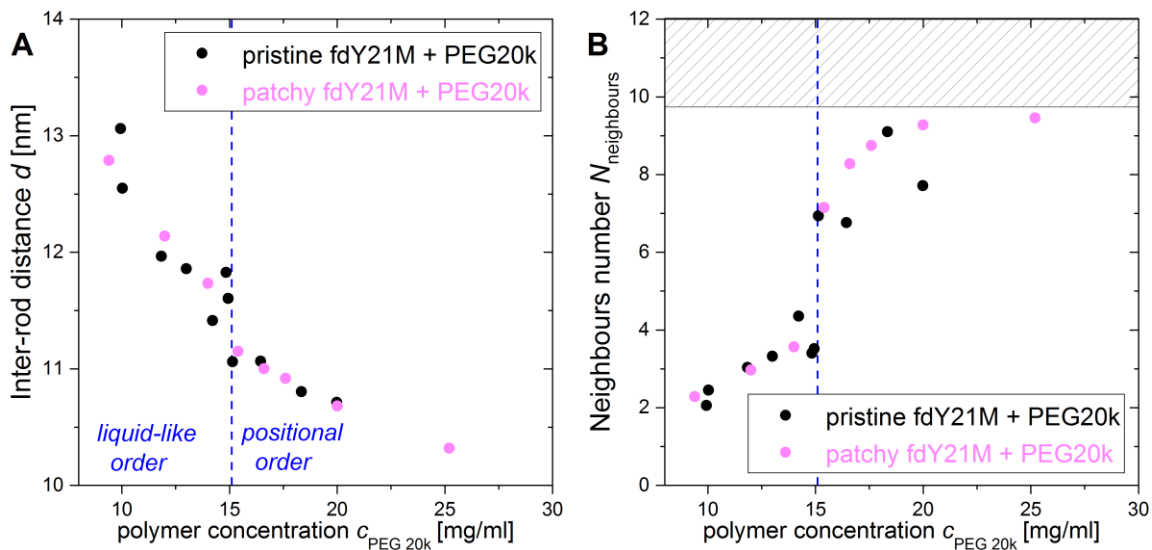


Fig. 4.6. (A) Inter-rod distance $d=4\pi/\sqrt{3}q_{100}$ and (B) average number of closest neighbors for a given polymer concentration in pristine and tip-labeled fd Y21M virus suspensions under depletion interaction. Number of closest neighbors in radial direction is estimated as the ratio ξ/d , where ξ is the translational correlation length measured via expression $2\pi/FWHM$ ($FWHM$ is a full width at half maximum of (100) peak extracted from SAXS spectra in Fig.4.5). Grey dashed area in (B) indicates the instrumental resolution. Blue dashed lines indicate the transition from liquid-like to positional order.

4.3.1.3 Single rod dynamics within the assemblies

DIC microscopy reveals the overall structure of twisted ribbons, such as their pitch (around 4 μm) and width (around 2 μm), as well as lamellar morphology of filaments at higher depletant concentration (Fig.4.4A-C). By adding tracer amount of viruses with combined labeling (green dyes on the body, red dyes on the tip), we can observe local ordering of the assemblies and rod self-diffusion within them thanks to fluorescence microscopy. It shows the liquid-like dynamics of single tip-labeled viruses within the twisted ribbon (Fig.4.7). The same type of motion has been found by Gibaud *et al.* [8] in the ribbons consisting of pristine rods. In case of smectic filaments, we have not detected significant viral motion within them. Tip-labeled viruses have been found to be located perpendicular to the layers. Fluctuations of patchy rod position shown in Fig. 4.8C representing the collective motion of the entire structure whose this particle belongs to. For a given time window of about 10 seconds, we have not detected any hopping-like diffusion of single viruses between filament layers, therefore we confirm positional order within smectic filaments at high depletant concentration evidenced by SAXS.

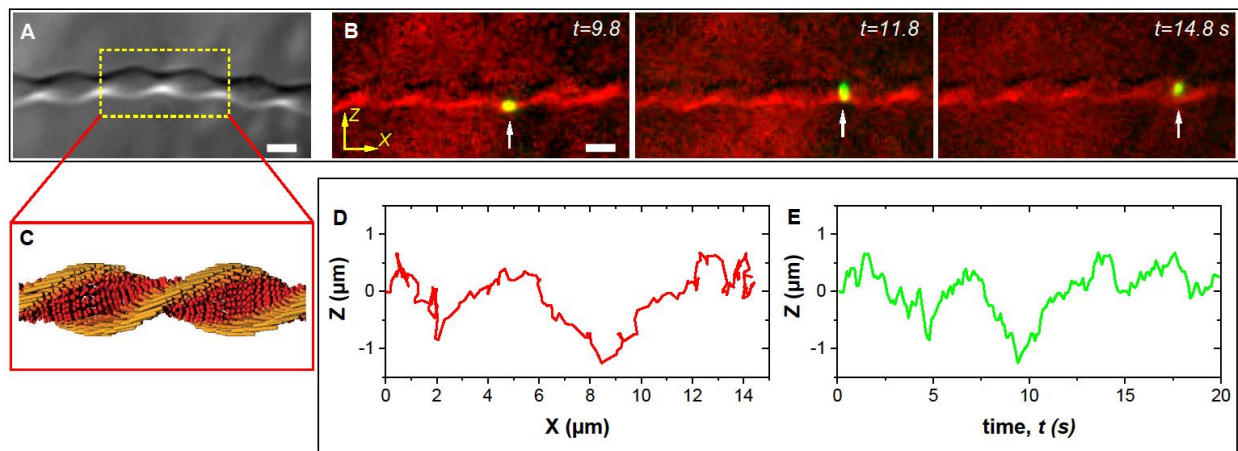


Fig. 4.7. Liquid-like order within twisted ribbons. Isolated twisted ribbon consisting of tip-functionalized fd-Y21M visualized with (A) DIC and (B) at different times with fluorescence optical microscopy. (C) Schematic structure of twisted ribbon [8]. Liquid-like order is deduced from the time –sequence images representing the motion of virus with combined (green dyes on viral body, red dyes on tip) labeling (B). Viral Z-X trajectory (D) and time evolution of Z-component. White arrows indicate particle with combined (red dyes on the tip, green dyes on the

body) labeling diffusing through twisted ribbon in combination with drift motion of entire structure. Scale bars: $2\ \mu\text{m}$.

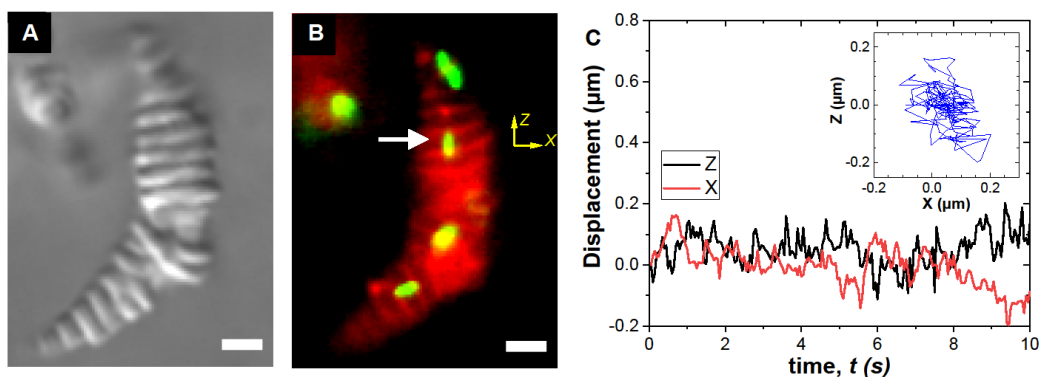


Fig. 4.8. Positional order within smectic filaments consisting of tip-labeled *fd*-Y21M viruses. Smectic B filament visualized with (A) DIC and (B) fluorescence optical microscopy. (C) Particle trajectory representing lack of significant motion within filaments. Inset: viral trajectory in Z-X plane. White arrow indicates the virus whose trajectory is plotted in (C). Nearly perpendicular virus position with respect to filaments layer confirms smectic B nature of the assemblies. Scale bar: $2\ \mu\text{m}$.

4.3.2 Effect of PEG 8k on tip-labeled viral suspension

Data on *fd* Y21M and PEG 8k mixture reported below have been obtained by a PhD student in our group Arantza Zavala Martinez.

As there is no effect of enthalpic patchiness on virus self-assembly under depletion attraction induced by PEG 20k, we have changed the depletant agent and chose to work with smaller polymer PEG 8k decreasing the maximum range of depletion forces from 7 nm to 4 nm to induce structures with positional order. Phase behavior of pristine rods and PEG 8k mixture is depicted in Fig. 4.9 (bottom panel). At viral concentrations below 10 mg/ml, we have observed tactoids (nematic droplets) formed in isotropic background (Fig. 4.9C). At higher rod concentrations (up to 15 mg/ml), the same anisotropic structures are self-assembled, but each assembly possesses a layered isotropic-nematic interface (Fig. 4.9D). The distance between closest layers of such interface along the tactoid's long axis is roughly one virus long. These structures have been described by Dogic [21]. They have nematic interior with the surface frozen

smectic phase. Increasing further PEG 8k concentration, we obtained elongated smectic filaments consisting of small membranes stuck on top of each other (Fig. 4.9E).

For the tip-labeled rods mixture with PEG 8k as a depletant agent, we found the region of twisted ribbons within the range of polymer concentrations 10-14 mg/ml (Fig. 4.9, top panel). At higher PEG 8k concentration, smectic filaments been observed.

The appearance of structures with liquid-like order such as tactoids and twisted ribbons under depletion interaction induced by PEG 8k is not expected. Relatively small size of depletant agents should promote the assembly of structures with positional order in isotropic liquid background [10]. This question remains unsolved and opens new perspectives on the investigation of viral systems with entropic patchiness of relatively short ranges compared to viral radius.

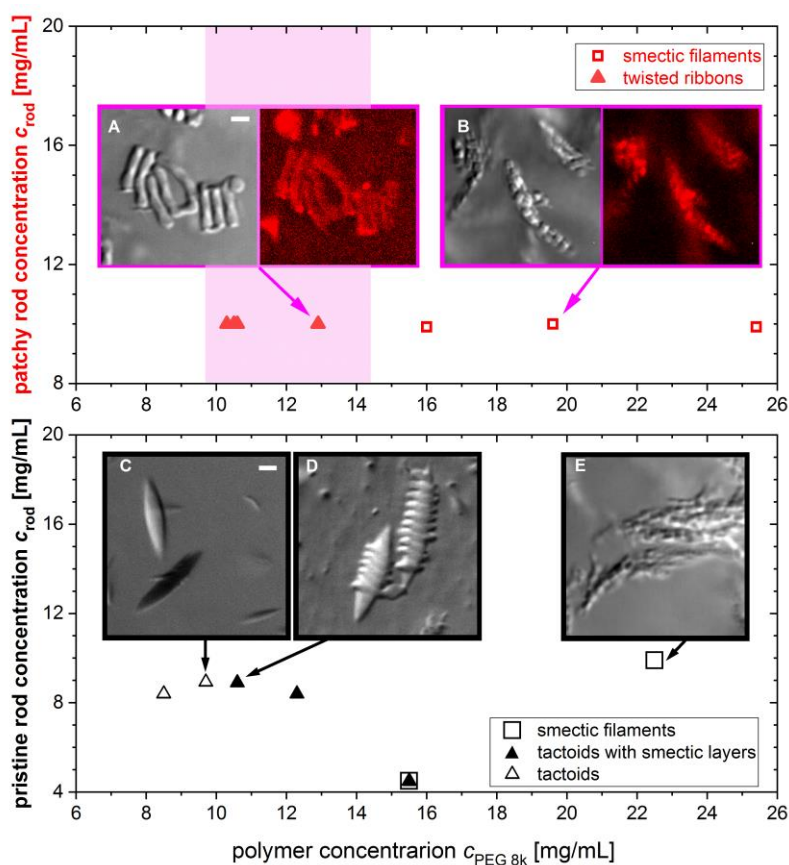


Fig.4.9. Phase diagram of patchy (top panel) and pristine (bottom panel) *fd-Y21M* mixed with PEG 8k polymer. DIC and fluorescence optical microscopy images of (A) twisted ribbons and (B) smectic filaments. Pinkish shadow is drawn to emphasize the twisted ribbon range. DIC

microscopy images of (C) nematic tactoids in isotropic background, (D) tactoids with smectic layers on its surface, and (E) smectic B filaments.

4.4 Conclusions

We combined the effect of entropic and enthalpic patchiness by adding non-adsorbing polymers into dispersion of tip-functionalized fd-Y21M viruses. In order to vary the strength of entropic patchiness i.e. depletion attraction strength [17], we used two types of depletant agents PEG20k and PEG 8k which differ by their size [16]. The radius of gyration of former one is two times higher than the viral radius, while the size the latter depletant is approximately the same as the rod radius.

We found no difference in phase behavior of tip-labeled viruses with in average 1 dye per rod end under depletion interaction induced by PEG 20k compared to phase diagram of pristine rods mixture with these polymers. In our experiments, hydrophobic inclusions on viral tips do not affect the structural properties of rods under depletion promoted by PEG 20k because the strength of enthalpic tip-patchiness is estimated by computer simulations to be not higher than $1-2 k_b T$ which is significantly lower than the strength of entropic patchiness between parallel rods estimated to be tens of $k_b T$. The range of enthalpic interaction in our system in principle is not known, but we can speculate that it is equal to fraction of nanometer which is at least one order of magnitude lower than that of depletion interaction given by a size of polymers. Knowing the fact that number of grafted dye molecules defines the local attraction strength between rod tips (Chapter 1), we can, therefore, expect that increasing the quantity of dyes per viral end one can affect the phase behavior of tip-functionalized particles under depletion interaction. In order to significantly enhance the strength and the range of enthalpic interaction, it is potentially possible to graft other compounds on virus tip to induce attractive interaction such as PNIPAM polymers [26].

Employing polymer PEG 8k as a depletant agent, we decreased the range of entropic patchy interaction by a factor two. Unexpected structures with liquid-like order have been found in both tip-labeled and pristine viral mixtures with relatively small polymers which are supposed to promote positional order within structures. This open question should stimulate new studies of rod self-assembly under depletion attraction with relatively short range of interaction.

4.5 References

1. N. D. Burrows, A. M. Vartanian, N. S. Abadeer, E. M. Grzincic, L. M. Jacob, W. Lin, J. Li, J. M. Dennison, J. G. Hinman, and C. J. Murphy. Anisotropic nanoparticles and anisotropic surface chemistry. *J. Phys. Chem. Lett.*, 2016, 7: 632-641.
2. S.C. Glotzer. Some Assembly Required. *Science*, 2004, 306: 419-420.
3. Z. Zhang, and S. C. Glotzer. Self-Assembly of Patchy Particles. *Nano Lett.*, 2004, 4: 1407-1413.
4. G. van Anders *et al*, Entropically Patchy Particles: Engineering Valence through Shape Entropy. *ACS Nano*, 2014, 8: 931-940.
5. A. V. Petukhov, R. Tuinier, G. J. Vroege. Entropic patchiness: effects of colloid shape and depletion. *Curr. Opin. in Coll. & Int. Sc*, 2017, 30: 54-61.
6. S. Sacanna, W. T. M. Irvine, P. M. Chaikin, and D. J. Pine. Lock and key colloids. *Nature*, 2010, 464: 575-578.
7. L. Rossi, S. Sacanna, W. T. M. Irvine, P. M. Chaikin, D. J. Pine, and A. P. Philipse. Cubic crystals from cubic colloids. *Soft Matter*, 2011, 7: 4139-4142.
8. T. Gibaud *et al*. Reconfigurable self-assembly through chiral control of interfacial tension. *Nature*, 2012, 481: 348-351
9. E. Barry and Z. Dogic. Entropy driven self-assembly of nonamphiphilic colloidal membranes. *PNAS*, 2010, 107: 10348-10353.
10. B. Sung, A. de la Cotte, and E. Grelet. Chirality-controlled crystallization via screw dislocations. *Nat. Commun.*, 2018, 9: 1405.
11. Q. Chen, S. C. Bae, and S. Granick. Directed self-assembly of a colloidal kagome lattice. *Nature*, 2011, 469: 381-384.
12. K. Chaudhary, Q. Chen, J. J. Juárez, S. Granick, and J. A. Lewis. Janus colloidal matchsticks. *JACS*, 2012, 134: 12901-12903.
13. A. Désert *et al*. Synthesis and Site-Specific Functionalization of Tetravalent, Hexavalent, and Dodecavalent Silica Particles. *Angew. Chem.*, 2013, 52: 11068-11072.
14. C. Hubert *et al*. Synthesis of multivalent silica nanoparticles combining both enthalpic and entropic patchiness. *Faraday Discuss.*, 2015, 181: 139-146.
15. H. N. W. Lekkerkerker and R. Tuinier. Colloids and the Depletion Interaction. *Springer*, 2011.

16. K. Devanand, and J. C. Selser. Asymptotic behavior and long-range interactions in aqueous solutions of poly(ethylene oxide). *Macromolecules*, 1991, 24: 5943-5947.
17. S. Asakura, and F. Oosawa. On interaction between two bodies immersed in a solution of macromolecules. *J. Chem. Phys.*, 1954. 22: 1255-1256
18. A. Vrij. Polymers at interfaces and the interactions in colloidal dispersions. *Pure & Appl. Chem.*, 1976, 48: 471-483.
19. S. A. Berkowitz and L. A. Day. Mass, length, composition and structure of the filamentous bacterial fd. *J. Mol. Biol.*, 1976, 102: 531.
20. Z. Dogic *et al.* Isotropic-nematic phase transition in suspensions of filamentous virus and the neutral polymer Dextran. *Phys. Rev. E*, 2004, 69: 051702.
21. Z. Dogic. Surface Freezing and a Two-Step Pathway of the Isotropic-Smectic Phase Transition in Colloidal Rods, *Phys. Rev. Lett.*, 2003, 91: 165701.
22. E. Grelet. Hard-rod behavior in dense mesophases of semiflexible and rigid charged viruses. *Phys. Rev. X*, 2014, 4: 21053.
23. L. Alvarez, M. P. Lettinga, and E. Grelet. Fast Diffusion of Long Guest Rods in a Lamellar Phase of Short Host Particles. *Phys. Rev. Lett.*, 2017, 118: 178002.
24. L. Onsager. The effects of shape on the interaction of colloidal particles. *Ann. N. Y. Acad. Sci.*, 1949, 51: 627–659.
25. D. Frenkel., H. N. W. Lekkerkerker, and A Stroobants. Thermodynamic stability of a smectic phase in system of hard rods. *Nature*, 1988, 332: 822-823.
26. K. Jain *et al.* Tunable LCST behavior of poly(N-isopropylacrylamide/ionic liquid) copolymers. *Polymer Chemistry*, 2015, 38.

Appendix

Calculation of depletion attraction depth for rod-polymer mixture

1. Overlap volume between two cylinders

Let us begin with two overlaid cylinders which have the same height L and radius r (Fig.1). From simple geometrical arguments, their overlap volume $V_{overlap}$ is given by the expression ($S_{overlap}$ is overlap area between cylinder bases):

$$V_{overlap} = L \cdot S_{overlap} \quad (1)$$

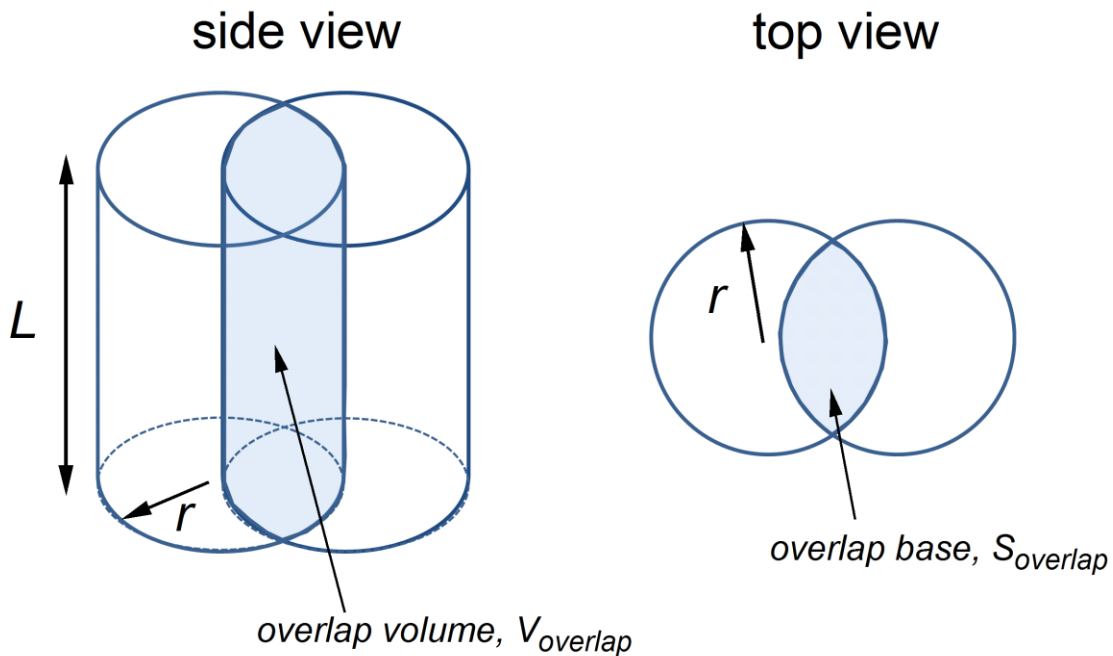


Fig. 1. Scheme representing overlap volume $V_{overlap}$ between two cylinders with heights L and radii r , and overlap area $S_{overlap}$ between their bases.

2. Overlap area between two circles: general case

To quantify the overlap volume between two cylinders, it is, thus, essential to calculate the overlap area between their circular bases. Let us consider the general case, and give the expression for the overlap area $S_{overlap}$ between two circles with different radii r_1 and r_2 (d is the center-to-center distance between two spheres, d_1 and d_2 distances between circle centers and

line which connect two intersection points, A_1 and A_2 are the red and blue areas on the scheme below) (Fig. 2) [1]:

$$S_{overlap} = A_1 + A_2 = R_1^2 \cdot \arccos\left(\frac{d_1}{R_1}\right) - d_1\sqrt{R_1^2 - d_1^2} + R_2^2 \cdot \arccos\left(\frac{d_2}{R_2}\right) - d_2\sqrt{R_2^2 - d_2^2} \quad (2)$$

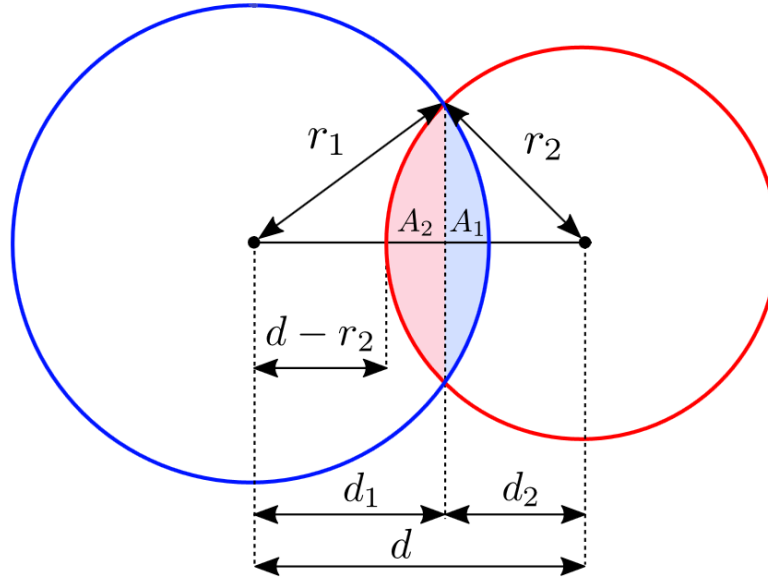


Fig. 2. Overlaid spheres with different radii r_1 and r_2 , where $S_{overlap} = A_1 + A_2$ is the overlap area, d is the center-to-center distance between two circles, and d_1 and d_2 distances between circle centers and line which connect two intersection points [1].

When both radii are equal $r_1 = r_2 = r$, expression (2) can be written as:

$$S_{overlap} = 2A_1 = 2r^2 \arccos\left(\frac{d}{2r}\right) - \frac{1}{2}d\sqrt{4r^2 - d^2} \quad (3)$$

3. Overlap volume for fd-Y21M viruses in mixture with PEG 20k and PEG 8k polymers

Let us move to fd-Y21M virus (length of $L_{virus} = 920$ nm, radius of $R_{virus} = 3.5$ nm) [2] surrounded by the excluded volumes induced (i) by PEG 20k (radius of gyration of $R_g^{20k} = 7$ nm) and (ii) by PEG 8k (radius of gyration of $R_g^{8k} = 4$ nm) [3]. In order to calculate maximum

overlap volume between two excluded layers induced by PEG 20k and PEG 8k polymers around fd-Y21M viruses (Fig. 3), we need to calculate overlap volume between two cylinders with radii (i) $r = R_{virus} + 2R_g^{20k}$ for PEG 20k, and (ii) $r = R_{virus} + 2R_g^{8k}$ for PEG 8k, when *two viruses are in contact* with each other (meaning that $d = 2R_{virus}$).

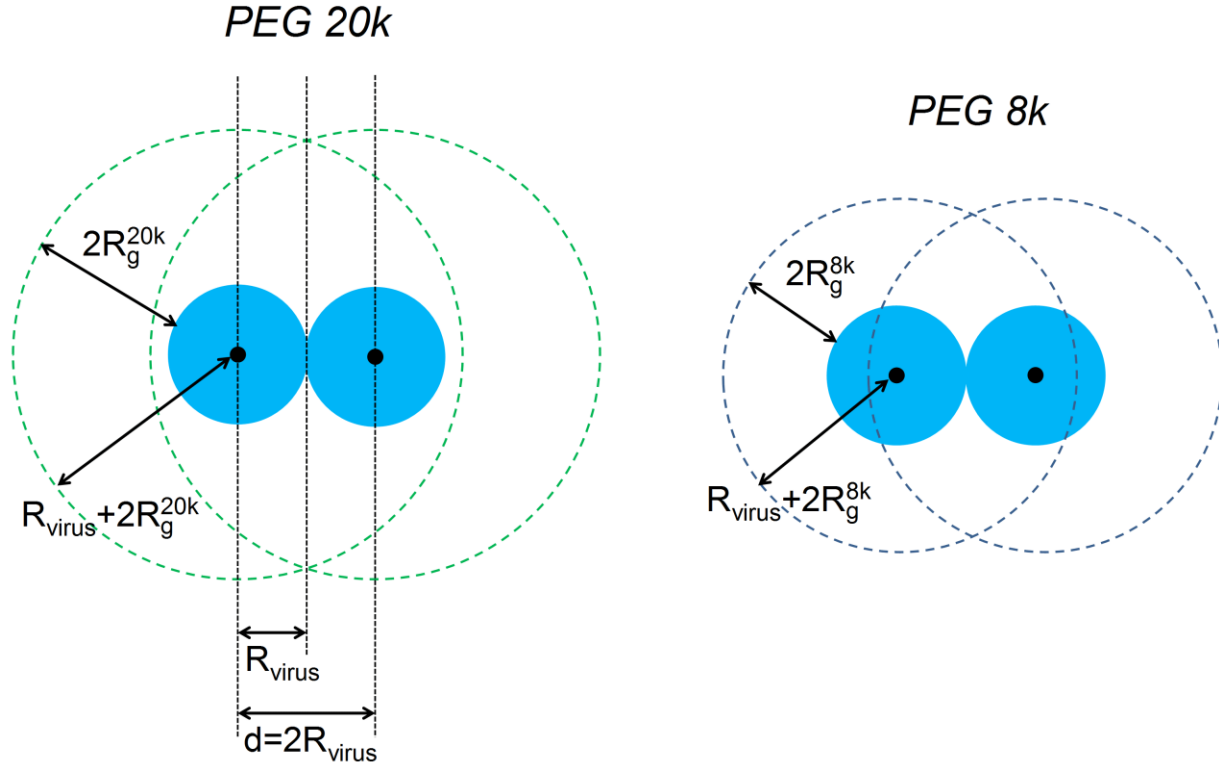


Fig. 3. Scheme representing the top view of maximum overlap volume between excluded layers induced around fd-Y21M viruses by PEG 20k and PEG 8k polymers. Blue circles correspond to viruses, and dashed lines correspond to excluded layers. R_{virus} is viral radius, R_g^{20k} and R_g^{8k} are the radii of PEG 20k and PEG 8k respectively, d is the center-to-center distance between two viruses.

Let us firstly calculate the maximum overlap areas between two cylinder bases which correspond to (i) fd-Y21M+PEG 20k and to (ii) fd-Y21M+PEG 8k. According to Fig. 3 expressions (3) for our case can be rewritten as (R_g is the polymer radius of gyrations):

$$S_{overlap} = 2(R_{virus} + 2R_g)^2 \arccos\left(\frac{R_{virus}}{R_{virus}+2R_g}\right) - R_{virus}\sqrt{4(R_{virus} + 2R_g)^2 - 4R_{virus}^2} \quad (4)$$

Hence, the overlap bases are:

- fd-Y21M+PEG 20k: $S_{overlap} \approx 719 \text{ nm}^2$
- fd-Y21M+PEG 8k: $S_{overlap} \approx 257 \text{ nm}^2$

Therefore, the maximum overlap volumes between two excluded layers for fd-Y21M virus mixture with polymers are:

- fd-Y21M+PEG 20k: $V_{overlap} = L_{virus} \cdot S_{overlap} \approx 661 \cdot 10^3 \text{ nm}^3 = 0.661 \cdot 10^{-21} \text{ m}^3$
- fd-Y21M+PEG 8k: $V_{overlap} \approx 236 \cdot 10^3 \text{ nm}^3 = 0.236 \cdot 10^{-21} \text{ m}^3$

4. Depth of depletion attraction

Finally, we can calculate the depth of depletion interaction potential between two fd-Y21M viruses by using expression [4]:

$$U_{max} = -\Pi \cdot V_{overlap} \quad (5)$$

where Π is the osmotic pressure exerted by the polymers on viruses, and in the dilute polymer regime it is given by expression [4]:

$$\Pi = n_b^{PEG} k_b T \quad (6)$$

Hence (n_b^{PEG} is the polymer concentration),

$$U_{max} = -n_b^{PEG} \cdot V_{overlap} \cdot k_b T \quad (7)$$

Let us calculate U_{max} at polymer overlap concentration which is given by expression [5]:

$$n_b^{PEG} = \frac{3}{4\pi R_g^3} \quad (8)$$

The values for PEG 20k and PEG 8k overlap concentrations are:

- PEG 20k overlap concentration: $n_b^{20k} = 7 \cdot 10^{23} \text{ m}^{-3} = 23 \frac{\text{mg}}{\text{ml}}$
- PEG 8k overlap concentration: $n_b^{8k} = 38 \cdot 10^{23} \text{ m}^{-3} = 50 \frac{\text{mg}}{\text{ml}}$

Using expression (7), we can now calculate the depth of depletion attraction induced by polymers between fd-Y21M viruses:

- Depth of attraction in case of PEG 20k:

$$U_{max}^{20k} = -7 \cdot 10^{23} \text{ m}^{-3} \cdot 0.661 \cdot 10^{-21} \text{ m}^3 \cdot k_b T \approx 462 k_b T$$

- Depth in case of PEG 8k:

$$U_{max}^{8k} = -38 \cdot 10^{23} \text{ m}^{-3} \cdot 0.236 \cdot 10^{-21} \text{ m}^3 \cdot k_b T \approx 897 k_b T$$

It is worth stressing that these values for U_{max} are overestimated due to two points. The first reason is that expression (6) for the osmotic pressure is valid only at dilute polymer regime meaning that polymer concentration must be lower the overlap concentration. The second point is that expression (7) is valid as long as diameter of rod is much larger than the diameter of polymer. In our experiments the size of polymer is the same for PEG 8k and two times higher for in case of PEG 20k than rod diameter. It leads to the virus penetration into the open polymer structure without overlapping any of the polymer segments resulting in the weaker depth of the attractive depletion potential predicted by expression (7) [5].

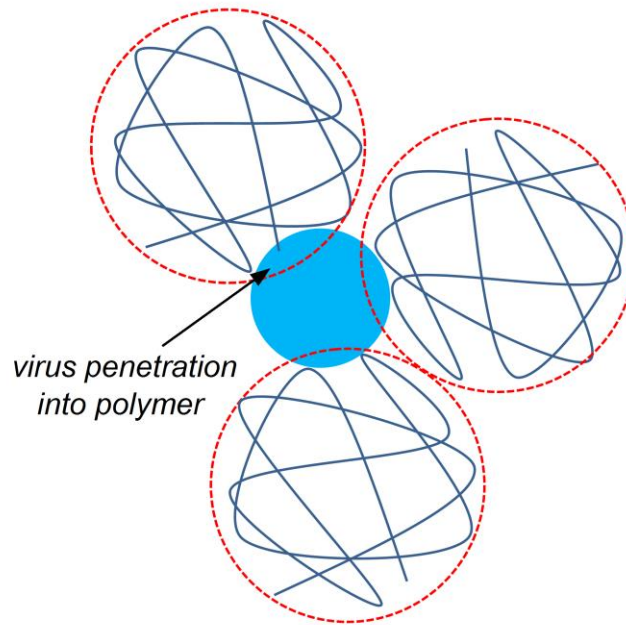


Fig. 4. Illustration of rod penetration into open polymer structure when rod radius is lower (or the same) as the radius of polymer.

References

1. <http://mathworld.wolfram.com/Circle-CircleIntersection.html>

2. E. Pouget, E. Grelet, and M. P. Lettinga. Dynamics in the smectic phase of stiff viral rods. *Phys. Rev. E*, 2011, 84: 41704.
3. K. Devanand, and J. C. Selser. Asymptotic behavior and long-range interactions in aqueous solutions of poly(ethylene oxide). *Macromolecules*, 1991, 24: 5943-5947.
4. H. N. W. Lekkerkerker and R. Tuinier. Colloids and the Depletion Interaction. *Springer*, 2011.
5. Z. Dogic. Isotropic-nematic phase transition in suspensions of filamentous virus and the neutral polymer Dextran. *Phys. Rev. E*, 2004, 69: 051702.

Conclusions and Perspectives

In this thesis, we aimed to investigate the structural and dynamical properties of colloidal rod-like fd-viruses with localized directional attraction interaction. This heterogeneous interaction between particles or so-called "patchiness" has been introduced by functionalizing the proximal viral tips by grafting hydrophobic fluorescent dye molecules onto them. Phase behavior and self-diffusion of patchy rods have been then studied revealing strikingly different features compared to their pristine i.e. purely repulsive counterparts.

We began with studying the structural properties of fd-viruses with local directional attraction in Chapter 1. It has been shown that the strength of patchy interaction between rod tips depends on the number of bound dye molecules, which has been tuned by employing different viral mutants and by varying the dye molar excess during the labeling reaction. In order to model our experimental system of patchy colloids and get deeper insight into the effect of localized interaction on their self-assembly, computer simulations have been conducted by the group from Eindhoven University of Technology in which rods were represented by the chain of partially overlapped hard spheres with an attractive bead at the end. We have shown, in agreement with numerical simulations, that increasing the attraction strength between rod tips extends the smectic phase range at the cost of the nematic phase leaving other phase transitions i.e. isotropic-nematic and smectic-columnar nearly unchanged. It has been suggested that only the lamellar ordering responds to the tip-labeling because in this organization all sticky viral tips are brought together being not highly correlated in other states of virus dispersion.

In this work, fluorescent dyes at the tips of fd-viruses have been used also for the observation of liquid crystalline structure in lamellar organization with improved resolution and contrast. In Chapter 2, we visualized the linear topological defect in smectic phase, such as edge and screw dislocations, at the lattice periodicity level. Edge dislocation profile has been extracted as well as quantitative analysis of displacement field has been performed and compared to the theoretical predictions. The intrinsic length scale (elastic length) over which an imposed distortion relaxes in a lamellar system has been experimentally determined for our viral dispersions giving the value which is two orders of magnitude lower than the smectic layer periodicity. In case of screw dislocations, we visualized the structure of the defect core enabling

its handedness determination. The distribution of core width has been also established showing its mean value to be equal to the lamellar periodicity. Self-diffusion experiments performed at the single rod level revealed the nematic-like organization within the screw dislocations.

Having clear insight about phase behavior of patchy viruses, our focus has shifted to the investigation of their dynamical properties. Dynamics of both patchy and pristine rods have been studied and compared by tracking individual particle displacements by fluorescence optical microscopy. In order to characterize the differences between the two types of rods, their self-diffusion coefficients have been experimentally measured. We evidenced that in all liquid crystalline phases of virus dispersions patchy rod diffusion is hindered compared to the diffusion of pristine ones. Particularly in smectic phase, tip-labeled rods have been found to mainly diffuse within the smectic layers perpendicular to the rod main axis, contrary to the non-labeled particles whose self-diffusion between layers is far more pronounced. This behavior has been explained by the higher smectic ordering potential experimentally measured in the dispersions of patchy rods compared to the potential obtained for raw particles. Angle fluctuations of individual rods with respect to the director at different concentrations have provided quantitative measurements of the orientational order parameter, which has been found to show similar behavior for both viral systems. This is consistent with the fact that isotropic-nematic phase transition is not affected by rod tip-functionalization. We also discussed the anomalous diffusion in the lamellar organization of viral dispersions estimating the typical “cage” size, which has been evidenced to have the same order of magnitude as the smectic layer periodicity.

In the last Chapter of the thesis, we combined the effect of entropic and enthalpic patchinesses. Non-adsorbing polymers have been added into dispersion of tip-labeled fd-viruses inducing effective depletion attraction between rod sides. Experimental phase diagrams for two viral systems under depletion interaction have been established by optical microscopy and SAXS experiments revealing no effect of sticky rod ends on self-assembly of tip-labeled viruses. We interpreted it by the both short range and weak strength of attraction induced by hydrophobic dyes which are not sufficient to affect the viral interaction originating from depletion effect. As a perspective of this work, in order to enhance both range and strength of attraction between rod ends, we suggested to employ other compounds to induce attraction interaction such as thermo-responsive PNIPAM (poly(N-isopropylacrylamide)) polymer [1]. By increasing the temperature

to more that the lower critical solution temperature (LCST) this polymer becomes hydrophobic which could lead to the *reversible patchiness* at the viral tip (Fig. 1A).

An idea of introducing patchy interaction between rod-like viral particles opens up a several perspectives for further investigation of complex fluids with directional attractive interactions. The directional attractive interaction induced by PNIPAM patch could be reversibly controlled by heating up or cooling down the colloidal dispersion with respect to LCST. For example, if we heated up the colloidal dispersion in the nematic phase consisting of PNIPAM-functionalized viruses, the thermo-induced smectic phase at the same virus concentration would be generated due to attraction between hydrophobic polymers at the rod ends (Fig.1B). Such complex fluid could be an example of liquid crystal where phase transitions can be tuned by both particle volume fraction and temperature at the same time.

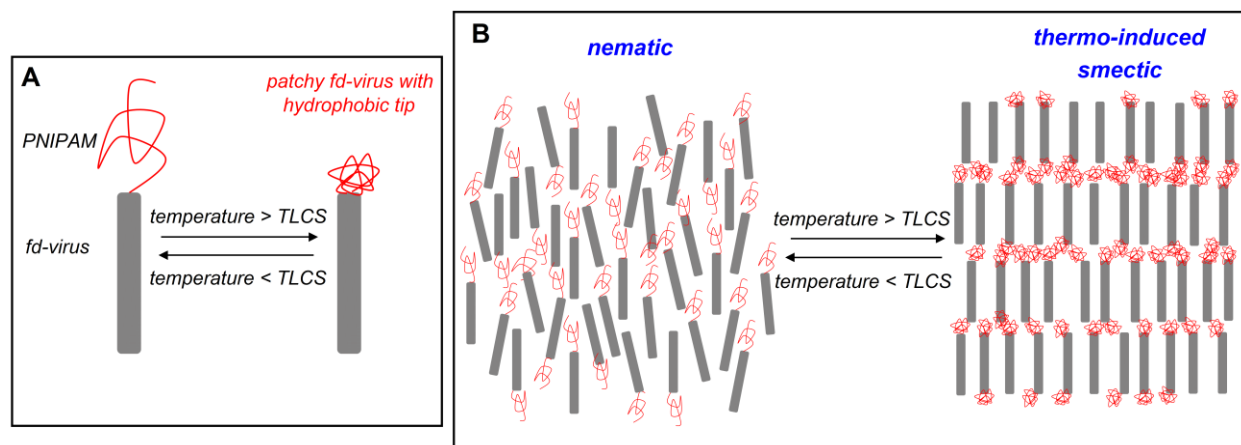


Fig. 1. (A) Scheme of thermo-responsive fd-virus with tip-patchiness induced by poly(*N*-isopropylacrylamide) (PNIPAM) polymer on the one of the rod ends. The directional attractive interaction could be achieved by heating up the colloidal dispersion above lower critical solution temperature (LCST) [1]. (B) Reversible nematic-smectic phase transition could then occur upon increasing the temperature of PNIPAM-functionalized viral dispersion.

In future, one can also use the mixture of tip-labeled rods with non-adsorbing polymers to study the fluctuation spectra of colloidal membranes assembled under depletion interaction [2]. Improved contrast and resolution of optical images obtained with fluorescence microscopy could reveal detailed information on thermal undulations of top and bottom membrane surfaces (Fig.2), which are otherwise not accessible with DIC microscopy.

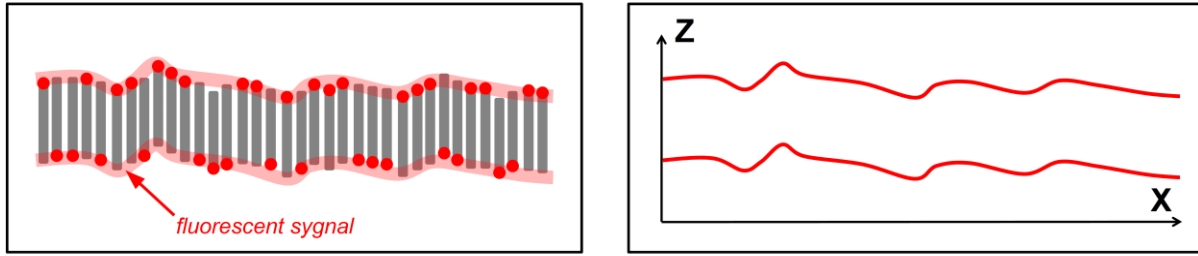


Fig. 2. (Left) Schematic side view of colloidal membrane constituting of tip-labeled rods. Fluorescent signal comes from both top and bottom membrane surfaces. (Right) Spectra coming from both membrane surfaces could be recorded with fluorescence optical microscopy.

Another short-term perspective could be, for example, to investigate the structural properties of patchy viral dispersions varying the rod flexibility. Higher rod stiffness has been shown to stabilize the smectic phase [4]. Thus, one could be interested what would be the phase behavior of tip-labeled viruses which possess higher persistent length such as fd-Y21M. In terms of dynamical study, we could compare the self-diffusion of pristine and tip-labeled particles in the liquid crystalline matrix of patchy viruses. It would be interesting to investigate the effect of attraction mean-field induced by sticky viral tips on the mobility of raw i.e. purely repulsive rods.

As a long-term perspective, one could use fd dispersion in smectic phase as a transmission diffraction grating for various photosensitive devices [3] thanks to its typical lamellar periodicity of around $1 \mu\text{m}$. Illumination of viral suspension in smectic phase by white light results in the light diffraction. Thus according to the Bragg law $\lambda = d \cdot \sin\theta$ (where λ is wavelength, d is a periodicity of diffracting grating i.e. smectic layer spacing, and θ is the deviation of a given wave from the 0^{th} diffraction order (Fig.3)), white light spreads out with different colors depending on their wavelengths (Fig. 3A). Our experiments showed that typical variation of smectic layer spacing values for patchy suspensions spans the range from $d=1 \mu\text{m}$ to $d=1.04 \mu\text{m}$, which is twice higher than the values range for raw suspensions. If we placed a screen in front of illuminated smectic dispersion with grating periodicity of $1 \mu\text{m}$, blue light would deviate on angle of $\theta = 23.6^\circ$ whereas red light would deviate on angle of $\theta = 44.4^\circ$. In this case, according to the expression $h = D \cdot \tan\left(\sin^{-1}\frac{\lambda}{d}\right)$, at screen-to-grating separation

equal to, for example, $D=10$ cm, the distance between 0^{th} diffraction order and blue or red spot will be $h=4.4$ cm or $h=9.8$ cm respectively (Fig. 3B). In case of diffraction grating periodicity of $d=1.04$ μm the positions of blue and red spots will be shifted down to the heights of $h=4.2$ cm and $h=9.1$ cm respectively. If we were able to change the virus concentration by varying the volume of smectic dispersions, we would be able to control the periodicity of diffraction grating i.e. smectic layer spacing, and therefore tune the positions of colors on the screen. This technique could be potentially applied in various photonic devices [3].

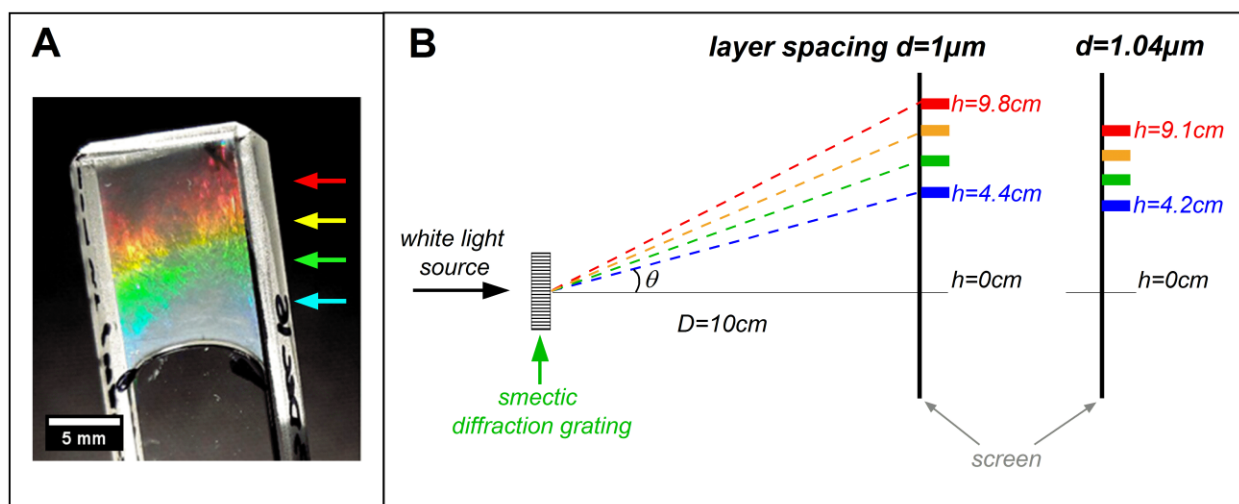


Fig. 3. (A) Glass cuvette which contains fd smectic dispersion illuminated from behind by white light. Variation of colors represents the light diffraction. Blue, green, yellow, and red arrows are drawn for eye guide to indicate the colors which appear thanks to wave deviation according to the Bragg law. Scale bar is 5 mm. (B) Scheme of the setup with smectic viral suspension as a diffraction grating with varying periodicity. Positions of colors are shown at the two different periodicity values of $d=1\mu\text{m}$ and $d=1.04\mu\text{m}$, which are the lowest and the highest values respectively found in our experiments.

As another long-term perspective, we could also use the genetic modifications on p9 and p7 proteins to display disulfide bridge (S-S bond) on the distal end of fd virus, in order to graft patchy functions efficiently. With, for example, fluorescence dye molecules at *both ends* of the rod (Fig. 4), we could expect to strengthen the effect of smectic phase extension at the cost of the nematic or even the isotropic phase.



Fig. 4. Scheme of bifunctionalized fd virus by fluorescent dye molecules.

Overall, localized directional interaction between rod-like building blocks can promote the appearance of highly desirable for material science layered structures [5] at low particle volume fraction.

References

1. K. Jain *et al.* Tunable LCST behavior of poly(N-isopropylacrylamide/ionic liquid) copolymers. *Polymer Chemistry*, 2015, 38.
2. E. Barry and Z. Dogic. Entropy driven self-assembly of nonamphiphilic colloidal membranes. *PNAS*, 2010, 107: 10348–10353.
3. Nicolas Bonod, Jérôme Neauport. Diffraction gratings: from principles to applications in high-intensity lasers. *Adv. in Opt. and Phot., Opt. Soc. of Am.*, 2016, 8: 156-199.
4. E. Grelet. Hard-rod behavior in dense mesophases of semiflexible and rigid charged viruses. *Phys. Rev. X*, 2014, 4: 21053.
5. S. Z. Butler *et al.* Progress, Challenges, and Opportunities in Two-Dimensional Materials Beyond Graphene. *ACS Nano*, 2013, 7: 2898.